Implémentation numérique de la fermeture de turbulence d'ondes dans un canal rotatif

Aleksandr Eremin

ÉCOLE CENTRALE LYON

Numéro d'ordre NNT: 2019LYSEC31 Année: 2019

THÈSE de DOCTORAT DE L'UNIVERSITÉ DE LYON
opérée au sein de **L'ÉCOLE CENTRALE DE LYON**

ÉCOLE DOCTORALE MEGA
Mécanique, Energétique, Génie civil et Acoustique

Spécialité: Mécanique des fluides

Soutenue le 05/11/2019 par

Aleksandr EREMIN

Numerical implementation of the wave-turbulence closure in a rotating channel

---

Devant le jury composé de:

Anne CADIOU	Ingénieure de recherche, CNRS	Examinatrice, co-encadrante
Sergio CHIBBARO	Maître de conférences, Sorbonne Université	Rapporteur
Benjamin FAVIER	Chargé de recherche, CNRS	Examinateur
Sébastien GALTIER	Professeur des Universités, École Polytechnique	Rapporteur
Fabien GODEFERD	Directeur de Recherche, CNRS	Examinateur, co-encadrant
Nicolas MORDANT	Professeur des Universités, Université Grenoble Alpes	Président
Aurore NASO	Chargée de recherche, CNRS	Examinatrice
Julian SCOTT	Professeur des Universités, École Centrale de Lyon	Directeur de thèse

Abstract

A problem of turbulence in a rapidly rotating channel is investigated. The rapid rotation means that nonlinearity is dominated by rotation suggesting application of wave-turbulence theory.

The first part of the work is devoted to study of the wave-turbulence closure (WTC) model. We express the velocity field as a combination of inertial waveguide modes. In its turn, confinement implies discretization of the wall-normal component of the wave vector. The nonlinear transfer is dominated by resonant interactions of wave-vector triads. Viscosity is present via modal damping, which is the sum of two components: volumetric and wall damping. The volumetric-damping rate grows as the square of the wavenumber inhibiting the energy cascade below a certain scale.

The numerical implementation of the model uses a time-marching scheme ensuring the realizability property of the model and explicit consideration of the spectral discontinuities predicted by the wave-turbulence theory. According to the results of numerical investigation of the WTC model the time evolution of the turbulence occurs in two phases. During the first phase wall damping dominates, but following an energy cascade to the small scales, volumetric damping takes over during the second phase. Provided the volumetric-damping coefficient is sufficiently small, the transition between the phases takes place abruptly at a time which is insensitive to both wall- and volumetric- damping coefficients, but varies significantly with the third parameter of the problem, which is the initial spectral width. Evolution of the spectra reveals the development of an inertial range whose exponent is found to be almost independent of the problem parameters. The transfer of energy parallel to the channel walls is found to be more efficient than in the cross-channel direction.

To perform direct numerical simulations (DNS) an appropriate method for initialization of the velocity field possessing the statistical properties prescribed by the model is developed. Comparison of the DNS and WTC results requires construction of the spectral matrix at later times. This involved the development of spectral analysis methods and their incorporation into the existing DNS code. Despite running the DNS on a super-computer and using many processors in parallel, only three runs were feasible. Those runs used the same physical parameters and different DNS spatial periods to check for convergence with respect to that numerical parameter. In an ideal world, many realizations would be performed and the ensemble average taken to calculate the spectral matrix. Given one run, this is not possible, so we instead developed a method based on statistical isotropy in the directions parallel to the walls in which averages are taken over annular regions in spectral space. Unfortunately, the results indicate that nonlinearity is not small enough for the Rossby number used in the DNS. That is, further reduction of the Rossby number would be needed to reach the regime of applicability of the wave-turbulence theory. This is not achievable with the computer power available.

Résumé

L'étude porte sur un problème de turbulence dans un canal mis en rotation rapide. Dans ce cas, la non linéarité est dominée par la rotation, ce qui suggère d'utiliser la théorie de la turbulence d'ondes.

La première partie de ce travail porte sur l'étude du modèle de fermeture pour la turbulence d'ondes (WTC pour « wave-turbulence closure »). Nous exprimons le champ de vitesse comme combinaison de modes de guide d'onde inertiels. Le confinement en canal implique aussi une discrétisation de la composante du vecteur d'onde normale à la paroi. Le transfert non linéaire est dominé par les interactions résonantes entre triades de vecteurs d'ondes. La viscosité, qui se manifeste par l'amortissement des modes, est la somme de deux contributions : l'une volumique, l'autre due à la paroi. Le taux d'amortissement en volume croît comme le carré du nombre d'onde, et inhibe la cascade d'énergie en-deçà d'une certaine échelle de longueur.

L'implémentation numérique du modèle utilise un schéma d'avancement en temps qui assure la propriété de réalisabilité du modèle ainsi que la prise en compte des discontinuités spectrales prédites par la théorie de turbulence d'ondes. Les résultats de notre étude numérique du modèle WTC montrent que l'évolution en temps de la turbulence se produit en deux phases. Pendant la première phase, l'amortissement dû à la paroi est dominant, mais à la suite de la cascade d'énergie vers les petites échelles, l'amortissement volumique prend le dessus pendant la seconde phase. Lorsque le coefficient d'amortissement volumique est suffisamment petit, la transition entre les deux phases se produit brusquement à un instant qui est indépendant à la fois des coefficients d'amortissement volumique et de paroi, mais qui varie significativement avec le troisième paramètre du problème qu'est la largeur spectrale initiale. L'évolution du spectre révèle le développement d'une zone inertielle dont la pente se trouve presque indépendante des paramètres du problème. Le transfert d'énergie parallèlement aux parois du canal apparaît être plus efficace que dans la direction normale.

En vue de réaliser des simulations numériques directes (DNS pour « Direct Numerical Simulations »), il a fallu développer une méthode appropriée à l'initialisation d'un champ de vitesse possédant les propriétés statistiques prescrites par le modèle. La comparaison des résultats de DNS et de WTC nécessite la construction de la matrice spectrale aux temps ultérieurs. Ceci a nécessité le développement de méthodes d'analyse spectrale et leur incorporation au sein du code de DNS existant. Malgré l'utilisation d'un super-calculateur et du calcul massivement parallèle, seuls trois calculs de DNS ont été possibles. Ces calculs utilisent les mêmes paramètres physiques mais différentes périodes spatiales pour la DNS, afin de vérifier la convergence en fonction des paramètres numériques. Idéalement, de nombreuses réalisations devraient être lancées et une moyenne d'ensemble prise pour calculer la matrice spectrale. Ceci n'étant pas possible avec un seul calcul, nous avons plutôt développé une méthode s'appuyant sur l'isotropie statistique dans les directions parallèles aux parois, dans laquelle les moyennes sont faites sur des domaines annulaires de l'espace spectral. Malheureusement, nos résultats indiquent que la non linéarité n'est pas suffisamment faible au nombre de Rossby utilisé dans les DNS. Par conséquent, un abaissement supplémentaire du nombre de Rossby serait nécessaire pour atteindre le régime d'applicabilité de la théorie de turbulence d'ondes. Ceci n'est cependant pas envisageable avec la puissance de calcul à disposition.

Acknowledgements

I cannot imagine how this work could be accomplished without support of several people and in this small but important section I'm going to express my sincere gratitude to these people.

In a first turn, I owe my deepest gratitude to my supervisors, Julian Scott, Fabien Godeferd and Anne Cadiou, who taught me how to conduct a high-quality research applying the art of rigorous mathematical derivations and justifying further numerical investigations of a problem. They also did not leave aside the importance of being present in the scientific community and ethical aspects of research. I'm very thankful for all the time we spent together on our weekly meetings and for their ability to keep patience whatever happened.

I want to thank all the member of my jury, particularly the reviewers, Sébastien Galtier and Sergio Chibbaro, for accepting my invitation and constructive comments on the manuscript and during the defence. I'm equally thankful to the members of monitoring committee, Grégory Vial and Fabrice Thouverez for proper discharge of their duties.

Special thanks should be offered to Christophe Pera who provided me special conditions in the computing centre P2CHPD (Pôle de Calcul Hautes Performances Dédiés) and to Laurent Pouilloux for maintaining the cluster of the PMCS2I (Pôle de Modélisation et Calcul en Science de l'Ingénieur et de l'Information) and for resolving all the technical issues arising during my work.

I also appreciate very much the help of Christophe Corre and Emmanuel Drouard in my humble experience of teaching.

There are two more people without whom I would have no chance to start my PhD — Michèle Debrenne, coordinator of the Franco-Russian relations in the Novosibirsk State University, and Mikhael Gorokhovski who acted as a first interviewer for this PhD proposal.

I thank all my colleagues and friends from the laboratory for maintaining positive atmosphere on the work place and for all the funny discussions during the lunch and break times. Robert, Donato, Srikanth, Gyuzel, Quan, Baolin, Pushkar, Juan, Andrea, Henri, Wesley, Cenk and all who I probably forgot to mention — thank you guys, it was a pleasure to me to spend time with you!

And of course I could not survive without all-embracing support and love of my faithful wife, Tatyana. Thank you Tanya for encouraging and believing in me till the very end of my PhD!

Contents

1. Introduction

Fluid dynamics is a very wide area of research due to the multiplicity of flow characteristics that can be encountered in nature and in experiments. In addition, researchers can also think of idealized flows that permit the advancement of theory in order to fuel models for actual flow prediction. The general method is to consider a simplified flow in which phenomena can be thoroughly studied separately. Some levels of complexity are nonetheless still difficult to grasp due to extreme regimes, an illustration of which is often found in very large Reynolds number flows. The goal of the present research thesis is therefore to address a specific regime of nonlinear interactions in a flow confined between two parallel solid walls and placed in a rapidly rotating frame. This regime of wave turbulence is yet to be fully understood, and the starting point of the present work is the model proposed by Scott [27].

Our aim is to contribute to the prediction of the dynamics of flows such as found in geophysical contexts, in which waves can be present and contribute to the overall fluid behavior. The present study is motivated by the significant effects of rotation and vertical confinement on atmospheric and oceanic flows. This is not to say that the case of pure rotation studied here is a particularly realistic model of such flows, because stratification also has important effects. However, both stratification and rotation lead to waves which have an important influence on the flow dynamics. The case of pure rotation is simpler than including both effects, which is the reason we focus on this case here: it can be considered as a stepping stone towards the full problem. Although we do not allow for stratification, it should be noted that the buoyancy force in variable density flows can be responsible for kinetic energy production in unstably stratified flows, but can also produce internal gravity waves in the case of stable stratification. This occurs in the atmosphere and ocean's thermocline and also in the case of salt-related stratification. In the ocean, internal waves are thought to be a major mechanism of energy redistribution from tidal forcing, and also to contribute to a large part of the overall energy dissipation necessary to close the balance of energy in geophysics studies. Overall, these few examples illustrate the importance of studying mechanisms of energy transport and cascade due to wave propagation, and also in contexts with boundary conditions due to walls (the ocean's bottom floor) or to interfaces (the ocean's surface) that constrain the flow geometry.

Inertial and internal gravity wave propagation is described in classical textbooks [19, 2]. The dispersion relation of inertial waves (and of internal gravity waves) depends only on the angle formed by the wavevector $\mathbf{k}$ and the axis of rotation (or the vertical in the case of gravity waves). As a result, the frequency of inertial waves is largest for wave vectors parallel to the

rotation axis and zero for wave vectors which are perpendicular to that axis. The latter are an example of flow which is two-dimensional in the sense that it does not vary in the direction of the axis. For such flows, the Coriolis force does not modify unbounded two-dimensional flow dynamics at all. In three-dimensional rotating flows, columns of fluid can be induced to move as a single structure parallel to the rotation axis, e.g. by forcing slow axial motion of a solid sphere, as shown in several experiments, e.g. [22]. These Taylor columns illustrate the specific axial coherence of rotating fluid motion, a phenomenon that can be explained by the Taylor-Proudman theorem [14]. This theorem can also be invoked in rapidly rotating turbulent flows to explain, to some extent and in an asymptotic limit, the appearance of structures elongated along the axis of rotation. In the strongly nonlinear turbulent regime, turbulent homogeneous flows submitted to uniform rotation can therefore have specific dynamics which concentrate kinetic energy towards the spectral plane perpendicular to the rotation axis.

The wave-turbulence regime which we focus on in this work is rather different from, although not entirely unconnected to, rotating strong turbulence. Wave turbulence is relevant when the turbulence is weak, being dominated by rotation rather than nonlinearity. Such turbulence consists of inertial waves, which evolve slowly under the small effects of nonlinearity and viscous dissipation. Theory tells us that, in the absence of nonlinearity and viscosity, a single wave can travel infinitely in an unbounded rotating ideal fluid at a given group velocity which describes energy transport by the wave. In actual fluids, viscosity damps the wave amplitude, and eventually kills its propagation. When considering several inertial waves, nonlinear energy exchange between triads of waves occurs when a resonance condition is met: the three wave vectors form a triangle, and a signed combination of their dispersion relations vanishes. In that case, kinetic energy is efficiently transferred from one wave to another, thus redistributing it in spectral space. In this way, energy is redistributed between different scales and wave-vector orientations. From statistical considerations, in rotating turbulence Waleffe proposed a triad instability principle resulting in an overall drain of energy towards the spectral plane perpendicular to the rotation axis [30]. In the strongly turbulent regime, non-resonant nonlinear interactions are important, as in the case of classical flows without rotation, so that the flow dynamics is a mix between wave and vortical interactions. In wave turbulence, all interactions are between resonant wave triads. This regime may be reached in different situations. For instance, the destabilization of a single wave can lead to an initially small number of resonant waves that start to populate the energy spectrum and finally lead to a broad-band distribution of energy in spectral space, and to a cascade from large to small scales, until the dissipation range is reached. A second route is via a specific forcing, with an increasing amplitude, of a rapidly rotating flow, so that the initial linear regime of propagating waves becomes a weakly nonlinear one, which can eventually become fully turbulent if sufficient energy is supplied to the system. Conversely, an initially turbulent flow may reach the wave turbulence regime after the dissipation of energy. In stably stratified turbulence, this intermediate state before ultimate viscous decay is called ‘fossil’ turbulence [10]. In the present work, we choose to

study the decay of turbulence from initial conditions which respect the wave-turbulence limit: the initial velocity field is a random motion with a Gaussian spectrum, whose parameters are chosen to comply with the wave-turbulence regime. The two parameters are the Ekman number and the Rossby number. The wave turbulence regime is reached when the Rossby number is sufficiently small — indicating the dominance of Coriolis effects over nonlinearity — and the Ekman number is also small — so that viscous dissipation is small compared with rotation. Quantitative estimates are discussed in subsection 6.2.1. Recent experimental work by Yarom and Sharon [32] has small Rossby and Ekman numbers and is thus of considerable interest in the present context. These authors measure the space-time Fourier energy spectrum as a function of the wave-vector angle, and their results indicate a concentration of energy around the inertial waves dispersion curve. However, only partial concentration is observed, and the flow is far from being fully in the wave-turbulence regime, which is expected to require still smaller Rossby and Ekman number. Thus, even the Coriolis platform in Grenoble may not provide adequately small values for these parameters.

Obviously, the direct numerical simulation (DNS) of inertial wave turbulence is faced with the same difficulty. Several authors have considered the simulation of rotating homogeneous turbulence, (see references in Godeferd and Moisy [11]) with some success considering comparisons with experimental data. In the freely decaying case, one- and two-point statistics obtained in simulations seem to match the values obtained in wind tunnels (with rotation produced by a rotating axial mean flow [15, 26]) or in tanks placed on a rotating platform and forcing by a towed grid [18]. However, both DNS and experiments are faced with the issue of limits of the fluid domain. In experiments, the flow is contained in tanks of size typically of the order of less than one meter, so that the traveling time of waves within the tank is small with respect to the rotation period, when considering standard experimental conditions of rotating turbulence. Inertial-wave reflection by the solid walls thus occurs very quickly. In addition, secondary flows from global instabilities can introduce perturbations. In DNS, when considering the most common Fourier spectral methods applied to three-dimensional periodic domains, the periodic condition is not consistent with wave propagation at most wavelengths, again producing undesired numerical confinement. For these reasons, conducting relevant direct numerical simulations in the wave-turbulence regime is difficult, an issue we will return to in section 6.5.

Faced with both these geometrical and dynamical regime constraints, one can turn to models for attempting to predict wave turbulence dynamics. This was done by Bellet et al. [3] in the unbounded case. These authors propose a two-point statistical model, which is inspired by previous quasi-Gaussian models developped during the last decades for homogeneous isotropic turbulence predictions (DIA and EDQNM models by Kraichnan [16], Orszag [25]) for rotating turbulence (Cambon et al. [8]), and for the evolution of random waves in a weakly nonlinear regime [4]. The key feature of these models is to consider the two-point correlation spectra of velocity or wave amplitude rather than the spectral coefficients themselves. An evolution equation is derived for the two-point correlation spectra, which is not closed due to nonlinearity. The

two-point equation involves the three-point moments, whose evolution equation introduces the four-point moments, and so on. The result is an infinite hierarchy of statistical moments, a well-known issue in turbulence when deriving equations for the flow statistics from the Navier-Stokes equations. This situation can be handled using a closure, the most common of which expresses the fourth-order moments in terms of the second-order ones, assuming that the spectral wave amplitudes are nearly Gaussian random variables. Although several previous authors proposed closures of this kind (Holloway and Hendershott [13], Zakharov et al. [33], Galtier [9]) the AQNM model by Bellet et al. [3] was the first one to be numerically implemented, and used for predicting wave turbulence evolution and quantitative estimates of its statistics. The numerical implementation of such models requires a robust time-marching scheme and the accurate representation of the surfaces of resonant triads in spectral space. This work was used as a starting point of the present study.

In this thesis, our goal is to consider two features of rotating flows which have never been studied in the wave-turbulence regime.

The first one is confinement: we consider a flow enclosed within two rotating parallel walls, without mean flow, the walls being perpendicular to the rotation axis. Studies of a rotating channel having a similar geometry were proposed both in experiments and numerical simulations (Kristoffersen and Andersson [17]) but most of them were for spanwise rotation. It is worth noting that Yang et al. [31] proposed a helical decomposition in a channel flow with streamwise or spanwise rotation, not wall-normal, but which is similar in spirit to our analysis in terms of helical — *i.e.* linear — mode decomposition, since linear modes in rotating turbulence match the inertial waves modes. Another parallel with the existing literature is found in the model proposed by Turner [29] for bounded turbulent rectangular channel flow, with free slip boundary conditions. This statistical model is inspired by two-point Gaussian models of EDQNM type, which, in the unbounded case, have been shown by Bellet et al. [3] to yield the wave-turbulence closure, referred to as AQNM by these authors, in the small Rossby limit of rotating turbulence. However, Turner's model requires an ad hoc 'random phase' approximation, which is not required in wave-turbulence models since, in the latter, the small Rossby number limit permits closure without this assumption (see Benney et al. [4], Bellet et al. [3], Scott [27]).

The second original feature of this work is the resolution of the three-dimensional, wave turbulence part of the flow independently of the two-dimensional component. The two-dimensional flow component consists of contributions from all wave vectors perpendicular to the rotation axis. If the flow were exactly two-dimensional rotation does not appear explicitly in its dynamics and the flow evolution can be described as exactly two-dimensional turbulence [12]. However, for wave turbulence, Scott [27] showed that in the wave-turbulence limit the two-dimensional flow decouples from the three-dimensional motion. The existence of energy transfers between 2D and 3D motion, and their intensity, is an open question for rotating strong turbulence. To our knowledge, no exact theory exists to quantify the extent to which the 2D and 3D motions interact, although partial arguments have been suggested [20] in infinite (ho-

mogeneous) rotating turbulence. For bounded rotating flows such as the one we consider, only numerical studies have been advanced, but they are challenged by the lack of resolution in the neighborhood of the 2D spectral plane, so that the rapid local variation of the transfer term is out of reach of DNS. Boundedness of the flow studied here at least allows a clear decomposition into 2D and 3D components, whose dynamics and possible interactions can then be studied. As noted earlier, in keeping with the results of Scott [27], the 3D component evolves independently of the 2D one in the wave-turbulence limit. Thus, the wave-turbulence model we use, whose derivation can be found in [27], concerns only the 3D component.

Our numerical resolution of the model proposed by Scott relies on a careful implementation of numerical schemes that preserves the necessary symmetries and conservation properties of the flow. The basic ingredients of the model are discussed in chapter 3. The implementation of the model is described in chapter 4.

Logically, the most important original part of this work concerns the quantitative results for inertial wave turbulence evolution that we report in chapter 5. We chose to explore a wide parametric range in terms of dependence on the initial conditions (the width of the initial spectrum) and on the bulk dissipation and wall-induced dissipation. One of the most spectacular spectral results is the emergence of spectral discontinuities, predicted by resonant waves theory, but whose actual existence and amplitude had to be observed. The timescale at which this spectral discontinuity appears can be estimated, but thanks to our simulations the exact scaling is available. Another highly awaited result is the way energy is redistributed in wavespace, or in other terms the pace of the cascade both in the wavenumber, k, perpendicular to the axis of rotation and in the inertial wave mode order n (which describes the discrete wave vector component parallel to the axis of rotation). Our time-evolving simulations show energy transfer from inertial waves of low to high wavenumber, as well as from low order to larger order. Both redistribution phenomena along k and n are therefore precisely demonstrated, until bulk dissipation kicks in to limit the extension of the energy cascade, and form a dissipative sub-range in the energy spectrum. From this time on, we assess the temporal power laws of energy evolution so that we are able to quantify the efficiency of the wave-turbulence cascade in a close-to-stationary similarity state.

The second important part of this PhD work was the design of a strategy aiming at the direct numerical simulation of wall-bounded inertial wave turbulence, for a possible comparison with predictions of the statistical model. The anticipated required effort is prodigious, but we decided to give it a try. The simulation platform we have chosen is a highly parallelized spectral code developed by Buffat and colleages at LMFA. This code has been used for studying the transition over a plane wall in a rotating channel [6], and for transition of the boundary layers [21], using a very high resolution of $4096 \times 512 \times 512$ grid points. For simulating inertial wave turbulence, the requirements are the following:

- in order to achieve proper boundary conditions as regards the propagation of waves out of

the computational domain, its horizontal extent has to be very large. It can be estimated from the inertial waves group velocity in the horizontal, compared with the number of wave-turbulence timescales required for a significant spectral evolution of the flow.

- Small scales have to be adequately resolved for the considered Ekman and Rossby number regime, and the inertial spectral sub-range ought to be observable, so that a very fine resolution is required.

- The computation needs to be run for long enough to permit the observation of a significant spectral evolution.

Altogether, these simulations are a considerable challenge. We must say that our final goal, which was a close comparison between the model predictions and DNS results, has not been reached. This is because, it turned out from DNS that, for the given (small) Rossby number, nonlinear transfer took place more rapidly than we had expected. The dissipative range was formed before enough rotation times had elapsed to allow wave-turbulence closure a chance of working. This means that, in an ideal world, the Rossby number should be reduced still further, but this has repercussions for the number of DNS Fourier modes that places the calculation beyond the reach of the available compute power.

Nonetheless, the DNS code has been adapted to include rotation, the initialization and spectral analysis routines required for comparison with the wave-turbulence model have been developed and DNS results were obtained. This work is described in section 6.5. We encountered difficulties related to the need to revise our strategy to fit the simulation in the available computer's memory, to the specific design of an algorithm for generating initial conditions that could be consistent with no-slip boundary conditions without triggering spurious waves, and to the extraction of the necessary data in the right dimensioning from DNS simulations to be compared with the model's results.

2. Inertial waveguide modes

Wave-turbulence analysis of decaying turbulence in a rotating channel, which is the subject of the next chapter, is based on a description of the velocity field as a combination of inviscid inertial waveguide modes. The main aim of this chapter is to explain these modes and their associated two viscous damping mechanisms: wall and volumetric.

In a frame of reference rotating with angular velocity $\mathbf{\Omega}$ (which will later be the rotational velocity of the channel walls), we non-dimensionalize using a length scale L (which will later be taken as the channel width) and the time scale $(2\Omega)^{-1}$, where $\Omega = |\mathbf{\Omega}|$. Velocity and pressure are non-dimensionalized using $2\Omega L$ and $4\rho\Omega^2 L^2$, where ρ is the fluid density. The incompressible Navier-Stokes equations are

$$\frac{\partial \mathbf{u}}{\partial t} + \underbrace{\mathbf{u}\cdot\nabla\mathbf{u}}_{\text{Convection}} + \underbrace{\hat{\mathbf{\Omega}}\times\mathbf{u}}_{\text{Rotation}} = -\nabla\Pi + \mathrm{E}\nabla^2\mathbf{u}, \tag{2.1}$$

$$\nabla\cdot\mathbf{u} = 0, \tag{2.2}$$

where $\hat{\mathbf{\Omega}}$ is a unit vector in the direction of $\mathbf{\Omega}$, the pressure variable Π incorporates the centrifugal force, $\mathrm{E} = \nu/\left(2\Omega L^2\right)$ is the Ekman number and ν the fluid viscosity. In this chapter we consider waves whose amplitude is sufficiently small that the convective term can be dropped, hence

$$\frac{\partial \mathbf{u}}{\partial t} + \hat{\mathbf{\Omega}}\times\mathbf{u} = -\nabla\Pi + \mathrm{E}\nabla^2\mathbf{u}. \tag{2.3}$$

2.1. Plane waves

Equations (2.2) and (2.3) have solutions of the form

$$\begin{pmatrix}\mathbf{u}\\ \Pi\end{pmatrix} = \begin{pmatrix}\tilde{\mathbf{u}}\\ \tilde{\Pi}\end{pmatrix}\exp(\mathrm{i}(\mathbf{K}\cdot\mathbf{x} - \omega t)), \tag{2.4}$$

where $\mathbf{K}$ is a real vector, while $\tilde{\mathbf{u}}$, $\tilde{\Pi}$ and ω are complex. Such solutions are referred to as plane waves and satisfy

$$\mathbf{K}\cdot\tilde{\mathbf{u}} = 0, \tag{2.5}$$

$$\mathrm{i}\left(\omega + \mathrm{i}\mathrm{E}K^2\right)\tilde{\mathbf{u}} - \hat{\mathbf{\Omega}}\times\tilde{\mathbf{u}} = \mathrm{i}\mathbf{K}\tilde{\Pi}, \tag{2.6}$$

where $K = |\mathbf{K}|$. Let us adopt right-handed Cartesian coordinates, (x, y, z), such that the z-axis is in the direction of $\mathbf{K}$. (2.5) implies $\tilde{\mathbf{u}}_z = 0$ and the x and y components of (2.6) give

$$\mathrm{i}\left(\omega + \mathrm{i}EK^2\right)\tilde{\mathbf{u}}_x + \hat{\Omega}_z\tilde{\mathbf{u}}_y = 0, \tag{2.7}$$

$$\mathrm{i}\left(\omega + \mathrm{i}EK^2\right)\tilde{\mathbf{u}}_y - \hat{\Omega}_z\tilde{\mathbf{u}}_x = 0. \tag{2.8}$$

The condition for a nonzero solution is

$$\left(\omega + \mathrm{i}EK^2\right)^2 = \hat{\Omega}_z^2, \tag{2.9}$$

hence

$$\omega = \pm D(\mathbf{K}) - \mathrm{i}EK^2, \tag{2.10}$$

$$\tilde{u}_y = \mp\mathrm{i}\tilde{u}_x, \tag{2.11}$$

where

$$D(\mathbf{K}) = \frac{K_\parallel}{K} \tag{2.12}$$

is the usual dispersion relation for inviscid inertial waves, $K_\parallel$ is the component of $\mathbf{K}$ parallel to the rotation vector and we have used

$$\hat{\Omega}_z = \frac{\hat{\mathbf{\Omega}}\cdot\mathbf{K}}{K} = \frac{K_\parallel}{K}. \tag{2.13}$$

To obtain a physically meaningful velocity field, we take the real part of (2.4). Writing $\tilde{u}_x = \left|\tilde{u}_x\right|\mathrm{e}^{\mathrm{i}\phi}$ and using (2.10) and (2.11), this gives

$$u_x = \left|\tilde{u}_x\right|\mathrm{e}^{-EK^2t}\cos(\mathbf{K}\cdot\mathbf{x} \mp D(\mathbf{K})t + \phi), \tag{2.14}$$

$$u_y = \pm\left|\tilde{u}_x\right|\mathrm{e}^{-EK^2t}\sin(\mathbf{K}\cdot\mathbf{x} \mp D(\mathbf{K})t + \phi), \tag{2.15}$$

which describe a vector $\mathbf{u}$ in the x-y plane of norm $\left|\tilde{u}_x\right|\mathrm{e}^{-EK^2t}$ and oriented at an angle

$$\pm\mathbf{K}\cdot\mathbf{x} - D(\mathbf{K})t \pm \phi \tag{2.16}$$

to the x-axis. This result can be visualised as follows. Imagine a line parallel to $\mathbf{K}$ and attach a velocity vector to each point on the line. These vectors are perpendicular to the line and, at any given instant, form helices according to (2.16). Depending on whether the upper or lower sign is taken, the two helices corkscrew about the line with different senses. They rotate in the same sense as t varies.

The above velocity fields are often referred to as helical modes [30]. They form the basis for spectral modelling [5] of rotating turbulence in unbounded domains, in particular the wave-turbulence analysis of [3]. However, there being no recognition of the effects of the walls, they are inappropriate for wall-confined flows, such as the channel flow.

Before including wall effects, note that (2.14) and (2.15) imply exponential decay of the wave due to viscous effects. This illustrates the dissipative mechanism which we refer to as volumetric damping because it operates throughout the flow, rather than being confined to boundary layers at the walls.

2.2. Waveguide modes

In the case of the rotating channel, there are bounding walls perpendicular to the rotation axis and separated by the channel width, h, which is taken as the length scale for non-dimensionalization. Thus, using a right-handed coordinate system, (x_1, x_2, x_3), with the x_3-axis in the direction of $\mathbf{\Omega}$, the walls lie at $x_3 = 0, 1$. Equations (2.2) and (2.3) give

$$\frac{\partial u_1}{\partial t} - u_2 = -\frac{\partial \Pi}{\partial x_1} + \mathrm{E}\nabla^2 u_1, \tag{2.17}$$

$$\frac{\partial u_2}{\partial t} + u_1 = -\frac{\partial \Pi}{\partial x_2} + \mathrm{E}\nabla^2 u_2, \tag{2.18}$$

$$\frac{\partial u_3}{\partial t} = -\frac{\partial \Pi}{\partial x_3} + \mathrm{E}\nabla^2 u_3, \tag{2.19}$$

$$\frac{\partial u_1}{\partial x_1} + \frac{\partial u_2}{\partial x_2} + \frac{\partial u_3}{\partial x_3} = 0. \tag{2.20}$$

Waveguide modes are solutions of (2.17)-(2.20) and boundary conditions at the walls (whose detailed expression, given later, depends on whether we consider inviscid or viscous modes) of the form

$$\begin{pmatrix} u_1 \\ u_2 \\ u_3 \\ \Pi \end{pmatrix} = \begin{pmatrix} \hat{u}_1(x_3) \\ \hat{u}_2(x_3) \\ \hat{u}_3(x_3) \\ \hat{\Pi}(x_3) \end{pmatrix} \exp\{\mathrm{i}(k_1 x_1 + k_2 x_2 - \omega t)\}, \tag{2.21}$$

where $\mathbf{k} = (k_1, k_2)$ is a real vector parallel to the walls, while $\hat{u}_1$, $\hat{u}_2$, $\hat{u}_3$, $\hat{\Pi}$ and ω are complex. Equations (2.17)-(2.20) give

$$\left(\mathrm{E}\left(\frac{\mathrm{d}^2}{\mathrm{d}x_3^2} - k^2\right) + \mathrm{i}\omega\right)\hat{u}_1 + \hat{u}_2 = \mathrm{i}k_1\hat{\Pi}, \tag{2.22}$$

$$\left(\mathrm{E}\left(\frac{\mathrm{d}^2}{\mathrm{d}x_3^2} - k^2\right) + \mathrm{i}\omega\right)\hat{u}_2 - \hat{u}_1 = \mathrm{i}k_2\hat{\Pi}, \tag{2.23}$$

$$\left(\mathrm{E}\left(\frac{\mathrm{d}^2}{\mathrm{d}x_3^2} - k^2\right) + \mathrm{i}\omega\right)\hat{u}_3 = \frac{\mathrm{d}\hat{\Pi}}{\mathrm{d}x_3}, \tag{2.24}$$

$$\frac{\mathrm{d}\hat{u}_3}{\mathrm{d}x_3} + \mathrm{i}(k_1\hat{u}_1 + k_2\hat{u}_2) = 0, \tag{2.25}$$

where $k = \left(k_1^2 + k_2^2\right)^{1/2}$.

2.2.1. Inviscid modes

Writing $g(x_3) = k^{-1}\hat{u}_3(x_3)$, (2.25) implies

$$k_1\hat{u}_1 + k_2\hat{u}_2 = \mathrm{i}k\frac{\mathrm{d}g}{\mathrm{d}x_3}. \tag{2.26}$$

Defining $h(x_3)$ (not to be confused with the channel width, which does not appear in the rest of this chapter) via

$$k_1\hat{u}_2 - k_2\hat{u}_1 = kh, \tag{2.27}$$

(2.26), (2.27) and the definition of $g(x_3)$ give

$$\hat{u}_1 = k^{-1}\left(\mathrm{i}k_1\frac{\mathrm{d}g}{\mathrm{d}x_3} - k_2h\right), \tag{2.28}$$

$$\hat{u}_2 = k^{-1}\left(\mathrm{i}k_2\frac{\mathrm{d}g}{\mathrm{d}x_3} + k_1h\right), \tag{2.29}$$

$$\hat{u}_3 = kg. \tag{2.30}$$

Setting $\mathrm{E} = 0$, (2.22) and (2.23) imply

$$\mathrm{i}\omega(k_1\hat{u}_1 + k_2\hat{u}_2) + k_1\hat{u}_2 - k_2\hat{u}_1 = \mathrm{i}k^2\hat{\Pi} \tag{2.31}$$

and

$$\mathrm{i}\omega(k_1\hat{u}_2 - k_2\hat{u}_1) - k_1\hat{u}_1 - k_2\hat{u}_2 = 0. \tag{2.32}$$

Hence, using (2.26) and (2.27),

$$\omega\frac{\mathrm{d}g}{\mathrm{d}x_3} - h = -\mathrm{i}k\hat{\Pi}, \tag{2.33}$$

and

$$\frac{\mathrm{d}g}{\mathrm{d}x_3} - \omega h = 0. \tag{2.34}$$

When E = 0, (2.24) and (2.30) give

$$\omega k g = -\mathrm{i}\frac{\mathrm{d}\hat{\Pi}}{\mathrm{d}x_3}. \tag{2.35}$$

Eliminating $\hat{\Pi}$ between (2.33) and (2.35) yields

$$\omega\left(\frac{\mathrm{d}^2 g}{\mathrm{d}x_3^2} - k^2 g\right) - \frac{\mathrm{d}h}{\mathrm{d}x_3} = 0. \tag{2.36}$$

Finally, elimination h between (2.34) and (2.36),

$$\left(1-\omega^2\right)\frac{\mathrm{d}^2 g}{\mathrm{d}x_3^2} + \omega^2 k^2 g = 0. \tag{2.37}$$

The inviscid boundary conditions are $\hat{u}_3 = 0$ at the walls, hence

$$g = 0 \qquad x_3 = 0, 1 \tag{2.38}$$

follows from (2.30).

(2.37) and (2.38) have solutions of the form

$$g = C \sin n\pi x_3, \tag{2.39}$$

where $C \neq 0$ is an arbitrary constant, while n takes on integer values and is referred to as the modal order. (2.37) and (2.39) imply

$$\omega^2 = \frac{n^2\pi^2}{k^2 + n^2\pi^2}. \tag{2.40}$$

When $n = 0$, $\omega = g = 0$ and $\mathrm{d}h\,/\,\mathrm{d}x_3 = 0$ according to (2.36). Thus, h is constant and (2.28)-(2.30) give

$$\hat{u}_1 = -k_2 k^{-1} h, \quad \hat{u}_2 = k_1 k^{-1} h, \quad \hat{u}_3 = 0. \tag{2.41}$$

The pressure follows from (2.33) as

$$\hat{\Pi} = -\mathrm{i}k^{-1} h. \tag{2.42}$$

This is referred to as the two-dimensional mode because it does not depend on x_3. For nonzero n, (2.40) suggests a choice of signs for ω. It is simplest to allow negative n and use $\omega = \omega_n(k)$, where

$$\omega_n(k) = \frac{n\pi}{\left(k^2 + n^2\pi^2\right)^{1/2}}. \tag{2.43}$$

That is, we associate the positive solution of (2.40) to positive n and the other solution to negative n. (2.28)-(2.30), (2.33), (2.34) and (2.39) give

$$\begin{aligned}\hat{u}_1 &= Cn\pi k^{-1}\left(\mathrm{i}k_1 - \omega_n^{-1}(k)k_2\right)\cos n\pi x_3 \\ &= \mathrm{i}C\left(k^2+n^2\pi^2\right)^{1/2}k^{-1}\left(k_1\omega_n(k)+\mathrm{i}k_2\right)\cos n\pi x_3,\end{aligned} \tag{2.44}$$

$$\begin{aligned}\hat{u}_2 &= Cn\pi k^{-1}\left(\mathrm{i}k_2 + \omega_n^{-1}(k)k_1\right)\cos n\pi x_3 \\ &= \mathrm{i}C\left(k^2+n^2\pi^2\right)^{1/2}k^{-1}\left(k_2\omega_n(k)-\mathrm{i}k_1\right)\cos n\pi x_3,\end{aligned} \tag{2.45}$$

$$\begin{aligned}\hat{u}_3 &= Ck\sin n\pi x_3 \\ &= \mathrm{i}C\left(k^2+n^2\pi^2\right)^{1/2}\left(-\mathrm{i}\frac{k}{\left(k^2+n^2\pi^2\right)^{1/2}}\sin n\pi x_3\right),\end{aligned} \tag{2.46}$$

$$\begin{aligned}\hat{\Pi} &= \mathrm{i}Cn\pi k^{-1}\left(\omega_n(k)-\omega_n^{-1}(k)\right)\cos n\pi x_3 \\ &= \mathrm{i}C\left(k^2+n^2\pi^2\right)^{1/2}\left(-\frac{k}{k^2+n^2\pi^2}\cos n\pi x_3\right),\end{aligned} \tag{2.47}$$

where we have used $\omega = \omega_n(k)$ and (2.43).

Let us compare the results with the modes given by equations (2.4)-(2.8) of [27]. When $n = 0$, (2.41) and (2.42) are in agreement provided we take $h = -\mathrm{i}$, as are (2.44)-(2.47) for $n \neq 0$ if $C = -\mathrm{i}\left(k^2+n^2\pi^2\right)^{1/2}$. These values of the constants h and C provide a particular normalisation of the modes, i.e. the one which agrees with that used in [27], which was chosen according to equation (2.11) of that article. That choice was motivated by the desire to simplify the analysis of the wave-turbulence closure.

It may be interesting to note that the inviscid waveguide modes studied here can be understood in terms of plane waves. The $n = 0$ mode is a plane wave with wave vector $\mathbf{K} = (k_1, k_2, 0)$. Modes with $n \neq 0$ can be interpreted as a combination of two plane waves. Thus, writing

$$\cos n\pi x_3 = \frac{1}{2}\left(\mathrm{e}^{\mathrm{i}n\pi x_3} + \mathrm{e}^{-\mathrm{i}n\pi x_3}\right), \quad \sin n\pi x_3 = \frac{1}{2\mathrm{i}}\left(\mathrm{e}^{\mathrm{i}n\pi x_3} - \mathrm{e}^{-\mathrm{i}n\pi x_3}\right), \tag{2.48}$$

the mode is the sum of plane waves with wave vectors $\mathbf{K} = (k_1, k_2, n\pi)$ and $\mathbf{K} = (k_1, k_2, -n\pi)$. Each of these waves is the reflection by the walls of the other. Hence the mode can be thought of as the reverberant propagation of inertial waves along the channel. Compared to the unbounded case, the component K_3 is now discrete, taking on integer multiples of π. (2.43) is the plane-wave dispersion relation.

2.2.2. Viscous modes

The no-slip conditions on the walls imply

$$\hat{u}_1 = \hat{u}_2 = \hat{u}_3 = 0 \qquad x_3 = 0, 1. \tag{2.49}$$

(2.22)-(2.25) and (2.49) form an eigenvalue problem with eigenvalue ω. Viscous dissipation means the modes decay in time, hence a negative imaginary part for ω. For general values of E this eigenvalue problem requires numerical solution. However, here we focus on the case of small E for which we expect the viscous modes to approach inviscid ones, but with small damping. It is this damping that we want to discuss.

Small E leads to thin boundary layers (referred to as Ekman layers) at the walls. These layers have thickness of order $O(\mathrm{E}^{1/2})$ to make the viscous terms in (2.22) and (2.23) comparable with the others. It is shown in [27] that small E modifies the frequency of an inviscid mode according to

$$\omega = \omega_n(k) - \mathrm{i}\Big(\mathrm{E}^{1/2} D_n(k) + \mathrm{E}\Big(k^2 + n^2\pi^2\Big)\Big), \tag{2.50}$$

where $D_n(k)$ is a complex damping coefficient given by equation (2.22) of that article. The imaginary part of $D_n(k)$ implies a small shift in the modal frequency, while the real part, which is positive, leads to modal decay. The former effect is unimportant in the model, whereas, as we shall see in later chapters, the latter can significantly affect the evolution of the turbulent energy spectra.

Given the interpretation of the inviscid modes in terms of plane waves of wave vectors $\mathbf{K} = (k_1, k_2, \pm n\pi)$, the term $\mathrm{E}\Big(k^2 + n^2\pi^2\Big) = \mathrm{E}K^2$ in (2.50) corresponds to the damping rate of plane waves in an unbounded domain. This term is referred to as volumetric damping because it corresponds to viscous dissipation everywhere in the flow. On the other hand, the real part of the term $\mathrm{E}^{1/2} D_n(k)$ represents dissipation in the boundary layers and is referred to as wall damping.

The relative importance of volumetric and wall damping depends on $K = \Big(k^2 + n^2\pi^2\Big)^{1/2}$. As discussed in [27], $\mathrm{E}^{1/2} D_n(k)$ depends only on the orientation of the vector $\mathbf{K} = (k_1, k_2, n\pi)$ relative to the rotation axis and is of $O(\mathrm{E}^{1/2})$ no matter how large K becomes. On the other hand, the volumetric damping factor, $\mathrm{E}K^2$, increases with K. The two are comparable if $K \sim \mathrm{E}^{-1/4}$, with dominant wall damping below this range and increasing importance of volumetric damping as K is increased. At large enough K, volumetric damping replaces wall damping as the dominant damping mechanism.

2.3. Summary

As discussed in section 2.1, plane waves are the basic building blocks in the theory of inertial waves. They provide a dispersion relation and the helical modes, which form the basis of

spectral analysis of the effects of rotation on turbulence in an unbounded domain.

For wall-bounded flows, such as the channel with walls perpendicular to the rotation axis which is the subject of this PhD, plane waves are insufficient because they do not allow for the walls. In section 2.2, we considered the effects of the walls, starting with the inviscid case. The resulting waveguide modes were determined and form the basis for the wave-turbulence analysis of [27]. They are a combination of two plane waves having the same frequency and wave vectors $\mathbf{K}$ with the same components, $K_1 = k_1$ and $K_2 = k_2$, parallel to the walls. On the other hand, the normal component K_3 changes sign, being $K_3 = n\pi$ for one of the waves and $K_3 = -n\pi$ for the other, where the modal order, n, takes on integer values. Thus, an important effect of boundedness is the discretization of K_3 to be a multiple of π.

As we saw in section subsection 2.2.2, the effect of small viscosity (i.e. small E) is weak damping of the modes resulting from a combination of wall and volumetric effects. The former is dominant when $K = O(1)$, but the latter increases in importance as K increases and takes over as the dominant damping mechanism for large enough K $\left(K \gg \mathrm{E}^{-1/4}\right)$.

3. Wave-turbulence closure model

This chapter describes a wave-turbulence closure (WTC) model of the rotating channel flow, which was derived in [27]. Wave-turbulence theory requires that linear terms are dominant, which, in the present case, means small Rossby number. Thus, nonlinearity takes many rotation periods to become effective. Wave-turbulence theory leads to the conclusion that nonlinear effects are dominated by *resonances*, i.e. interactions between wave triads whose frequencies sum to zero.

The unconfined, 3D case was studied in [3]. The resonant modes occur on a surface in Fourier space and nonlinear effects are represented by an integral over that surface according to wave-turbulence theory. In our case, confinement by the channel walls means that the turbulence is inhomogeneous in the cross-channel direction. As a result, Fourier analysis is restricted to the directions parallel to the walls and the wave vector is two-dimensional. Cross-channel variations of the flow are represented by Fourier series, rather than Fourier integrals. More precisely, a basis set of inertial waveguide modes, parametrised by a 2D continuous wave vector, $\mathbf{k}$, and an integer n (the modal order) is used to express the flow field. Thus, the spectral description becomes discrete in the cross-channel direction. Owing to the 2D nature of the wave vector, resonances are now associated with a curve, rather than a surface, and nonlinear effects appear as an integral over this curve (and a sum over modal orders).

A slight subtlety arises because wave-turbulence theory requires the waves to be dispersive. However, as we shall see (and as discussed in [27]) there is a particular family of modes ($n = 0$, referred to as 2D modes) whose group velocity is zero and which are consequently nondispersive. The flow is separated into two components, the 2D one and the wave one, and wave-turbulence analysis is only applied to the latter. Fortunately, it turns out (see [27] and the further discussion in Appendix B) that the energetics of the wave component are unaffected by the 2D component in the wave-turbulence limit, hence the wave-component spectra can be analysed separately (the spectral evolution equations of the wave component are closed).

In section 3.1, we describe the main ingredients of the model, while section 3.2 concerns the properties of the resonance curves. Some resonance curves can disappear as the wavenumber $|\mathbf{k}|$ is reduced below a certain critical value. This leads to a striking result of confinement, namely the appearance of discontinuous jumps in the spectra. This is the subject of section 3.3. The prediction of discontinuities is an artefact of the model. In fact, wave turbulence theory does not apply sufficiently close to a critical wavenumber and one expects rapid, but continuous variations of the spectra of confined turbulence at small Rossby number.

3.1. Governing equations

We study incompressible, decaying turbulence without mean flow confined between two infinite, parallel walls, $x_3 = 0, h$, which rotate with angular velocity $\mathbf{\Omega} = (0, 0, \Omega)$, as shown in Figure 3.1.

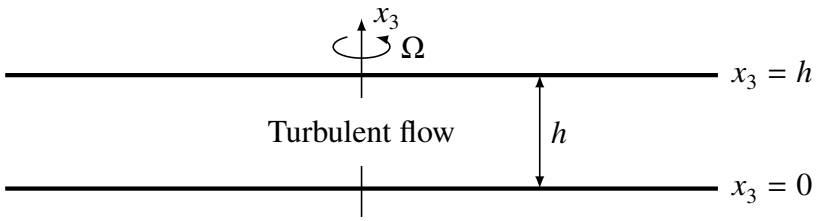

Figure 3.1.: Channel schema

The flow is governed by the Navier-Stokes equations in the frame of reference rotating with the walls. We non-dimensionalize using the length, time, velocity and pressure scales, h, $(2\Omega)^{-1}$, $2\Omega h$ and $4\rho\Omega^2 h^2$, leading to

$$\frac{\partial \mathbf{u}}{\partial t} + \mathbf{u} \cdot \nabla \mathbf{u} + \hat{\mathbf{\Omega}} \times \mathbf{u} = -\nabla \Pi + \mathrm{E}\nabla^2 \mathbf{u}, \tag{3.1}$$

$$\nabla \cdot \mathbf{u} = 0, \tag{3.2}$$

where the pressure variable, Π, includes the centrifugal force, $\hat{\mathbf{\Omega}}$ is a unit vector collinear to the angular velocity and $\mathrm{E} = \nu/(2\Omega h^2)$ is the Ekman number. Given the non-dimensionalization, the velocity components, u_i, scale with the Rossby number, which is denoted ε to suggest the smallness required by wave-turbulence closure. Small ε can be interpreted as rapid rotation and implies that the nonlinear term in (3.1), $\mathbf{u} \cdot \nabla \mathbf{u}$, is small compared with the Coriolis term, $\hat{\mathbf{\Omega}} \times \mathbf{u}$. The wall boundary conditions which accompany (3.1) and (3.2) are

$$u_i = 0, \quad x_3 = 0, 1. \tag{3.3}$$

As noted above, we will consider the limit of small Rossby number in which nonlinearity is weak and hence takes a long time to act (as we shall see later the evolution time scales as ε^{-2}). In order that viscosity does not kill the turbulence before nonlinearity becomes significant, the Ekman number is also supposed small.

The turbulence is assumed to be statistically homogeneous and isotropic [1] in the unconfined directions, x_1 and x_2, but confinement means that it is inhomogeneous with respect to the third direction. In the case of 3D homogeneous turbulence, Fourier analysis in all three directions is used, whereas here, there being only two directions of homogeneity, the basis set

employed for the velocity and pressure fields has the form $e^{i\mathbf{k}\cdot\mathbf{x}}$ where $\mathbf{k} = (k_1, k_2, 0)$ is a two-dimensional wave vector. Different choices for the basis set are possible, e.g. the linear viscous modes of the channel, but the one employed here is the inviscid modes, solutions of (3.1), (3.2) without the nonliear and viscous terms in (3.1) and subject to the inviscid boundary conditions $u_3 = 0$, $x_3 = 0, 1$.

These modes have the form

$$u_i = W_i^{(n)}(x_3; \mathbf{k})\, e^{i(\mathbf{k}\cdot\mathbf{x} - \omega_n(k)t)}, \tag{3.4}$$

$$\Pi = \Phi^{(n)}(x_3; \mathbf{k})\, e^{i(\mathbf{k}\cdot\mathbf{x} - \omega_n(k)t)} \tag{3.5}$$

and are parameterized by the wave vector $\mathbf{k}$, of norm $k = |\mathbf{k}|$, and by an integer n:

$$W_1^{(n)}(x_3; \mathbf{k}) = \frac{k_1\omega_n(k) + ik_2}{k} \cos(n\pi x_3), \tag{3.6}$$

$$W_2^{(n)}(x_3; \mathbf{k}) = \frac{k_2\omega_n(k) - ik_1}{k} \cos(n\pi x_3), \tag{3.7}$$

$$W_3^{(n)}(x_3; \mathbf{k}) = -\frac{ik}{(k^2 + n^2\pi^2)^{1/2}} \sin(n\pi x_3), \tag{3.8}$$

$$\Phi^{(n)}(x_3; \mathbf{k}) = -\frac{k}{k^2 + n^2\pi^2} \cos(n\pi x_3), \tag{3.9}$$

$$\omega_n(k) = \frac{n\pi}{(k^2 + n^2\pi^2)^{1/2}}. \tag{3.10}$$

These modes are referred to as *inertial waveguide modes* of order n. Regarding $n\pi$ as a discretized wave-vector component in the x_3 direction of the three-dimensional wave vector $\mathbf{K} = (k_1, k_2, n\pi)$ allows us to consider (3.10) as the usual dispersion relation for plane inertial waves. Writing $\cos n\pi x_3$ and $\sin n\pi x_3$ in terms of $e^{in\pi x_3}$ and $e^{-in\pi x_3}$, (3.4)-(3.9) can be interpreted as indicating the waveguide modes consist of two plane inertial waves, the one being the reflection by the walls of the other. Note that the mode $-\mathbf{k}$, $-n$ is the complex conjugate of $\mathbf{k}$, n.

The waveguide modes form a complete set for solenoidal velocity fields in the channel. Thus, we can write any velocity field satisfying (3.2) as a combination of waveguide modes:

$$u_i(\mathbf{x}, x_3, t) = \sum_{n=-\infty}^{\infty} \int \tilde{u}_n(\mathbf{k}, t) W_i^{(n)}(x_3; \mathbf{k})\, e^{i\mathbf{k}\cdot\mathbf{x}}\, d^2\mathbf{k}. \tag{3.11}$$

As noted in [27], the modes are orthogonal in the sense that (2.11) of [27] is satisfied. This leads to an expression, (2.13) of [27], for the coefficients $\tilde{u}_n(\mathbf{k}, t)$ in terms of $u_i(\mathbf{x}, t)$ which is an

inverse of the transform (3.11). Since the velocity, u_i, is real and the modes $-\mathbf{k}$, $-n$ and $\mathbf{k}$, n are conjugates, the coefficients $\tilde{u}_n$ possess the following property:

$$\tilde{u}_n^*(\mathbf{k},t) = \tilde{u}_{-n}(-\mathbf{k},t), \tag{3.12}$$

where "*" denotes complex conjugation. That is, a mode must be accompanied by its conjugate to make the velocity real. We suppress the modal oscillations by employing mode amplitudes $a_n(\mathbf{k},t)$ defined by

$$a_n(\mathbf{k},t) = \tilde{u}_n(\mathbf{k},t)\,\mathrm{e}^{\mathrm{i}\omega_n(k)t}\,. \tag{3.13}$$

Note that, in the absence of nonlinearity and viscosity, a_n is time independent. Given small Rossby and Ekman numbers, we expect slow evolution of a_n. According to [27], for small Rossby and Ekman numbers, the evolution equation of the amplitudes is

$$\frac{\partial a_n(\mathbf{k},t)}{\partial t} + \Delta_n(k)a_n(\mathbf{k},t) = \sum_{n_p,n_q=-\infty}^{\infty} \int \mathrm{e}^{\mathrm{i}\left(\omega_n(k)+\omega_{n_p}(p)+\omega_{n_q}(|\boldsymbol{k}+\boldsymbol{p}|)\right)t} N_{nn_pn_q}(\mathbf{k},\mathbf{p})a_{n_p}^*(\mathbf{p})a_{n_q}^*(-\mathbf{k}-\mathbf{p})\,\mathrm{d}^2\mathbf{p}, \tag{3.14}$$

where $N_{nn_pn_q}(\mathbf{k},\mathbf{p})$ are nonlinear coefficients given in Appendix A, which are zero unless one of the four conditions $n \pm n_p \pm n_q = 0$ is met, and

$$\Delta_n(k) = \underbrace{\mathrm{E}^{1/2}D_n(k)}_{\text{wall damping}} + \underbrace{\mathrm{E}\left(k^2+n^2\pi^2\right)}_{\text{volumetric damping}} \tag{3.15}$$

is the overall viscous damping factor of the given mode. The first term of $\Delta_n(k)$ describes viscous dissipation due to the boundary layers at the walls and contains

$$\begin{aligned} D_n(k) = \frac{\left(1-\omega_n^2(k)\right)^{1/2}}{\sqrt{2}}\Big(&\left(1+\omega_n(k)\right)^{3/2} + \left(1-\omega_n(k)\right)^{3/2} \\ &+ \mathrm{i}\Big(\left(1+\omega_n(k)\right)^{3/2} - \left(1-\omega_n(k)\right)^{3/2}\Big)\Big), \end{aligned} \tag{3.16}$$

which depends only on the direction of the three-dimensional wave vector and has a maximum when $\mathbf{K}$ is parallel to the walls. The second term represents volumetric damping and is proportional to the wavenumber squared. This reflects the usual behavior of smaller scales to dissipate energy faster then the large ones. Given the small Ekman number, $\mathrm{E}^{1/2} << \mathrm{E}$ which means that wall damping dominates over volumetric dissipation for the large scales.

The statistical characterization of turbulence uses two-point correlations of velocity amplitudes which are represented by a spectral matrix $A_{nm}(k,t)$. This matrix is defined via the statistical average of products of the modes amplitudes of orders n and m:

$$\overline{a_n^*(\mathbf{k},t)a_m(\mathbf{k}',t)} = A_{nm}(k,t)\delta(\mathbf{k}-\mathbf{k}'), \tag{3.17}$$

where δ is the Dirac function. As noted in [27], $A_{nm}(k)$ is Hermitian, i.e.

$$A_{nm}(k,t) = A^*_{mn}(k,t) \tag{3.18}$$

and positive definite. The diagonal elements ($n = m$) of this matrix are therefore real and positive. One can obtain the statistically and x_3-averaged kinetic energy using

$$\frac{1}{2}\int_0^1 \overline{u_i u_i}\,\mathrm{d}x_3 = \sum_{n=-\infty}^{\infty}\int_0^\infty \pi k A_{nn}(k,t)\,\mathrm{d}k. \tag{3.19}$$

Hence, the diagonal elements represent the distribution of energy over the modes n and horizontal wavenumbers k. Because $A_{-n-n} = A_{nn}(k)$, there are equal contributions to the energy from $-n$ and n when $n \neq 0$. The off-diagonal elements can be complex and express correlations between modes of different orders. Our aim is to study the time evolution of $A_{nm}(k,t)$ in the limit of small Rossby number. Henceforth, for simplicity's sake, we omit the time variable in the A_{nm} parameters, but it should be borne in mind.

We will not get into the details of the derivation of the wave-turbulence closure, which can be found in [27]. Here, we introduce only the overall ideas and give the resulting equation describing the time evolution of the spectral matrix.

Wave-turbulence theory is applicable to dispersive waves only. From (3.10) it follows that modes with $n = 0$ are not dispersive as their group velocity is zero. So, we separate the modes $n = 0$ from the others contributing to (3.11). These two groups of modes divide the flow into two components. The one, $n = 0$, is referred to as the *two-dimensional component* and the second as the *wave component*.

The usual assumption of asymptotic statistical independence in the limit of infinite separations leads to the representation of four-order moments as the sum of their quasi-normal values and a cumulant correction. The terms corresponding to cumulants are found to be negligible due to rapid oscillations in $\mathbf{k}$-space. Arguing in a similar way for the quasi-normal contribution and neglecting terms with rapid time oscillations, the asymptotically important part of the third-order moments is obtained using standard wave-turbulence techniques described by Newell and Rumpf [24]. The result is the following evolution equation for the diagonal elements of the spectral matrix for $n \neq 0$, namely

$$\begin{aligned}&\frac{\partial A_{nn}(k)}{\partial t} + 2\,\mathrm{Re}(\Delta_n(k))A_{nn}(k)\\ &\qquad = \sum_{n_p,n_q\neq 0}\oint_{C_{nn_pn_q}(\mathbf{k})} \frac{A_{n_pn_p}(p)\Big(\eta_{nn_pn_q}(\mathbf{k},\mathbf{p})A_{nn}(k) + \lambda_{nn_pn_q}(\mathbf{k},\mathbf{p})A_{n_qn_q}(|\mathbf{k}+\mathbf{p}|)\Big)}{\Gamma_{n_pn_q}(\mathbf{k},\mathbf{p})}|\,\mathrm{d}\mathbf{p}|,\end{aligned} \tag{3.20}$$

where Re denotes real part of a complex number and the following notation is used for the nonlinear coefficients

$$\eta_{nn_pn_q}(\mathbf{k},\mathbf{p}) = 8\,\mathrm{Re}\Big(N^*_{nn_pn_q}(\mathbf{k},\mathbf{p})N_{n_qn_pn}(-\mathbf{k}-\mathbf{p},\mathbf{p})\Big), \tag{3.21}$$

$$\lambda_{nn_pn_q}(\mathbf{k},\mathbf{p}) = 4\Big|N_{nn_pn_q}(\mathbf{k},\mathbf{p})\Big|^2, \tag{3.22}$$

and geometrical coefficient

$$\Gamma_{n_pn_q}(\mathbf{k},\mathbf{p}) = \frac{1}{\pi}\Big|\nabla_{\mathbf{p}}\sigma_{nn_pn_q}(\mathbf{p},\mathbf{k})\Big| \tag{3.23}$$

with

$$\sigma_{nn_pn_q}(\mathbf{p},\mathbf{k}) = \omega_n(k) + \omega_{n_p}(p) + \omega_{n_q}(|\boldsymbol{k}+\boldsymbol{p}|). \tag{3.24}$$

The integral is taken around a curve which is defined as the locus of points in the $\mathbf{p}$-plane for which

$$\sigma_{nn_pn_q}(\mathbf{p},\mathbf{k}) = 0 \tag{3.25}$$

for given $\mathbf{k}$, n, n_p and n_q, such that one of the conditions

$$n \pm n_p \pm n_q = 0 \tag{3.26}$$

is satisfied. We will omit the indices of $\sigma_{nn_pn_q}$ in what follows. This curve is referred to as *the resonance curve*. It defines vector triads, $(\mathbf{k},n)$, $(\mathbf{p},n_p)$ and $(-\mathbf{k}-\mathbf{p},n_q)$ such that the sum of modal frequencies is zero. The resonance curve may not exist, in which case the integral in (3.20) should be taken to be zero. Figure 3.2 shows the resonance curves for a particular choice, $n = 1$, $k = 10$, and all n_p, n_q satisfying $n \pm n_p \pm n_q = 0$. As we shall see, each loop corresponds to a particular choice of n_p, n_q. The following section describes the properties of such curves.

Recalling that the velocity is $O(\varepsilon)$, $A_{nm}(k)$ is $O(\varepsilon^2)$. Hence, from equation (3.20) it follows that the $A_{nn}(k)$ evolution time scale is $O(\varepsilon^{-2})$. It is shown in [27] that the two-dimensional component evolves independently[1] on the usual large-scale turnover time, $t = O(\varepsilon^{-1})$, and makes the off-diagonal elements decay on a time scale asymptotically smaller then $O(\varepsilon^{-2})$.

Two important results concerning realizability and energy conservation follow from equation (3.20). The former is that $A_{nn}(k)$ never become negative. The later is that, without viscous dissipation, the $n \neq 0$ part of the energy is conserved. Moreover, one can show that the truncated version of (3.20) respects equipartition in the absence of dissipation (see Appendix C for the details).

Given $A_{-n-n} = A_{nn}$, we restrict attention to $n > 0$ from here on. We also use isotropy in the horizontal directions by choosing axes, x_1, x_2, such that $\mathbf{k} = (k, 0)$.

[1] In [27], the reasoning relies on various identities based on numerical evidence. Appendix B provides analytical proofs of these identities.

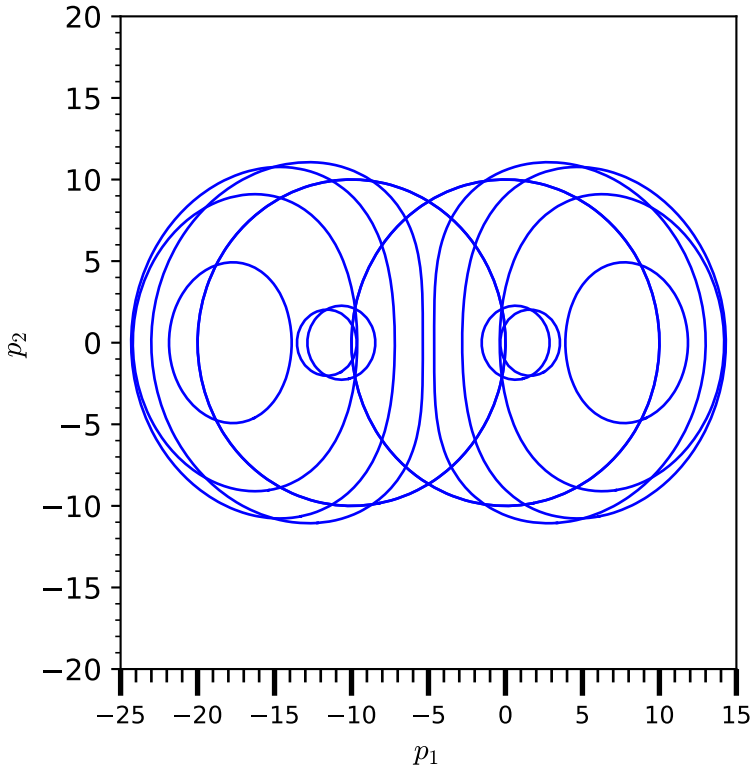

Figure 3.2.: Resonance curves in the **p**-plane for $n = 1$, $k = 10$

3.2. Properties of the resonance curve

The purpose of this section is to investigate the existence and topology of the resonance curve. It should be borne in mind that $n_p, n_q \neq 0$ and one of the four conditions (3.26) is satisfied.

First, note that, for given values of n, n_p, n_q and $\mathbf{k} = (k, 0)$, the left-hand side of (3.25) is a smooth function of $\mathbf{p}$ which tends to $\omega_n(k) > 0$ as $p \to \infty$. Thus, the resonance curve does not extend to infinite p. Note that there is no resonance curve if $n_p, n_q > 0$ because $\omega_n(k)$, $\omega_{n_p}(p)$ and $\omega_{n_q}(|\mathbf{k} + \mathbf{p}|)$ are all positive. Thus, we assume $n_p < 0$ or $n_q < 0$ below. Note also that σ, and hence the resonance curve, is symmetric under the reflection $p_2 \mapsto -p_2$.

3.2.1. $k = 0$

When $\mathbf{k} = 0$, (3.25) becomes

$$1 + \omega_{n_p}(p) + \omega_{n_q}(p) = 0. \tag{3.27}$$

Unless $n_p, n_q < 0$, there are no solutions of (3.27). On the other hand, if $n_p, n_q < 0$, the left-hand side of (3.27) increases monotonically from -1 at $p = 0$ to $+1$ at $p = \infty$. Thus, the resonance

curve exists when $n_p, n_q < 0$ and consists of a circle, $p = r_{n_p n_q}$, in the $\mathbf{p}$ plane, where $r_{n_p n_q}$ is the solution of (3.27) for these n_p, n_q.

Having dealt with the case $\mathbf{k} = 0$, we restrict attention to $\mathbf{k} \neq 0$ in what follows.

3.2.2. $k \to \infty$

As $k \to \infty$ for given n, n_p and n_q, if p remains finite, (3.25) cannot be satisfied because the first and third terms in (3.24) tend to zero, whereas the second does not. Thus, $p \to \infty$. Likewise, if $|\mathbf{k} + \mathbf{p}|$ remains finite, the first and second terms approach zero, while the third does not. Hence, $p \to \infty$ and $|\mathbf{k} + \mathbf{p}| \to \infty$, so (3.25) takes the approximate form

$$\frac{n}{k} + \frac{n_p}{p} + \frac{n_q}{|\mathbf{k} + \mathbf{p}|} = 0. \tag{3.28}$$

Without loss of generality, we assume $n_p < 0$. Otherwise, renaming $n_p \leftrightarrow n_q$ and $\mathbf{p} \leftrightarrow -\mathbf{k} - \mathbf{p}$ make (3.25) still satisfied. If p goes to infinity faster then k, i.e. $p/k \to \infty$, the left-hand side of (3.28) multiplied by k tends to $n > 0$, whereas it approaches $-\infty$ as $p/k \to 0$. This implies that the resonance curve always exists for big enough k. It is shown in Appendix D that the curve consists of a single loop.

3.2.3. Finite nonzero k

As k varies, the number of loops of the resonance curve may change. This occurs if $\sigma = 0$ and $\nabla_{\mathbf{p}}\sigma = 0$ leading to

$$\frac{n\pi}{\left(k^2 + n^2\pi^2\right)^{1/2}} + \frac{n_p\pi}{\left(p^2 + n_p^2\pi^2\right)^{1/2}} + \frac{n_q\pi}{\left(|\mathbf{k} + \mathbf{p}|^2 + n_q^2\pi^2\right)^{1/2}} = 0, \tag{3.29}$$

and

$$\frac{n_p\pi\mathbf{p}}{\left(p^2 + n_p^2\pi^2\right)^{3/2}} + \frac{n_q\pi(\mathbf{k} + \mathbf{p})}{\left(|\mathbf{k} + \mathbf{p}|^2 + n_q^2\pi^2\right)^{3/2}} = 0. \tag{3.30}$$

Solutions, k, $\mathbf{p}$, of (3.29) and (3.30) are referred to as *critical points*. Note that (3.29) and (3.30) are invariant under the symmetry $n_p \leftrightarrow n_q$, $\mathbf{p} \leftrightarrow -\mathbf{k} - \mathbf{p}$. Thus, critical points with $n_p \neq n_q$ occur in symmetric pairs having the same k.

Appendix E describes a procedure for solution of (3.29) and (3.30) allowing the determination of critical points. Numerical implementation of this procedure was carried out. Of course, the infinity of possible n, n_p and n_q cannot all be treated numerically, so the modal orders were restricted to $0 < n$, $|n_p|$, $|n_q| \leq n_{max}$ ($n_{max} = 20$). It was found that a single critical point, k_c, $\mathbf{p}_c = (p_{c1}, 0)$, exists provided n_p and n_q have opposite signs, otherwise there are none. Although we have no analytical proof of this result, we assume it to hold.

Let k_c and $\mathbf{p}_c = (p_{c1}, 0)$ represent a critical point. Taylor's expansion of $\sigma(\mathbf{p}, k)$ gives

$$\sigma(\mathbf{p}, k) \sim \kappa(k - k_c) + \frac{1}{2}\sum_{i,j=1}^{2} D_{ij}(p_i - p_{ci})(p_j - p_{cj}), \tag{3.31}$$

where

$$\kappa = \frac{\partial\sigma}{\partial k}(\mathbf{p}_c, k_c), \quad D_{ij} = \frac{\partial^2\sigma}{\partial p_i \partial p_j}(\mathbf{p}_c, k_c). \tag{3.32}$$

Writing

$$\sigma(\mathbf{p}, k) = \omega_n(k) + \omega_{n_p}\left(\left(p_1^2 + p_2^2\right)^{1/2}\right) + \omega_{n_q}\left(\left((k + p_1)^2 + p_2^2\right)^{1/2}\right) \tag{3.33}$$

we obtain

$$\kappa = \omega_n'(k_c) + \operatorname{sgn}(k_c + p_{c1})\omega_{n_q}'\left(\left|k_c + p_{c1}\right|\right), \tag{3.34}$$

$$D_{ij} = \begin{bmatrix} \mu_1 & 0 \\ 0 & \mu_2 \end{bmatrix}, \tag{3.35}$$

$$\mu_1 = \omega_{n_p}''\left(\left|p_{c1}\right|\right) + \omega_{n_q}''\left(\left|k_c + p_{c1}\right|\right), \tag{3.36}$$

$$\mu_2 = \left|p_{c1}\right|^{-1}\omega_{n_p}'\left(\left|p_{c1}\right|\right) + \left|k_c + p_{c1}\right|^{-1}\omega_{n_q}'\left(\left|k_c + p_{c1}\right|\right), \tag{3.37}$$

where ω_n' and ω_n'' are the first and second derivatives of $\omega_n(k)$.

(3.34), (3.36) and (3.37) were numerically evaluated for each of the critical points obtained as described above. We found that $\kappa < 0$ and $\mu_1, \mu_2 > 0$. As $k \to \infty$, we saw earlier that the resonance curve exists and forms a single loop. As k decreases, a change in the number of loops requires a critical point which, as we have seen, exists only if n_p and n_q have opposite signs. As $k \searrow k_c$, (3.31) yields a resonance curve which approaches

$$\mu_1(p_1 - p_{c1})^2 + \mu_2 p_2^2 = -2\kappa(k - k_c). \tag{3.38}$$

since $\kappa < 0$ and $\mu_1, \mu_2 > 0$, this implies that the resonance curve disappears via a small ellipse as k decreases through k_c.

We conclude that, when it exists, the resonance curve consists of a single loop. It is present for all k if $n_p, n_q < 0$, but only when $k > k_c$ if n_p and n_q have opposite signs.

3.3. Spectral discontinuities

For given n and n_p, n_q of opposite signs, let $\mathbf{k}_c = (k_c, 0)$ and $\mathbf{p}_c = (p_{c1}, 0)$ represent the associated critical point. The resulting contribution of the integral to (3.20) is zero if $k < k_c$ and we

now evaluate it as k increases through k_c. From (3.31) and (3.35),

$$\Gamma_{n_p n_q}(\mathbf{k},\mathbf{p}) \sim \frac{1}{\pi}\left(\mu_1^2(p_1 - p_{c1})^2 + \mu_2^2 p_2^2\right)^{1/2} \tag{3.39}$$

in the neighborhood of the critical point. Appendix F demonstrates that the integral on the

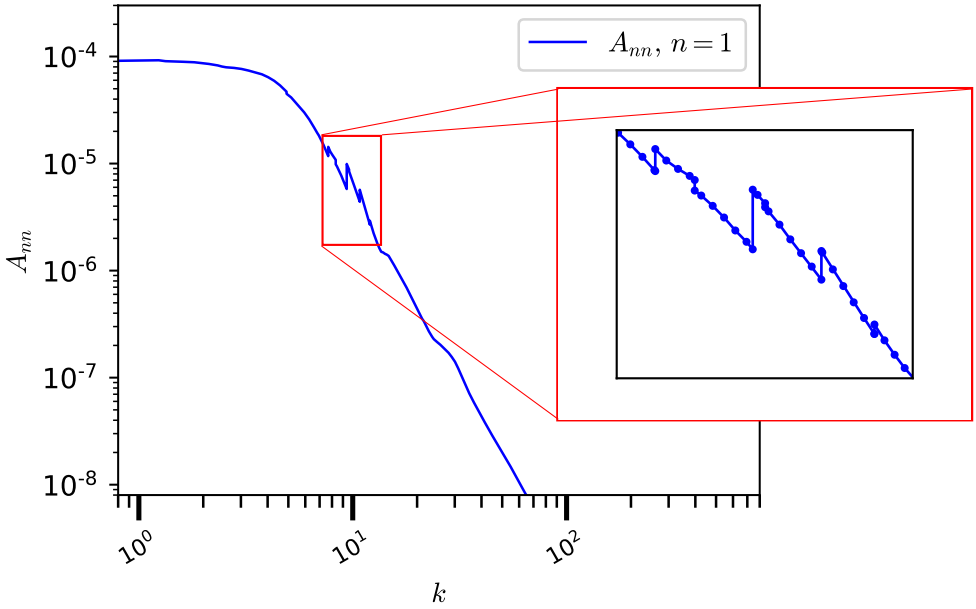

Figure 3.3.: Example of spectral discontinuities.

right-hand side of (3.20) approaches the limiting form

$$\frac{2\pi^2}{(\mu_1\mu_2)^{1/2}} A_{n_p n_p}(p_c)\left(\eta_{n n_p n_q}(\mathbf{k}_c,\mathbf{p}_c)A_{nn}(k) + \lambda_{n n_p n_q}(\mathbf{k}_c,\mathbf{p}_c)A_{n_q n_q}\left(\left|\mathbf{k}_c + \mathbf{p}_c\right|\right)\right) \tag{3.40}$$

as $k \searrow k_c$. Thus, the integral in (3.20) has a discontinuous jump, from zero to (3.40), as k increases through k_c. As a result, spectral evolution according to (3.20) will introduce discontinuous jumps in the spectra, $A_{nn}(k)$, even if the initial spectra are smooth. This is illustrated by Figure 3.3, which shows a typical result of numerical solution of (3.20). Such jumps do not occur in the unconfined 3D case studied in [3] because the equivalent of the integral in (3.20) is over a (resonant) surface whose area goes to zero as critical point is approached sufficiently rapidly that the limiting value of the integral is zero. The jumps are thus symptomatic of confinement.

The discontinuities of $A_{nn}(k)$ are an artefact of wave-turbulence asymptotics, which break down in a small neighborhood, $k - k_c = O(\varepsilon^2)$, of the critical point. In reality, we expect rapid, but not discontinuous variation as k passes through k_c, with wave-turbulence theory applying outside $k - k_c = O(\varepsilon^2)$.

4. WTC implementation

As described in the previous chapter, wave-turbulence closure leads to evolution equations, (3.20), for the energy density in spectral space. Nonlinear effects appear in these equations as integrals over resonance curves. Numerical evaluation of these integrals constitutes the core part of the implementation. Spectral discontinuities, discussed in section 3.3 and which reflect the appearance/disappearance of resonance curves, also require some care.

In this chapter, we present the most important ingredients of the numerical implementation. Section 4.1 provides a precise definition of the Rossby number, ε, and corresponding rescalings of the spectra and time variable which lead to elimination of the Rossby number as a parameter in the numerical problem to be solved. In section 4.2, symmetries are employed to reduce the subsequent numerical cost of evaluating the integrals around the resonance curves. Spectral discretization and truncation are introduced in section 4.3. Section 4.4 describes the numerical evaluation of the integrals around the resonance curve. In section 4.5, the numerical scheme used for time discretization is discussed. Section 4.6 describes the organisation of the program resulting from the numerical implementation.

The code was first developed in FORTRAN in serial form, then parallelized using MPI. Section 4.7 discusses parallelization and its scaling with the number of available processes.

Finally, section 4.8 concerns various checks on the accuracy of the code which were undertaken to verify its correctness, as well as results which show that the truncated inviscid model leads to equipartition of energy.

4.1. Rescaling and a precise definition of the Rossby number

Since, as noted in the previous chapter, $A_{nn}(k)$ and its nonlinear evolution time scale are respectively $O(\varepsilon^2)$ and $O(\varepsilon^{-2})$, it is natural to introduce the $O(1)$ variables $B_n(k) = \varepsilon^{-2} A_{nn}(k)$ and $T = \varepsilon^2 t$, leading to

$$\frac{\partial B_n(k)}{\partial T} = \alpha_n(k) B_n(k) + \tau_n(k) \tag{4.1}$$

for $n \neq 0$, where

$$\alpha_n(k) = J_n(k) - 2\varepsilon^{-2} \operatorname{Re}(\Delta_n(k)), \tag{4.2}$$

$$J_n(k) = \sum_{n_p,n_q} \oint_{C_{nn_pn_q}(\mathbf{k})} \frac{\eta_{nn_pn_q}(\mathbf{k},\mathbf{p}) B_{n_p}(p)}{\Gamma_{n_pn_q}(\mathbf{k},\mathbf{p})} |\,\mathrm{d}\mathbf{p}|, \tag{4.3}$$

$$\tau_n(k) = \sum_{n_p,n_q} \oint_{C_{nn_pn_q}(\mathbf{k})} \frac{\lambda_{nn_pn_q}(\mathbf{k},\mathbf{p}) B_{n_p}(p) B_{n_q}(|\mathbf{k}+\mathbf{p}|)}{\Gamma_{n_pn_q}(\mathbf{k},\mathbf{p})} |\,\mathrm{d}\mathbf{p}|. \tag{4.4}$$

Here, Re denotes the real part of a complex number and the sums in (4.3) and (4.4) are over all $n_p, n_q \neq 0$ such that one of the four conditions $n \pm n_p \pm n_q = 0$ is satisfied. Because $B_{-n} = B_n$, equation (4.1) need only be applied for $n > 0$ and we assume this henceforth. For the same reason, we replace B_{n_p} and B_{n_q} by $B_{|n_p|}$ and $B_{|n_q|}$ in (4.3) and (4.4). The viscous damping factor

$$2\varepsilon^{-2}\,\mathrm{Re}(\Delta_n(k)) = \beta_w \frac{\left(1-\omega_n^2(k)\right)^{1/2}}{\sqrt{2}} \Big((1+\omega_n(k))^{3/2} + (1-\omega_n(k))^{3/2} \Big) + \beta_v \left(k^2 + n^2\pi^2\right) \tag{4.5}$$

contains two parameters, $\beta_w = 2\varepsilon^{-2}\mathrm{E}^{1/2}$ and $\beta_v = 2\varepsilon^{-2}\mathrm{E}$, which respectively measure the importance of wall and volumetric damping. Since E is small, $\beta_v \ll \beta_w$ and wall damping generally dominates for the large scales. However, volumetric damping becomes significant if $k^{-1}\left(k^2+n^2\pi^2\right)^{3/2}$ is large, of order $\mathrm{E}^{-1/2}$. This happens at small scales, when $k^2+n^2\pi^2$ is large, and also at small $k/(|n|\pi)$, i.e. when the three-dimensional wave vector is nearly vertical.

We choose to define ε such that the initial wave-component energy equals ε^2, i.e.

$$2\pi \sum_{n=1}^{\infty} \int_0^{\infty} k B_n(k,0)\ \mathrm{d}k = 1, \tag{4.6}$$

which is obtained from (3.19) using $B_{-n} = B_n$. The initial spectra are taken as

$$B_n(k,0) = C \exp\left[-\frac{k^2+n^2\pi^2}{\Xi^2} \right], \tag{4.7}$$

where Ξ determines the spectral width and the constant C is calculated using (4.6) as

$$C = \frac{1}{\pi\Xi^2 \sum_{n=1}^{\infty} \mathrm{e}^{-n^2\pi^2/\Xi^2}}. \tag{4.8}$$

(4.7) implies that the large scales contain most of the energy. Note that the parameters of the problem are β_w, β_v and Ξ.

4.2. Consequences of symmetry

$C_{nn_pn_q}(\mathbf{k})$, $\lambda_{nn_pn_q}(\mathbf{k},\mathbf{p})$ and $\Gamma_{n_pn_q}(\mathbf{k},\mathbf{p})$ are symmetric under the transformation $n_p \leftrightarrow n_q$, $\mathbf{p} \leftrightarrow -\mathbf{k}-\mathbf{p}$. Thus, we can combine $n_p < n_q$ and $n_p > n_q$ to obtain

$$J_n(k) = \sum_{n_p,n_q} \zeta_{n_pn_q} \oint_{C_{nn_pn_q}(\mathbf{k})} \frac{\eta_{nn_pn_q}(\mathbf{k},\mathbf{p})B_{|n_p|}(p) + \eta_{nn_qn_p}(\mathbf{k},-\mathbf{k}-\mathbf{p})B_{|n_q|}(|\mathbf{k}+\mathbf{p}|)}{\Gamma_{n_pn_q}(\mathbf{k},\mathbf{p})} |\,\mathrm{d}\mathbf{p}|, \tag{4.9}$$

$$\tau_n(k) = 2\sum_{n_p,n_q} \zeta_{n_pn_q} \oint_{C_{nn_pn_q}(\mathbf{k})} \frac{\lambda_{nn_pn_q}(\mathbf{k},\mathbf{p})B_{|n_p|}(p)B_{|n_q|}(|\mathbf{k}+\mathbf{p}|)}{\Gamma_{n_pn_q}(\mathbf{k},\mathbf{p})} |\,\mathrm{d}\mathbf{p}| \tag{4.10}$$

from (4.3) and (4.4), where $\zeta_{n_pn_q}$ takes the value 1/2 if $n_p = n_q$ and 1 otherwise and the sums are taken over all $n_p, n_q \neq 0$, $n_p \leq n_q$ such that one of the conditions $n \pm n_p \pm n_q = 0$ is met. Since the resonance curve only exists if $n_p < 0$ or $n_q < 0$, terms in (4.9) and (4.10) with $n_p > 0$ are zero. Thus, we further restrict attention to $n_p < 0$.

Taking $\mathbf{k} = (k, 0)$, $C_{nn_pn_q}(\mathbf{k})$ and the integrands in (4.9) and (4.10) are symmetric under reflection about the p_1-axis, i.e. $p_2 \leftrightarrow -p_2$. Thus, we can restrict the integrals to the part of the resonance curve in $p_2 \geq 0$, then multiply the results by 2.

4.3. Truncation and discretization

In the mathematical model, (4.1), the wavenumber, k, can take any real value in $k \geq 0$ and the modal order, n, any positive integer value. From a numerical point of view, truncation and discretization are needed. Thus, we work with the spectra, $B_n(k)$, for $0 \leq k \leq k_{max}$, $0 < n \leq n_{max}$ and discretize k to a finite set of points. For each $0 < n \leq n_{max}$, the discrete values of k are written $0 = k_{0,n} < k_{1,n} < \cdots < k_{N_n,n} = k_{max}$, where N_n is the number of discrete values for the given n. These values are the amalgamation of two sets. The first, $0 = k_0 < k_1 < \cdots < k_N = k_{max}$, is independent of n and given by

$$k_i = \chi\left(\exp\left[\frac{i}{N}\ln\left(1 + k_{max}/\chi\right)\right] - 1\right), \tag{4.11}$$

where χ is a user specified numerical parameter, comparable in magnitude to the initial spectral width, Ξ. Observe that, for $k_i \gg \chi$, the term -1 in the above equation is negligible and the k_i follow an exponential law. This has the advantage over evenly spaced k_i of reducing the number of required wavenumbers, thus decreasing the calculation time.

The second set of wavenumbers varies with n. For any given n, it consists of all critical $k_c \leq k_{max}$ for $-n_{max} \leq n_p < 0$ and $0 < n_q \leq n_{max}$ such that $n \pm n_p \pm n_q = 0$. Recall from the discussion in subsection 3.2.3 and section 3.3 that $B_n(k)$ has a discontinuous jump at each critical wavenumber. The limiting value as $k \nearrow k_c$ is denoted by $B_n^<$, while as $k \searrow k_c$, it is $B_n^>$.

The appearance of these wavenumbers among those to which $B_n(k)$ is discretized avoids interpolation across discontinuities when numerically evaluating the integrals in (4.9) and (4.10), which improves the precision of the numerical approximation of these integrals.

Given the use of double precision throughout the implementation, it is highly unlikely that there is a precise coincidence between a critical wavenumber and one of the k_i. Thus, the two sets, k_i and all k_c for the given n, are combined in order to produce the $k_{i,n}$. The spectra are represented by discrete values $B_n^<(k_{i,n})$ and $B_n^>(k_{i,n})$, where, since the spectra are continuous when $k_{i,n}$ is other then a critical wavenumber, $B_n^< = B_n^>$ for such $k_{i,n}$.

4.4. Integration over a resonance curve

Numerical evaluation of (4.9) and (4.10) requires integration over a resonance curve for given n, n_p, n_q and $\mathbf{k}$. To this end we first introduce a parametrization of the resonance curves.

4.4.1. Resonance-curve parametrization

Since (3.25) is unchanged by $p_2 \mapsto -p_2$ when $\mathbf{k} = (k, 0)$, the resonance curve is reflection symmetric. Because it consists of a single loop, it crosses the p_1-axis at just two points, $p_1 = P^-(k; n, n_p, n_q)$ and $p_1 = P^+(k; n, n_p, n_q)$, these points being the solutions of

$$\omega_n(k) + \omega_{n_p}(|p_1|) + \omega_{n_q}(|k + p_1|) = 0, \tag{4.12}$$

ordered as $P^- < P^+$. Like the resonance curve, these solutions exist only if $n_p, n_q < 0$ or if $k > k_c$ and n_p, n_q have opposite signs.

The quantities P^+ and P^- are determined as follows. As noted earlier, the sums in (4.9) and (4.10) can be restricted to $n_p < 0$. Thus, we suppose negative n_p in what follows. There are two cases:

i) If $n_q < 0$, the left-hand side of (4.12) is negative when $p_1 = 0$ and positive as $|p_1| \to \infty$. Hence, $P^- < 0$ and $P^+ > 0$. Starting at $p_1 = 0$, we step through increasing integer values of p_1 until the left-hand side of (4.12) becomes positive or zero. This provides an interval in which P^+ is to be found. Interval halving is then used to refine the solution to a user-prescribed precision. A similar procedure (stepping downwards from $p_1 = 0$ through integer values, then using interval having) yields P^-.

ii) If $n_q > 0$, there is a critical wavenumber $k = k_c$ with $p_1 = p_{c1} > 0$. With this value of p_1, the left-hand side of (4.12) is a decreasing function of $k \geq k_c$, from its value of 0 when $k = k_c$. Thus, the left-hand side of (4.12) is negative for $p_1 = p_{c1}$ in the range $k > k_c$ for which the resonance curve exists. It follows that $P^- < p_{c1}$ and $P^+ > p_{c1}$.

Marching upwards from p_{c1} in steps of 1, yields an interval containing P^+ and interval halving allows refinement to a required precision. P^- is obtained similarly.

The resonance curve follows the differential equation

$$\frac{\mathrm{d}\mathbf{p}}{\mathrm{d}s} = (-Z_2, Z_1), \tag{4.13}$$

where s is a parameter and $\boldsymbol{Z}$ is the vector

$$\boldsymbol{Z} = -\nabla_{\mathbf{p}}\sigma = \frac{\pi n_p \mathbf{p}}{\left(p^2 + n_p^2\pi^2\right)^{3/2}} + \frac{\pi n_q(\mathbf{k}+\mathbf{p})}{\left(|\mathbf{k}+\mathbf{p}|^2 + n_q^2\pi^2\right)^{3/2}}. \tag{4.14}$$

As $p \to \infty$, σ approaches the positive value $\omega_n(k)$. Thus, it is positive outside and negative inside the resonance curve. Hence, $\nabla_{\mathbf{p}}\sigma$ yields an outward normal vector on the curve. It follows from (4.13) and the first equality in (4.14) that increasing s corresponds to following the curve in a clockwise sense. We use fourth-order Runge-Kutta integration of (4.13) to follow $\mathbf{p}(s)$ along the resonance curve towards increasing s starting from $\mathbf{p}(0) = (P^-, 0)$. At each step, the step length, Δs, is first determined using

$$\Delta s = \delta \frac{P^+ - P^-}{|\boldsymbol{Z}|}, \tag{4.15}$$

where δ is a small, user defined parameter. The idea is to keep $|\Delta\mathbf{p}|$ close to $\delta(P^- - P^+)$, a small fraction of the overall perimeter of the resonance curve. Integration stops when $p_2 \le 0$ and the final values of $\mathbf{p}$ (which should be $\mathbf{p} = (P^+, 0)$) and $s = s_{max}$ are then refined to fourth-order precision. Thus, we step along the upper half ($p_2 \ge 0$) of the resonance curve.

4.4.2. Calculations of J_n and τ_n

We now apply the above parametrization to the integrals in (4.9) and (4.10) with $\mathbf{k} = (k, 0)$, using the previously noted symmetry $p_2 \leftrightarrow -p_2$. According to (3.23), (4.13) and (4.14), $|\,\mathrm{d}\mathbf{p}| = \pi\Gamma_{n_p n_q}(\mathbf{k}, \mathbf{p})\,\mathrm{d}s$. Thus,

$$\begin{aligned} J_n &= 2\pi \sum_{n_p, n_q} K_1^{n n_p n_q}, \\ \tau_n &= 4\pi \sum_{n_p, n_q} K_2^{n n_p n_q}, \end{aligned} \tag{4.16}$$

where the sums are over all $-n_{max} \le n_p < 0$, $n_p \le n_q \le n_{max}$, $n_q \neq 0$ such that one of the conditions $n \pm n_p \pm n_q = 0$ is met and

$$\begin{aligned} K_1^{nn_pn_q} &= \zeta_{n_pn_q} \int_0^{s_{max}} \left(\eta_{nn_pn_q}(\mathbf{k}, \mathbf{p}) B_{|n_p|}(p) + \eta_{nn_qn_p}(\mathbf{k}, -\mathbf{k}-\mathbf{p}) B_{|n_q|}(|\mathbf{k}+\mathbf{p}|) \right) \mathrm{d}s, \\ K_2^{nn_pn_q} &= \zeta_{n_pn_q} \int_0^{s_{max}} \lambda_{nn_pn_q}(\mathbf{k}, \mathbf{p}) B_{|n_p|}(p) B_{|n_q|}(|\mathbf{k}+\mathbf{p}|) \, \mathrm{d}s. \end{aligned} \tag{4.17}$$

Note the multiplicative factor 2 in (4.16), which arises from employing reflection symmetry.

At each step of marching along the resonance curve, the contributions to the integrals (4.17) are calculated and added into running totals which yield numerical approximations to the integrals after the final step. If $p = |\mathbf{p}|$ or $q = |\mathbf{k}+\mathbf{p}|$ cross one of the discrete spectral values, $k_{i,n}$, during the step, subintervals are used. The boundaries between subintervals are the points where p or q cross a discrete wavenumber, determined by linear interpolation across the step. Subintervals with $p > k_{max}$ or $q > k_{max}$ do not contribute to the integrals. The integrand is evaluated using linear interpolation at the midpoint of each subinterval and multiplied by the extent of the subinterval in s to obtain the contribution to the integral, i.e. a trapezoidal-style rule is applied. Interpolation across the entire step is used for the coefficients $\lambda_{nn_pn_q}(\mathbf{k}, \mathbf{p})$, $\eta_{nn_pn_q}(\mathbf{k}, \mathbf{p})$ and $\eta_{nn_qn_p}(\mathbf{k}, -\mathbf{k}-\mathbf{p})$, while the spectra are determined by interpolation between two consecutive discrete values of k, hence respecting spectral discontinuities.

The above procedure can be applied without further ado to calculate J_n and τ_n at all discrete wavenumbers, $k_{i,n}$, other then $k_{0,n} = 0$ and critical wavenumbers. These special cases require more care and are treated as follows.

4.4.3. $k = 0$

The problem with $k = 0$ is that it leads to division by zero in (A.2), which is used to calculate the coefficients $\eta_{nn_pn_q}(\mathbf{k}, \mathbf{p})$ and $\lambda_{nn_pn_q}(\mathbf{k}, \mathbf{p})$. Thus, we consider the limit $k \to 0$. Using the results given in Appendix A, we find

$$N_{nn_pn_q}(\mathbf{k}, \mathbf{p}) \to \frac{1}{2} p^{-1} (p_2 - \mathrm{i}p_1) \Lambda_{nn_pn_q}(p), \tag{4.18}$$

$$N_{n_qn_pn}(-\mathbf{k}-\mathbf{p}, \mathbf{p}) \to \frac{1}{4} p^{-1} (p_2 - \mathrm{i}p_1) \Xi_{nn_pn_q}(p), \tag{4.19}$$

where $\Lambda_{nn_pn_q}(p)$ and $\Xi_{nn_pn_q}(p)$ (not to be confused with the spectral width Ξ) are real functions given by (A.4) and (A.5). In particular, $\Lambda_{nn_pn_q}(p)$ possesses the property of antisymmetry with respect to $n_p \leftrightarrow n_q$.

As we saw in subsection 3.2.1, the resonance curve for $k = 0$ consists of the circle $p = r_{n_pn_q}$. Thus, (3.21)-(3.23), (4.14), (4.18) and (4.19) yield

$$\eta_{nn_pn_q}(\mathbf{k}, \mathbf{p}) = \Lambda_{nn_pn_q}(r_{n_pn_q}) \Xi_{nn_pn_q}(r_{n_pn_q}), \tag{4.20}$$

$$\lambda_{nn_pn_q}(\mathbf{k},\mathbf{p}) = \Lambda^2_{nn_pn_q}(r_{n_pn_q}), \tag{4.21}$$

$$\Gamma_{n_pn_q}(\mathbf{k},\mathbf{p}) = r_{n_pn_q}\gamma_{n_pn_q}(r_{n_pn_q}) \tag{4.22}$$

on the resonance curve, where

$$\gamma_{n_pn_q}(p) = \left| \frac{n_p}{\left(p^2 + n_p^2\pi^2\right)^{3/2}} + \frac{n_q}{\left(p^2 + n_q^2\pi^2\right)^{3/2}} \right|. \tag{4.23}$$

Given these results, evaluation of the integrals in (4.3) and (4.4) gives

$$J_n(0) = 2\pi \sum_{n_p,n_q} \frac{\Lambda_{nn_pn_q}(r_{n_pn_q})\Xi_{nn_pn_q}(r_{n_pn_q})}{\gamma_{n_pn_q}(r_{n_pn_q})} B_{|n_p|}(r_{n_pn_q}), \tag{4.24}$$

$$\tau_n(0) = 2\pi \sum_{n_p,n_q} \frac{\Lambda^2_{nn_pn_q}(r_{n_pn_q})}{\gamma_{n_pn_q}(r_{n_pn_q})} B_{|n_p|}(r_{n_pn_q})B_{|n_q|}(r_{n_pn_q}), \tag{4.25}$$

where the sums are over $n_p, n_q < 0$ such that $r_{n_pn_q} \le k_{max}$ and one of the four conditions $n \pm n_p \pm n_q = 0$ is satisfied. Note that the condition $n_p, n_q < 0$ is required for existence of the resonance curve at $k = 0$.

Symmetry considerations can be applied to (4.24) and (4.25). Antisymmetry of $\Lambda_{nn_pn_q}(p)$ with respect to $n_p \leftrightarrow n_q$ means that the $n_p = n_q$ contributions are zero. Symmetry of $r_{n_pn_q}$ and $\gamma_{n_pn_q}$ and antisymmetry of $\Lambda_{nn_pn_q}(p)$ with respect to $n_p \leftrightarrow n_q$ yield

$$J_n(0) = 2\pi \sum_{n_p,n_q} \frac{\Lambda_{nn_pn_q}(r_{n_pn_q})\left(\Xi_{nn_pn_q}(r_{n_pn_q})B_{|n_p|}(r_{n_pn_q}) - \Xi_{nn_qn_p}(r_{n_pn_q})B_{|n_q|}(r_{n_pn_q})\right)}{\gamma_{n_pn_q}(r_{n_pn_q})}, \tag{4.26}$$

$$\tau_n(0) = 4\pi \sum_{n_p,n_q} \frac{\Lambda^2_{nn_pn_q}(r_{n_pn_q})}{\gamma_{n_pn_q}(r_{n_pn_q})} B_{|n_p|}(r_{n_pn_q})B_{|n_q|}(r_{n_pn_q}), \tag{4.27}$$

where the sums are over $-n_{max} \le n_p < n_q < 0$ such that $r_{n_pn_q} \le k_{max}$ and one of the four conditions $n \pm n_p \pm n_q = 0$ is satisfied.

Evaluation of (4.26) and (4.27) requires the values $r_{n_pn_q}$, which are the solution of (3.27) with respect to $p > 0$. The left-hand side of (3.27) has the value -1 at $p = 0$. It is evaluated at consecutive integer values of p, starting at $p = 1$, until it becomes positive or zero. This provides an interval of length 1 in which the solution is to be found. Interval halving is then used to obtain p to a prescribed tolerance. The quantities $B_{|n_p|}(r_{n_pn_q})$ and $B_{|n_q|}(r_{n_pn_q})$ are obtained by linear interpolation between consecutive discrete wavenumbers.

4.4.4. Critical wavenumbers

Consider a critical wavenumber, k_c. For $k < k_c$, the corresponding resonance curve is absent and the limiting values, $J_n^<(k_c)$ and $\tau_n^<(k_c)$, as $k \nearrow k_c$ can be obtained using (4.16), (4.17) and numerical integration around the remaining resonance curves as described earlier. That is, the n_p, n_q associated with k_c are excluded from the sums in (4.17). However, the critical resonance curve contributes to $J_n^<(k_c)$ and $\tau_n^<(k_c)$, the limiting values as $k \searrow k_c$. The critical curve contributions can be obtained by considering the limit, in the manner described in section 3.3 and Appendix F. Thus we find

$$J_n^>(k_c) = J_n^<(k_c) + \frac{2\pi^2}{(\mu_1\mu_2)^{1/2}}\Big(\eta_{nn_pn_q}(\mathbf{k}_c, \mathbf{p}_c)B_{|n_p|}(p_c) + \eta_{nn_qn_p}(\mathbf{k}, -\mathbf{k}-\mathbf{p})B_{|n_q|}(|\mathbf{k}_c + \mathbf{p}_c|)\Big), \quad (4.28)$$

$$\tau_n^>(k_c) = \tau_n^<(k_c) + \frac{4\pi^2}{(\mu_1\mu_2)^{1/2}}\lambda_{nn_pn_q}(\mathbf{k}_c, \mathbf{p}_c)B_{|n_p|}(p_c)B_{|n_q|}(|\mathbf{k}_c + \mathbf{p}_c|). \quad (4.29)$$

Note that (4.28) and (4.29) include contributions from both members of the pair of critical points corresponding to k_c.

4.5. Time discretization and associated numerical scheme

Time is discretized to equally spaced values, T_m, with time step ΔT. (4.1) implies

$$B_n(T_{m+1}) = B_n(T_m)\,\mathrm{e}^{\theta_n(T_{m+1})} + \int_{T_m}^{T_{m+1}} \tau_n(T')\,\mathrm{e}^{\theta_n(T_{m+1})-\theta_n(T')}\,\mathrm{d}T', \quad (4.30)$$

where

$$\theta_n(T) = \int_{T_m}^{T} \alpha_n(T')\,\mathrm{d}T'. \quad (4.31)$$

A first approximation (predictor step) is obtained by taking constant $\alpha_n(T') = \alpha_n^*$, $\tau_n(T') = \tau_n^*$, where α_n^* and τ_n^* are computed using the known spectral values, $B_n(T_m)$, from the end of the previous time step. Thus, (4.30) and (4.31) give the first approximation

$$B_n^*(T_{m+1}) = B_n(T_m)\,\mathrm{e}^{\alpha_n^*\Delta T} + \Delta T\frac{\mathrm{e}^{\alpha_n^*\Delta T}-1}{\alpha_n^*\Delta T}\tau_n^*. \quad (4.32)$$

A second approximation (corrector step) follows from taking $\alpha_n(T') = \alpha_n^{**}$, $\tau_n(T') = \tau_n^{**}$, where α_n^{**} and τ_n^{**} are computed using the spectral values $(B_n(T_m) + B_n^*(T_{m+1}))/2$. Thus,

$$B_n(T_{m+1}) = B_n(T_m)\,\mathrm{e}^{\alpha_n^{**}\Delta T} + \Delta T\frac{\mathrm{e}^{\alpha_n^{**}\Delta T}-1}{\alpha_n^{**}\Delta T}\tau_n^{**} \quad (4.33)$$

completes the time step.

Since $\lambda_{nn_pn_q}(\mathbf{k},\mathbf{p})$, $\Gamma_{n_pn_q}(\mathbf{k},\mathbf{p})$ and the spectral values are positive, (4.4) implies that $\tau_n(k) \geq 0$. Having this in mind, one concludes from (4.32) and (4.33) that initially positive spectra cannot become negative, hence, the scheme does not spoil the realizability property mentioned in section 3.1. That is the advantage of this scheme, compared with, say, use of second-order Runge-Kutta.

To improve precision when $\alpha_n^*\Delta T$ is small, (4.32) is written as

$$B_n^*(T_{m+1}) = B_n(T_m) + \Delta T \frac{e^{\alpha_n^*\Delta T}-1}{\alpha_n^*\Delta T}(\tau_n^* + \alpha_n^* B_n(T_m)). \tag{4.34}$$

for (say) $\left|\alpha_n^*\Delta T\right| \leq 0.2$ and the quantity $\left(e^X-1\right)\Big/X$ is evaluated using a power series in $X = \alpha_n^*\Delta T$. The same method is employed for (4.33) when $\left|\alpha_n^*\Delta T\right| \leq 0.2$.

The above procedure is used for time stepping of all discrete wavenumbers. Critical wavenumbers use the scheme twice: once for $B_n^<$ and once for $B_n^>$.

4.6. Program description

In the current implementation there are eight numerical parameters. They are:

- n_{max} — maximum order of the inertial waveguide modes;
- k_{max} — maximum wavenumber value;
- N — number of k_i, given by (4.11), in the range $0 \leq k \leq k_{max}$;
- χ — parameter appearing in (4.11), of order Ξ;
- δ — parameter determining the step length, Δs, for integration over a resonance curve;
- ϵ — tolerance used for the interval halving (not to be confused with Rossby number, ε);
- T_{max} — maximum time;
- N_T — number of time steps, which with T_{max} define a time step $\Delta T = T_{max}/N_T$.

n_{max}, k_{max} and N should be sufficiently large and δ, ϵ and ΔT sufficiently small that the numerical results have satisfactorily converged. The three physical parameters are:

- β_v — the volume damping coefficient;
- β_w — the wall damping coefficient;

- Ξ — the initial spectral width.

We can divide the program into two stages — initialization and time evolution.

During the initialization stage all the required critical points are found using the method described in Appendix E in order to construct the discrete wavenumbers, $k_{i,n}$. Then, the points of intersection of the resonance curves with the p_1-axis, P^- and P^+, or radii $r_{n_p n_q}$, in the case $k = 0$, are determined. Finally, the spectra are initialized as described in section 4.1.

The evolution stage consists of a loop over time steps until the desired maximum time is reached. Each time step is divided into two stages, predictor and corrector. Both involve the calculation of J_n and τ_n as described in section 4.4.

4.7. Parallelization

The purpose of parallelization is to improve performance by carrying out similar calculations simultaneously. It is accomplished by dividing the problem into independent parts which are to be calculated by different processes. It is important to balance the amount of work across the processes for the sake of efficiency of the parallelization.

The most time-consuming part of the computations is the calculation of the integrals over the resonance curves. It is therefore natural to allocate a subset of resonance-curve integrals to each process. As the number of resonance curves differs with n and k, the idea is to distribute resonance curves across processes in such a way that the number of curves treated by each process is approximately the same. This allows us to calculate $J_n(k)$ and $\tau_n(k)$ independently on each process for its range of n, $k_{i,n}$. The results are then shared across all processes when applying the time-stepping scheme described in section 4.5.

4.7.1. Scalability

The fact that an algorithm can be subdivided into different tasks does not necessarily imply that parallelization will be effective. It is often the case that intercommunications consume a significant part of the computational capacity. In order to estimate the quality of a given implementation measures such as *speedup* and *efficiency* are widely employed. The former presents the ratio of the sequential-version runtime to the time taken by the parallel one. The latter quantifies the fraction of time for which a processor is usefully utilized. For sake of simplicity we compare the results of a one-process parallel version instead of the sequential one. Formally, relative speedup, S_p, and efficiency, E_p, for p processes are defined as follows

$$S_p = \frac{T_1}{T_p}, \tag{4.35}$$

$$E_p = \frac{S_p}{p} = \frac{T_1}{pT_p}, \tag{4.36}$$

where T_p denotes the computing time for p processes.

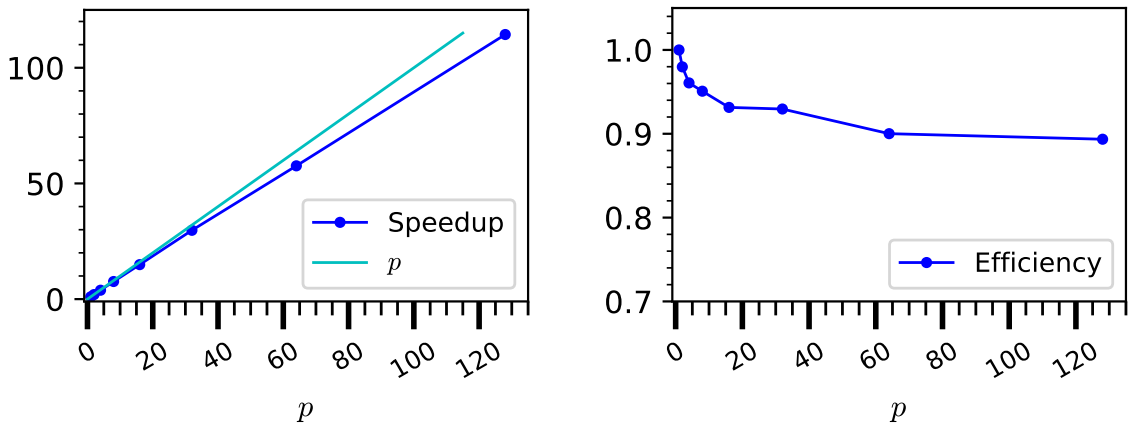

Figure 4.1.: Left: the relative speedup, the slope is 0.98; right: the relative efficiency.

Figure 4.1 illustrates the relative speedup and efficiency of our implementation. These results were obtained using the numerical parameters: $n_{max} = 10$, $k_{max} = 8000$, $N = 500$, $\epsilon = 10^{-13}$, $\delta = 0.01$, $N_T = 2000$ and $T_{max} = 0.2$. The calculations were carried out on the cluster P2CHPD (https://p2chpd.univ-lyon1.fr/) equipped with Intel(R) Xeon(R) E5-2670 2.60GHz processors. The typical calculation time on 128 cores is about 7 minutes. The above results show satisfactory efficiency of the parallelized implementation, at least in the case of exploitation up to 128 processes.

4.8. Validation

In order to verify the correctness of our implementation, we checked the accuracy of particular core functions and verified the properties of energy conservation and thermalization.

4.8.1. Tests of the core routines

To check correctness of the core routines of the WTC code we estimated their accuracy using a number of measures of numerical error:

- ERRC — critical point determination;
- ERRR — determination of the resonance-curve radius in the case $k = 0$;

- ERRP — P^- and P^+ determination;
- ERRRC — integration of (4.13);
- ERRD — calculation of the spectral time derivatives;
- ERRT — energy conservation by nonlinear transfers in the absence of viscosity.

The first three measures, ERRC, ERRR and ERRP, are respectively defined as the maximum deviation from zero of the left-hand sides of (3.29) and (3.30), (3.27) and (4.12). They are supposed to be controlled by the parameter of interval-halving tolerance, ϵ, which is confirmed by numerical results from Table 4.1.

ϵ	ERRC	ERRR	ERRP
10^{-13}	$1.6 \cdot 10^{-14}$	$5.1 \cdot 10^{-15}$	$8.4 \cdot 10^{-15}$
10^{-3}	$2.1 \cdot 10^{-4}$	$1.3 \cdot 10^{-4}$	$1.5 \cdot 10^{-4}$

Table 4.1.: Tolerance-dependent accuracy measures.

To examine the accuracy of the integration of (4.13), we calculate ERRRC as the maximum deviation from zero of the left-hand side of (4.12). As a fourth-order Runge-Kutta scheme is employed, it is expected to behave as $O(\Delta s^4)$, where Δs is a step length of the integration. Given that Δs is determined from δ using (4.15), we expect an error proportional to δ^4. Figure 4.2 demonstrates the expected slope. Thus, we conclude that marching over the resonance curve is properly implemented.

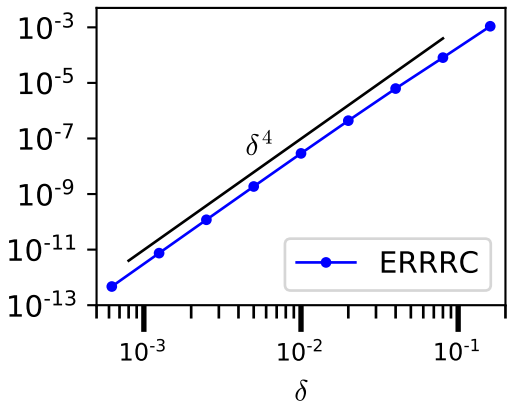

Figure 4.2.: ERRRC convergence, the slope is 3.95.

Consider the time derivative of spectra which is calculated using (4.1). To estimate the accuracy of the calculation, the integral involved in $J_n(k)$ and $\tau_n(k)$ are evaluated using a more

precise method, namely, fourth-order Runge-Kutta, and compared to the one used in the code, which employs a second-order trapezoidal-style rule. Note that the initial spectra, which have no discontinuous jumps and are smooth, were used. This is the reason why we expect a fourth-order integration to more accurate. However, once spectral jumps have developed under time evolution, the trapezoidal-style integration with spectral discretization which respects the critical wavenumbers is preferable, hence its use in the code we have developed. ERRD is obtained as the maximum difference between the second-order and fourth-order spectral time derivatives, divided by the maximum absolute value of those derivatives.

At first sight it is perhaps natural to expect ERRD to converge as $O(\Delta s^2)$, i.e. proportional to δ^2, because of the second-order integration scheme. However, as discussed in section 4.4, to evaluate the integrand in the middle of a subinterval, linear interpolation between spectral values at two consecutive points k is used. This means that, besides the integration error, there is another source of inaccuracy which is linear interpolation of the spectra. Hence, to make the overall error converge as second order, we should decrease the integration step length, Δs, and also increase the number of discrete wavenumbers, N, in proportion. Results showing the expected second-order accuracy are given in Figure 4.3.

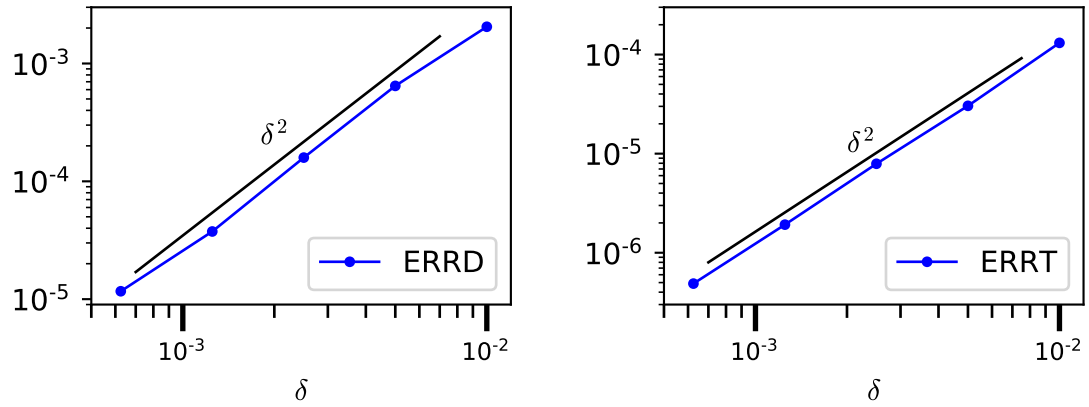

Figure 4.3.: Left: ERRD convergence, the slope is 1.95; right: ERRT convergence, the slope is 1.99. The value of $N = 7.8/\delta$.

The nonlinear transfer term on the right-hand side of (4.1) is

$$T_n(k) = J_n(k)B_n(k) + \tau_n(k). \tag{4.37}$$

Energy conservation means that the integral of $T_n(k)$ over $\mathbf{k}$, summed over $n > 0$, should be zero. The energy conservation error is defined as

$$ERRT = \frac{\sum_n \int T_n(k)k \, \mathrm{d}k}{\sum_n \int \left|T_n(k)\right|k \, \mathrm{d}k}. \tag{4.38}$$

If there was no discretization, ERRT would be zero. The numerical results, presented in the Figure 4.3, show the expected δ dependence when δ and N are varied, keeping δN constant.

Thus, we conclude that the implementation respects the expected energy conservation of the wave-component.

4.8.2. Accuracy following time evolution

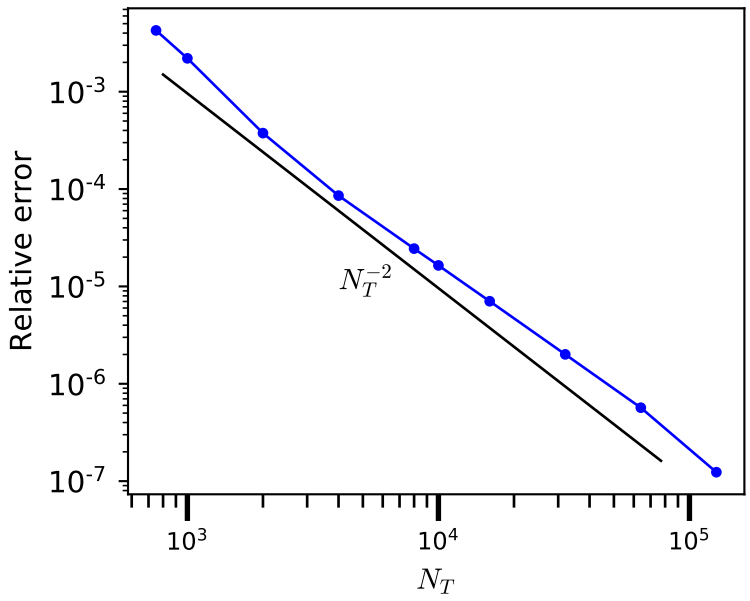

Figure 4.4.: Convergence as a function of N_T.

One can also ask how well the time-stepping scheme represents the time solution of the model. In reply to this question, we undertook a number of runs of the code with different N_T. The results at a given T_{max} were compared with a reference case for which N_T was so large that convergence was guaranteed. Without going into the precise details, Figure 4.4 shows the variation of the difference between the calculated and "true" spectra as a function of N_T. The straight line has a slope of -2, indicating that the time-stepping scheme has the expected second-order accuracy.

4.8.3. Thermalization

As shown in Appendix C, the inviscid wave-turbulence model, truncated to k_{max} and n_{max}, respects a state in which $B_n(k)$ is independent of k and n, a state known as *equipartition*. In classical statistical mechanics, such a state applies at thermodynamic equilibrium. It may be

interesting to see whether the model developed here approaches equipartition under time evolution.

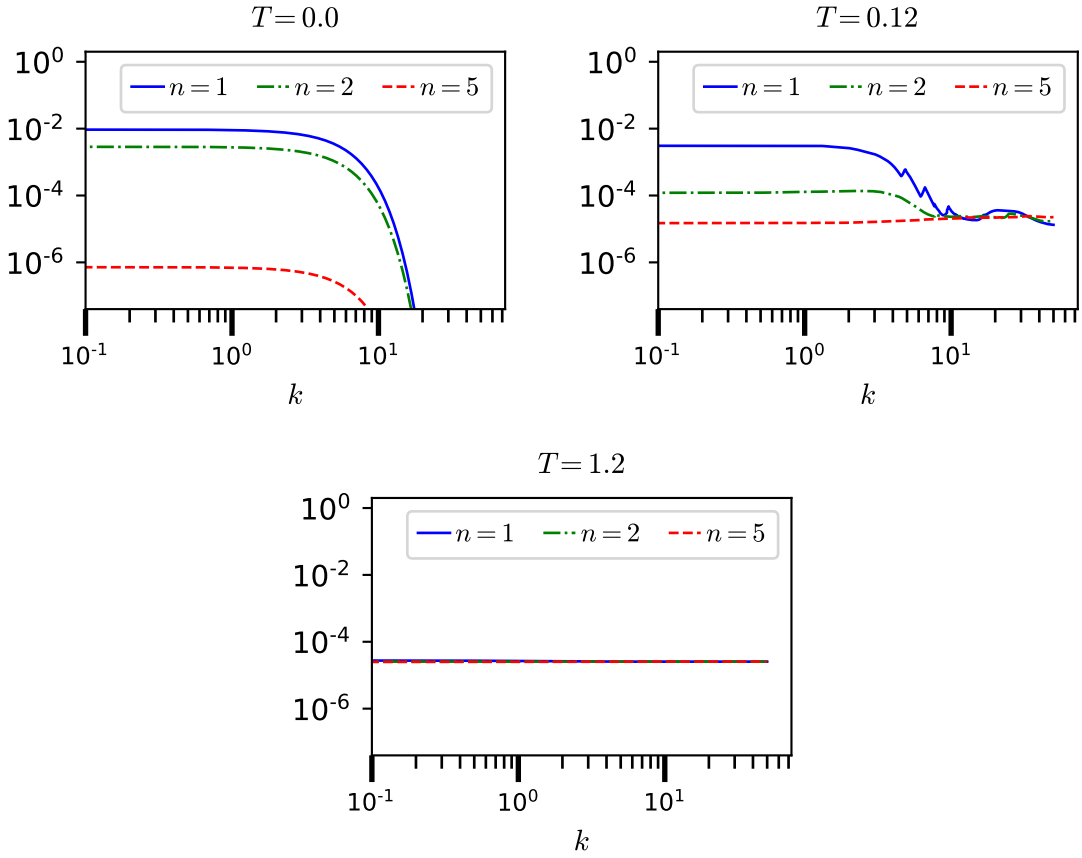

Figure 4.5.: Thermalization process.

In order to accelerate the process we truncated wavenumbers via a relatively small value of k_{max}. The parameters used are: $n_{max} = 5$, $k_{max} = 50$, $N = 500$, $\epsilon = 10^{-13}$, $\delta = 0.01$, $N_T = 20000$, $T_{max} = 2$, $\Xi = 5$, $\beta_v = 0$ and $\beta_w = 0$. Figure 4.5 shows the evolution of energy density, $B_n(k)$, for modes $n = 1$, $n = 2$ and $n = 5$. Energy is first transferred to the small scales, reaching the cut-off, then propagates backwards to the larger scales, eventually leading to equipartition of the energy. Note that the final value is the same for all the waveguide modes. The fact that the numerical scheme is able to capture this pile-up of energy in the small scales without blowing up is a good indicator of its robustness. Needless to say, equipartition is an artefact of truncation and does not occur in the untruncated problem.

5. WTC numerical results

This chapter presents numerical results obtained using the wave-turbulence closure. We first describe the overall energetics in section section 5.1. In the second part of this chapter, section 5.2 gives a more detailed analysis in which the distribution of energy over k and n is discussed.

5.1. Energy evolution

Because wave-turbulence theory limits us to work only with wave component, i. e. modes $n \neq 0$, energy refers only to wave-component part. According to $B_n(k) = \varepsilon^{-2} A_{nn}$, $A_{-n-n} = A_{nn}$ and (3.19) we can write the total energy as

$$\frac{1}{2}\int_0^1 \overline{u_i u_i}\, \mathrm{d}x_3 = \underbrace{\int_0^\infty \pi\varepsilon^2 B_0(k) k\, \mathrm{d}k}_{\text{2D part}} + \underbrace{\varepsilon^2 \mathscr{E}}_{\text{wave-component part}}, \tag{5.1}$$

where

$$\mathscr{E} = 2\pi \sum_{n=1}^{\infty} \int_0^\infty B_n(k) k\, \mathrm{d}k \tag{5.2}$$

represents the wave-component part of the energy.

An evolution equation for $\mathscr{E}(T)$ can be obtained by multiplying equation (4.1) by $2\pi k$, integrating over k and summing over $n \geq 1$. As discussed earlier, the nonlinear term, $J_n B_n + \tau_n$, represents energy transfer between modes and is energy conserving. Thus, it contributes zero, hence

$$\frac{\mathrm{d}\mathscr{E}}{\mathrm{d}T} = -D_v - D_w, \tag{5.3}$$

where

$$D_v = 2\pi\beta_v \sum_{n=1}^{\infty} \int_0^\infty \left(k^2 + n^2\pi^2\right) B_n(k) k\, \mathrm{d}k, \tag{5.4}$$

$$D_w = \sqrt{2}\pi\beta_w \sum_{n=1}^{\infty} \int_0^\infty \left(1 - \omega_n^2(k)\right)^{1/2} \left(\left(1 + \omega_n(k)\right)^{3/2} + \left(1 - \omega_n(k)\right)^{3/2}\right) B_n(k) k\, \mathrm{d}k \tag{5.5}$$

and we have used equation (4.5). Both D_v and D_w are positive and represent two contributions to viscous dissipation, namely volumetric and wall damping. The energy decreases monotonically according to (5.3). Although (5.3) does not directly involve the nonlinear transfer term, as we shall see later, the latter has a profound effect on spectral evolution, producing an energy cascade towards the small scales. The factor $k^2 + n^2\pi^2$ in (5.4) is larger for such scales, so nonlinear transfer tends to accentuate the volumetric dissipation. In any case, the time evolution of the spectrum, $B_n(k)$ in (5.4) and (5.5), due to such transfer has important consequences for D_v and D_w and there is thus an indirect effect of nonlinearity on the energy dissipation.

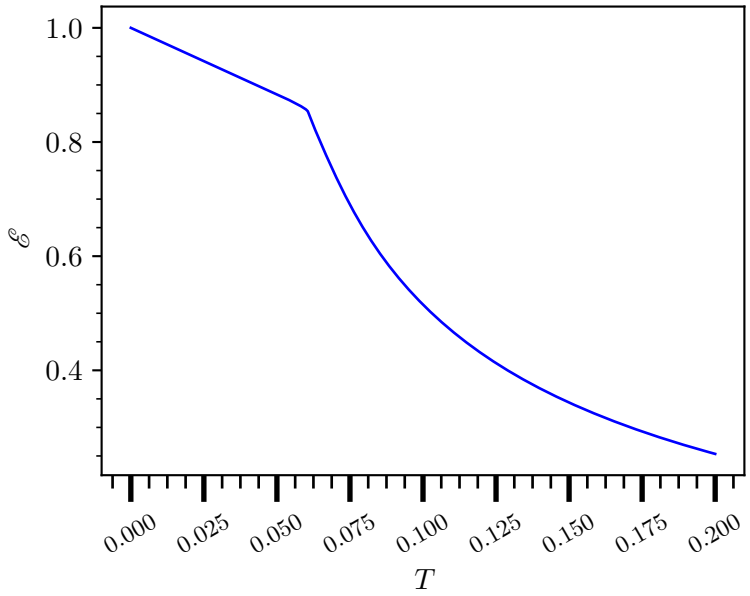

Figure 5.1.: Evolution of energy; $\Xi = 5, \beta_w = 2$ and $\beta_v = 0.002$.

Figure 5.1 and Figure 5.2 show results for the time evolution of $\mathscr{E}$, D_v and D_w for a particular choice of parameters. As will be seen, there are two phases of energy evolution. $\mathscr{E}$ initially decreases rather slowly, following an approximately linear time-dependency. There is then a quite abrupt transition to more rapid decay. The reason for this behavior can be seen from Figure 5.2. During the initial phase, wall damping is dominant and D_w is approximately constant. However, volumetric damping increases rapidly as a certain time, referred to as the critical time T_c, is approached and it takes over from wall damping as the dominant dissipative mechanism. Nonlinear transfer to smaller scales is responsible for the rapid rise in D_v near the critical time, where a dissipative range of wavenumbers is established.

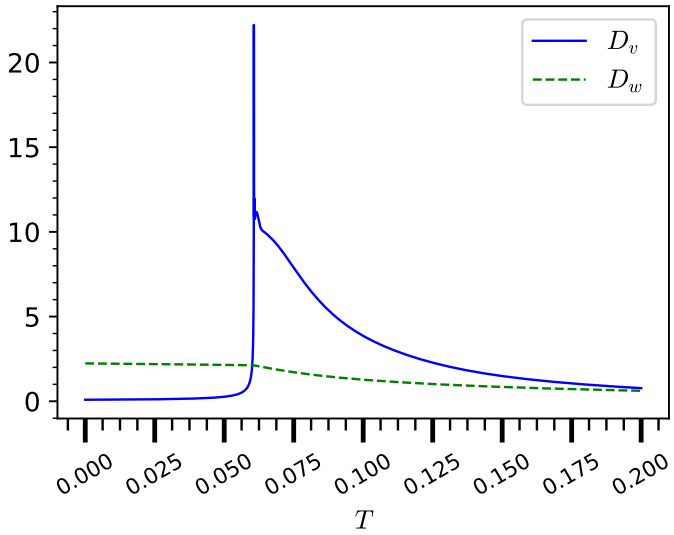

Figure 5.2.: Evolution of viscous-damping contributions to the energy dissipation; $\Xi = 5$, $\beta_w = 2$ and $\beta_v = 0.002$.

5.1.1. Volumetric damping

The above results are for the case $\beta_v = 0.002$ of a relatively small volumetric damping coefficient. Figure 5.3 shows the effects of increasing β_v. The transition between the two phases of evolution is less and less rapid and takes place at longer times. The latter conclusion may, at first sight, be surprising because one expects the dissipative range to shift to lower wavenumbers. Hence, less time to establish the dissipative range. However, the energy at a given time is reduced by the increased dissipation, which decreases the turbulence intensity. Thus, the nonlinear transfer terms are reduced, leading to slower transfer. And it is the latter effect that wins.

Figure 5.4 shows the volumetric dissipation using the same parameters Figure 5.3. The decreasing sharpness of the peak with increasing β_v corresponds to the less rapid transition between the two phases of evolution noted above. Given the difficulty of visually identifying a critical time for the larger values of β_v, we decided to define it more precisely by the maximum of D_v.

Table 5.1 shows the value of $T_c \cdot \mathscr{E}(T_c)$ for different β_v, $\Xi = 5$ and $\beta_w = 1$. It is seen that the value is very nearly constant, and thus despite significant increases in T_c for the larger β_v in the table (recall Figure 5.4). This supports the suggestion, made earlier, that the observed increase of T_c with β_v is due to slower nonlinear transfer because the higher dissipation has made the turbulence less intense. $\mathscr{E}(T_c)$ is a measure of turbulence intensity and constant $T_c \cdot \mathscr{E}(T_c)$ suggests that the time taken for transfer is inversely proportional to the energy, not an implausible suggestion given that the nonlinear term in the spectral equations is quadratic.

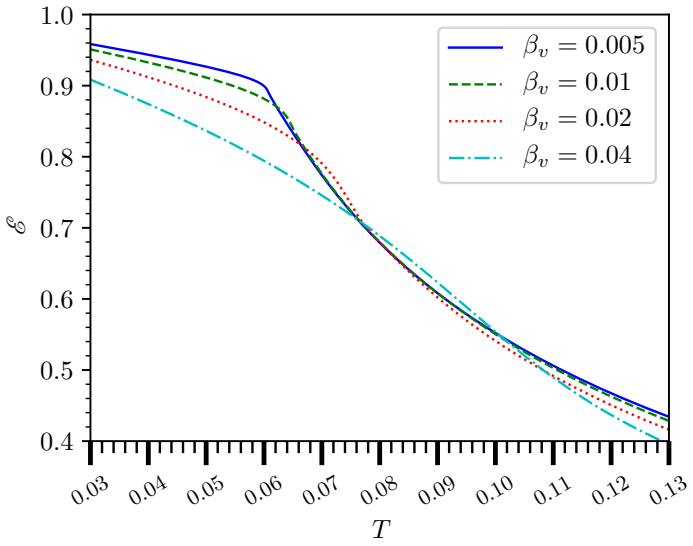

Figure 5.3.: Changes of the energy-evolution plot when varying β_v; $\Xi = 5$ and $\beta_w = 1$.

β_v	T_c	$T_c \cdot \mathscr{E}(T_c)$
0.005	0.061	0.0541
0.01	0.065	0.0546
0.02	0.075	0.0551
0.04	0.096	0.0558

Table 5.1.: $T_c \cdot \mathscr{E}(T_c)$ for different β_v; $\Xi = 5$ and $\beta_w = 1$.

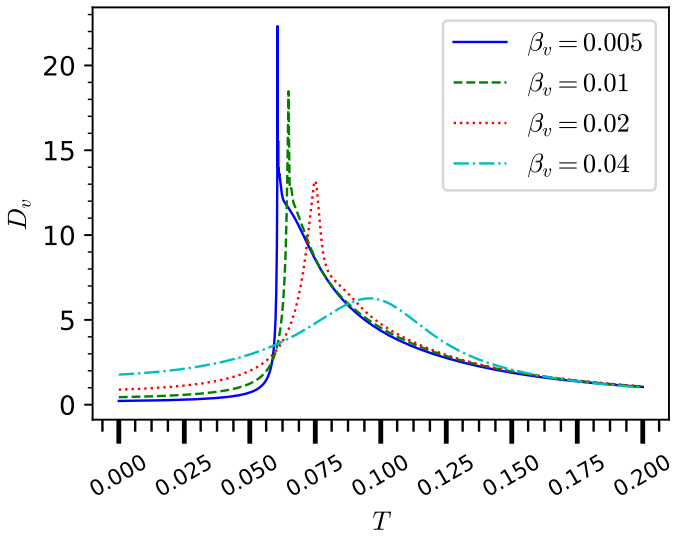

Figure 5.4.: Evolution of the volumetric-damping rate; $\Xi = 5$ and $\beta_w = 1$.

5.1.2. Wall damping

Figure 5.5 shows the effects of varying β_w on the time evolution of energy for a given (small) β_v. As β_w increases the energy decays more rapidly in the initial phase. The limiting case $\beta_w = 0$ shows that there is still some decay prior to the critical time, even though only the volumetric contribution to energy dissipation is present. Following the critical time, the energy decay is not greatly affected by β_w.

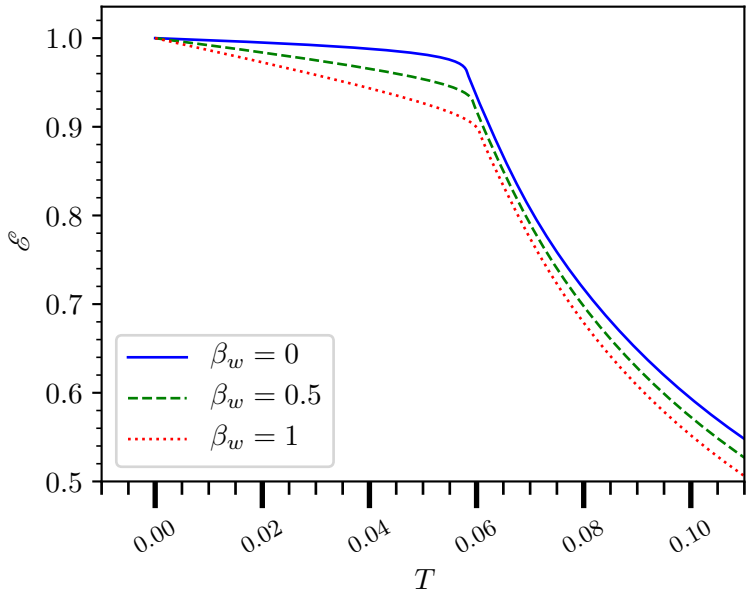

Figure 5.5.: Evolution of energy; $\Xi = 5, \beta_v = 0.005$.

The critical time itself is shown as a function of β_w for two values of β_v in Figure 5.6. Apparently it does not depend strongly on either β_w or β_v *provided* β_v *is small enough*. It is found to be an increasing function of either of the dissipation coefficients.

Figure 5.7 shows the evolution of D_v and D_w as log-log plots. The straight lines following the critical time suggest power laws. The slopes of the lines imply exponents of -1 for $\mathscr{E}$, -1.02 for D_w and -2.37 for D_v. Note that the exponents of $\mathscr{E}$ and D_w are very nearly the same, whereas D_v decays more rapidly. The factor multiplying $B_n(k)k$ in the integral of (5.5) is $O(1)$ for all modes and does not weight small scales more than large ones. Thus, like the energy, D_w is dominated by the large scales and it is perhaps not surprising that $\mathscr{E}$ and D_w evolve in a similar way. Indeed if, as a might approximation, the given factor is replaced by 1, the integrals in (5.2) and (5.5) are the same. On the other hand, the factor $k^2 + n^2\pi^2$ in (5.4) weights the small scales more than the large ones and D_v is dominated by the former. It is thus to be expected to show different behavior.

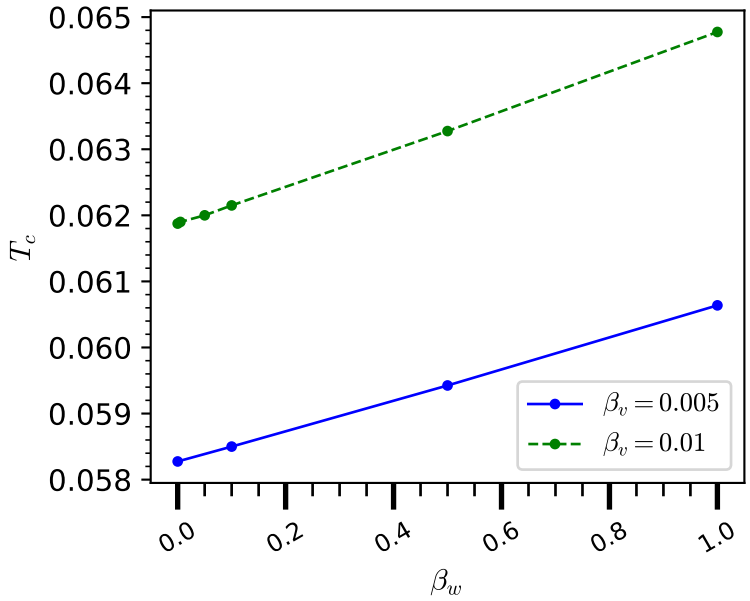

Figure 5.6.: T_c as a function of β_w; $\Xi = 5$ and $\beta_v = 0.01, 0.005$.

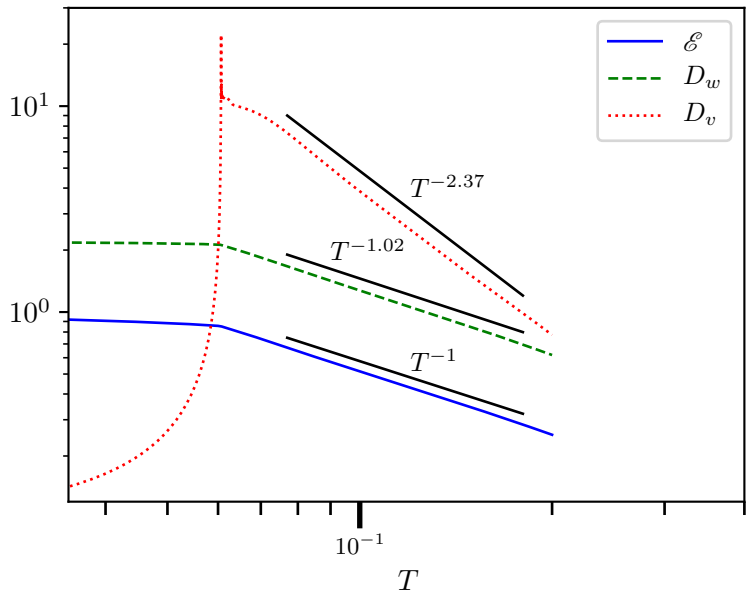

Figure 5.7.: Evolution of $\mathscr{E}$, D_v and D_w using a logarithmic scale; $\Xi = 5, \beta_w = 2$ and $\beta_v = 0.002$.

5.1.3. Influence of spectral width on the critical time

Having studied the effects of varying β_v and β_w for a single value, $\Xi = 5$, of the spectral width, one can ask the question: how do the results depend on Ξ? Figure 5.8 shows the critical time using a log-log plot as a function of Ξ. It will be seen that T_c decreases with increasing Ξ, presumably because increasing the energy of the smaller scales of the initial flow accelerates the nonlinear transfer. A power law of exponent about -2.4 is found at larger Ξ, and another of exponent about -0.4 at lower values of Ξ.

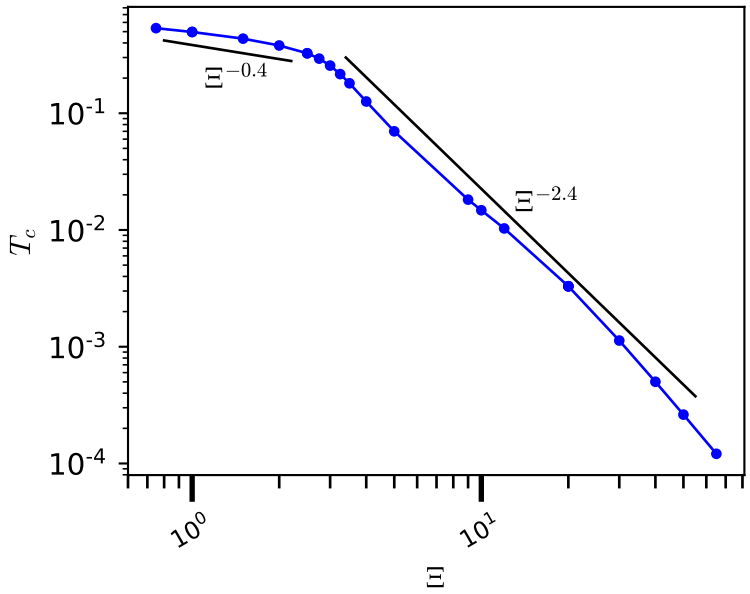

Figure 5.8.: Influence of spectral width on the critical time; $\beta_w = 1, \beta_v = 0.01$.

5.2. Spectral evolution

Initialized using (4.7), the spectra, $B_n(k)$, evolve according to the governing equations, (4.1). This evolution is the subject of this section. As for the energy, two phases of evolution are found. Firstly a spectral front propagates towards large k, forming an inertial range behind it. This illustrates the turbulent energy cascade. Then, near the critical time, the spectral advance ceases and a dissipative range is established. In the second phase the spectra decay and the dissipative range retreats to smaller k. As expected, spectral discontinuities are found in the inertial range. We also observe oscillations of the spectra which appear just prior to the critical time and persist thereafter.

5.2.1. The evolution of the $B_n(k)$

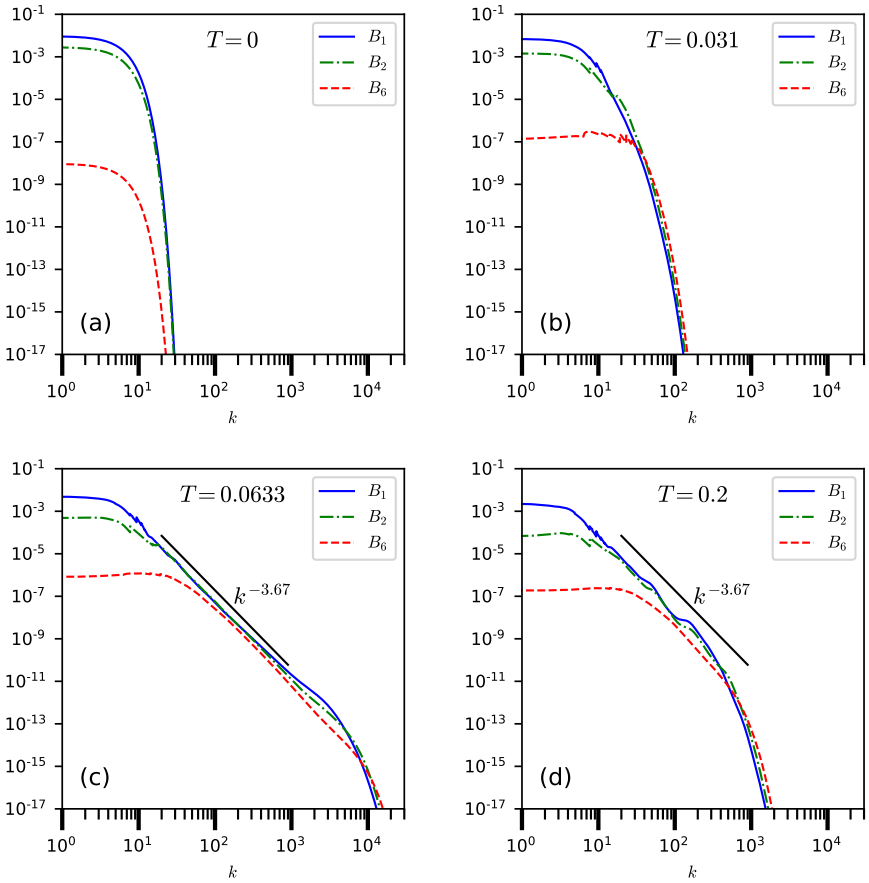

Figure 5.9.: Evolution of $B_n(k)$ for $n = 1, n = 2, n = 6$; $\Xi = 5, \beta_w = 2, \beta_v = 0.005$. The spectral front moves to the right in (a), (b), (c) and retreats back in (c), (d). The straight lines in (c) and (d) represent the power law $k^{-3.67}$.

Figure 5.9 shows results for $n = 1, 2$ and 6 for a particular choice of the parameters Ξ, β_w and β_v. As noted above, there are two phases: first a spectral front moves towards larger k. This reflects nonlinear transfer between modes and forms an inertial range behind the front. This phase lasts until volumetric dissipation becomes important and a dissipative range is established, dissipation balancing the nonlinear transfer at larger times. In the second phase, which begins at the critical time $T_c = 0.0633$, the front, now representing the dissipative range, retreats and the spectra decay. There is also nonlinear transfer between different n. This is apparent in the results for $n = 6$, which show increasing B_6 prior to the critical time, followed by decay thereafter. This transfer appears to go from smaller to larger n, as we might expect given a cascade from large to small scales. The spectra in the inertial range roughly follow straight

lines in these log-log plots, indicating power-law dependency of $B_n(k)$ on k. However, the existence of spectral discontinuities means such power laws are only approximate.

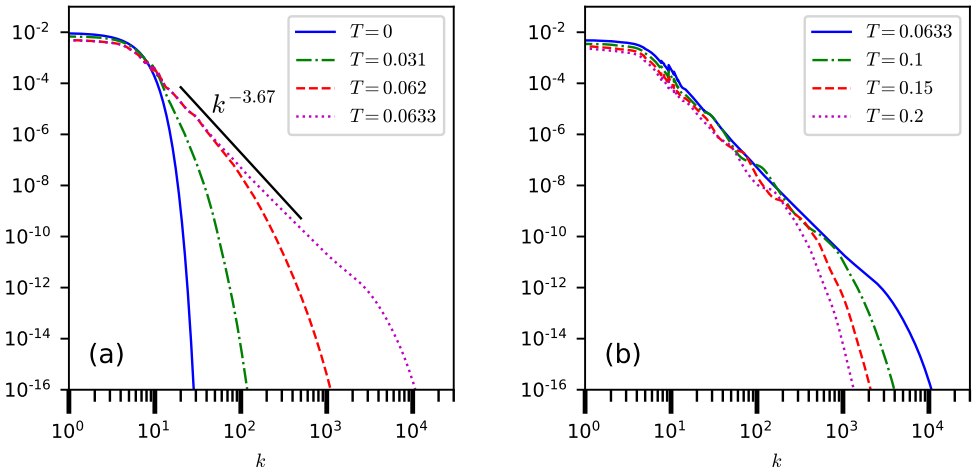

Figure 5.10.: Evolution of $B_1(k)$; $\Xi = 5, \beta_w = 2, \beta_v = 0.005$. The straight line shows the power law $k^{-3.67}$.

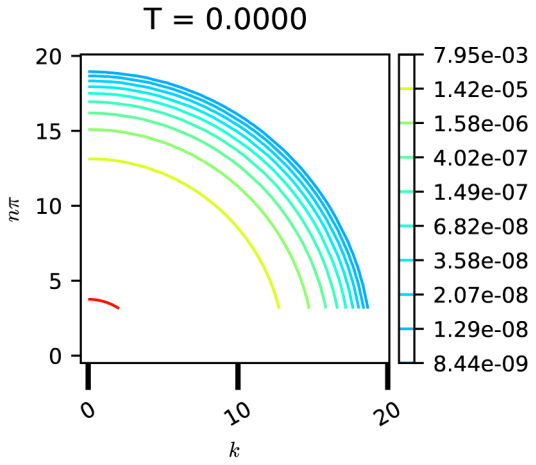

Figure 5.11.: Contours of $B_n(k)$ for $T = 0$; $\Xi = 5$.

Focusing on $n = 1$, Figure 5.10 shows $B_1(k)$ for more time instants than the previous figure. It is apparent that the front accelerates in the first phase of evolution, its rate of advance becoming very large as the critical time is approached. This rapid advance of the front is the reason for the sharp onset of volumetric dissipation at small β_v found in the previous section. It also requires a small time step to avoid numerical instability. As β_v is decreased, the dissipative range moves to larger k and a smaller time step is needed. Thus, we cannot simply set $\beta_v = 0$, but one might

speculate that the spectral front goes to infinite k in a finite time in the absence of volumetric damping. This would explain the insensitivity of T_c to variation of β_v at small enough values.

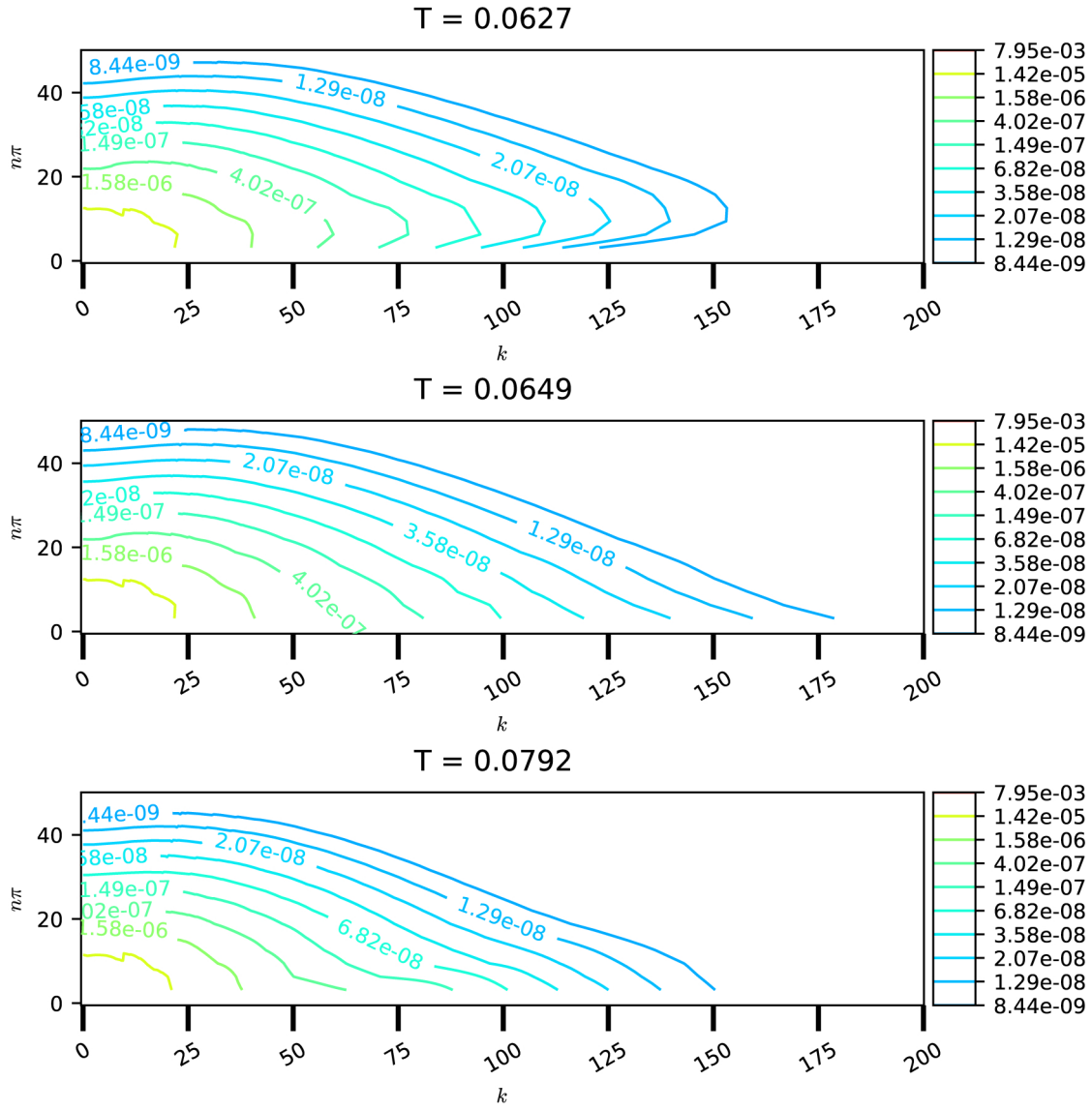

Figure 5.12.: Contours of $B_n(k)$ for time moments around $T = T_c = 0.0649$; $\Xi = 5$, $\beta_w = 1$, $\beta_v = 0.01$. Note the change of scales relatively to Figure 5.11, which is indicative of the transfer of energy to the smaller scales resulting from the energy cascade.

Figure 5.11 and Figure 5.12 show contours of $B_n(k)$ in the $(k, n\pi)$ plane at the initial instant and close to the critical time. The circular contours in Figure 5.11 are a reflection of the isotropic nature of the initial spectra. The transfer of energy to smaller scales due to the energy

cascade is reflected in Figure 5.12. The greater spectral extent in k than in $n\pi$ indicates more efficient transfer in the directions parallel to the walls. It is also apparent that, following the critical time, for given k, $B_n(k)$ is largest for smaller $n\pi$, having a maximum at $n = 1$. This is not true just prior to the critical time.

Figure 5.13 illustrates the existence of discontinuities in the spectra. The initial spectra are smooth, but time evolution according to the wave-turbulence closure causes discontinuities to appear.

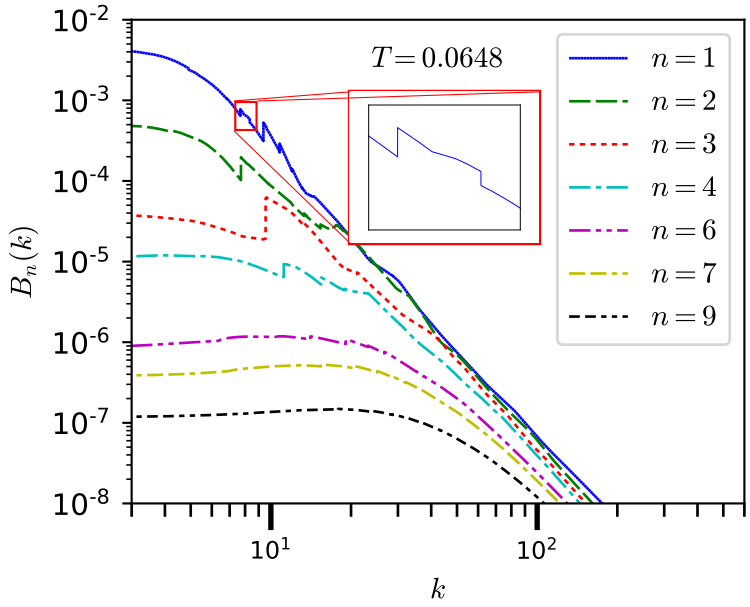

Figure 5.13.: Spectral discontinuities for different n at $T = T_c$; $\Xi = 5, \beta_w = 1, \beta_v = 0.01$.

5.2.2. Energy distributions in k and n

The energy, given by (5.2), can be decomposed in two ways:

$$\mathscr{E} = \int_0^\infty e(k)\ \mathrm{d}k \tag{5.6}$$

$$= \sum_{n=1}^{\infty} e_n, \tag{5.7}$$

where

$$e(k) = 2\pi k \sum_{n=1}^{\infty} B_n(k) \tag{5.8}$$

and

$$e_n = 2\pi \int_0^\infty kB_n(k)\ \mathrm{d}k. \tag{5.9}$$

Thus, $e(k)$ gives the energy distribution as a function of k, taking into account all n, where as e_n gives a similar description of the distribution of energy over n. Both are shown in Figure 5.14 for $\Xi = 5$, $\beta_w = 2$ and $\beta_v = 0.005$ and three values of T, including T_c. These results illustrate the advance, then retreat, of a spectral front in both k and n. The also indicate an inertial range in k and n to which power laws apply, but with somewhat different exponents for k and n.

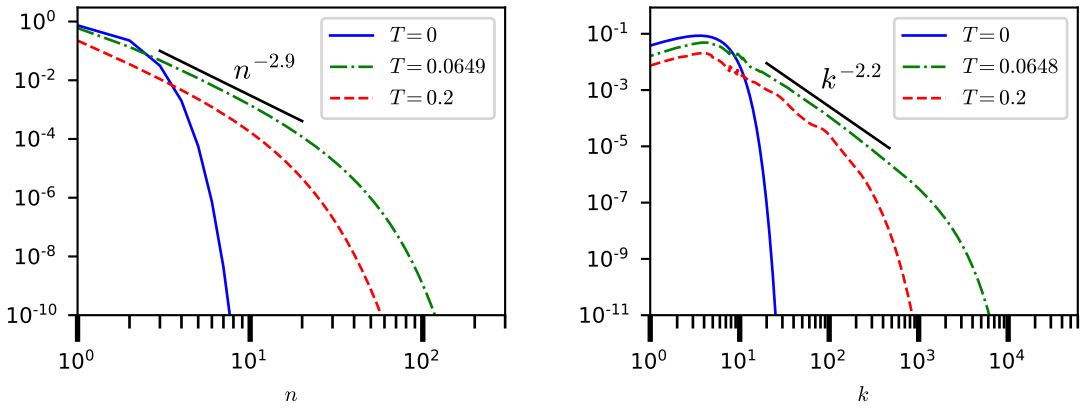

Figure 5.14.: e_n and $e(k)$; $\Xi = 5, \beta_w = 2, \beta_v = 0.005$.

The effects of varying β_w and β_v on $e(k)$ at the critical time are illustrated in Figure 5.15. Although increasing β_w diminishes the energy, because more has been dissipated, this is not as

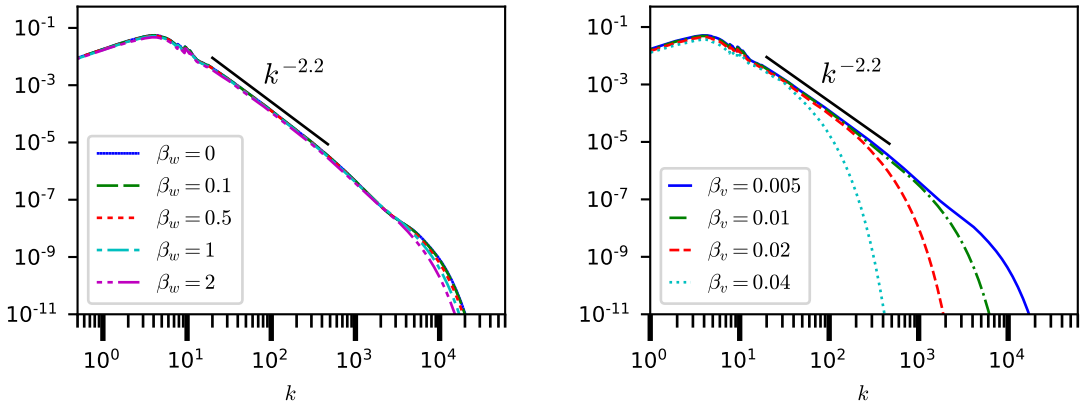

Figure 5.15.: $e(k)$ at $T = T_c$ for different β_w and β_v; $\Xi = 5$. Left: $\beta_v = 0.005$. Right: $\beta_w = 1$.

significant as the rapidly increasing dissipative wavenumber resulting from decreasing β_v. The log-log slope in the inertial range appears to be insensitive to both parameters.

5.2.3. Influence of the initial spectral width

As we saw in section subsection 5.1.3, varying Ξ changes the critical time significantly: the larger Ξ the more energy is initially present in the small scales and the more rapid the spectral evolution. Figure 5.16 shows $e(k)$ at the critical time for $\beta_w = 1, \beta_v = 0.01$ and various values of Ξ. The spectral slope of the inertial range appears not to vary with Ξ. Given its insensibility

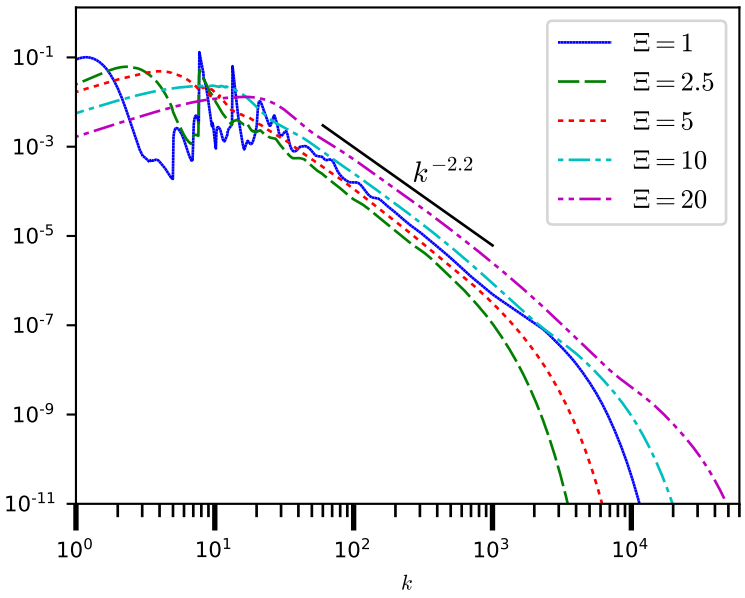

Figure 5.16.: $e(k)$ at $T = T_c$ for different values of Ξ; $\beta_w = 1, \beta_v = 0.01$.

to changes in β_w and β_v noted earlier, the slope seems to have a nearly constant value.

The figure also reveals a striking effect of varying Ξ on the spectral discontinuities, which become stronger when Ξ is decreased. As noted above, decreasing Ξ increases the critical time, reflecting slower spectral evolution. It may be that the longer development time encourages the appearance of discontinuities in the spectrum.

Figure 5.17 focusses on a single modal order, $n = 1$. It again shows that decreasing Ξ strengthens the discontinuities.

5.2.4. Spectral oscillations

Figure 5.10 shows that the spectral slope of $B_1(k)$ is close to -3.67, at least for the particular parameters used. Figure 5.18 shows $B_1(k)$, normalised by $k^{-3.67}$ at various times before, close to and after the critical time. Wavelike oscillations in both k and time appear near the critical time and persist thereafter.

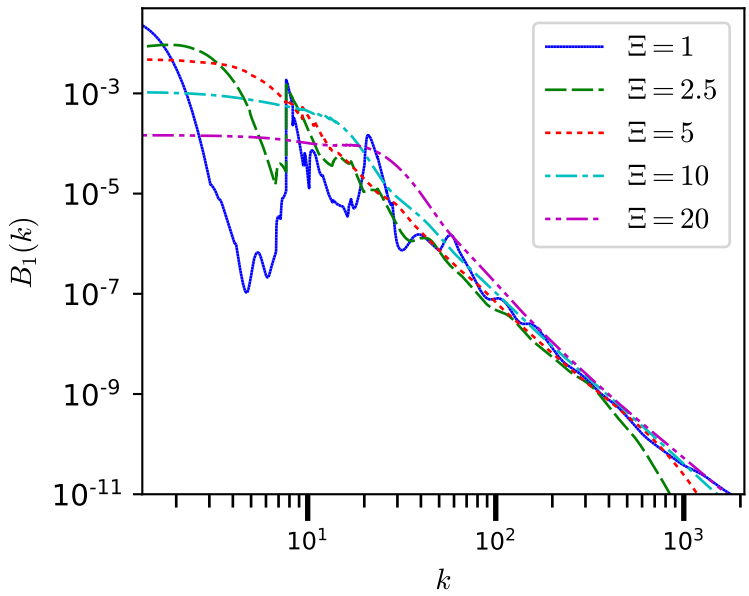

Figure 5.17.: Influence of initial spectral width, Ξ, on spectral discontinuities of $B_1(k)$ at $T = T_c; \beta_w = 1, \beta_v = 0.01$.

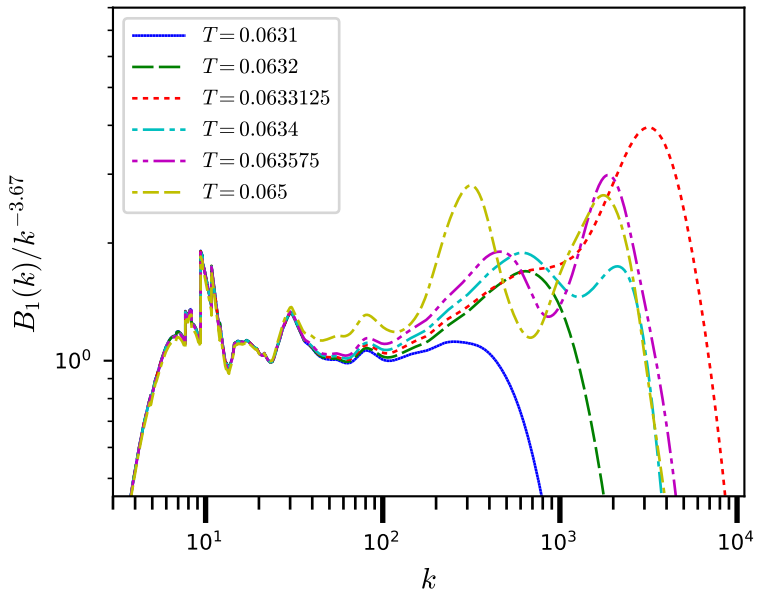

Figure 5.18.: Oscillations of the spectrum in the inertial range; $\Xi = 5, \beta_w = 2$ and $\beta_v = 0.005$. The spectrum is normalised with $k^{-3.67}$.

5.3. Conclusion

In section 5.1, we studied the time evolution of the wave-component energy, $\mathscr{E}$, which decays due to viscosity according to two mechanisms: wall dissipation, D_w, in the boundary layers and volumetric dissipation, D_v, throughout the flow. Wall and volumetric dissipations are characterised by two parameters, β_w and β_v, of the model, while the initial conditions introduce one more, the spectral width Ξ.

The results indicate two phases of evolution, clearly separated by a critical time T_c for small enough β_v. In the first phase, D_w is dominant, while D_v dominates in the second phase. The transition between phases becomes more and more abrupt as β_v is decreased. Prior to the critical time, wall damping causes the energy to decay at a rate dependent on β_w: the larger its value, the faster the decay. Following the critical time, volumetric damping takes over and power-law dependency on time is observed. The critical time is insensitive to β_w and β_v for small enough β_v, but depends strongly on Ξ. The larger the initial spectral width, the smaller T_c.

Section 5.2 presented results for $B_n(k)$, which describe the energy distribution over different modes, as well as $e(k)$, which includes all modal orders n for a given k, and e_n, which takes all k into account for a given n. Prior to the critical time, plots of $B_n(k)$ as a function of k show a spectral front which propagates towards larger k. This is symptomatic of an energy cascade from large to small scales. An inertial range is left behind by the advancing front. In this range the spectra have approximate power-law dependency on k. We say approximate because discontinuities appear in the spectra. The spectral front accelerates, moving very rapidly as the critical time is approached, which is why the transition to the second phase of evolution is so abrupt. Near the critical time volumetric dissipation becomes important and a dissipative range is formed in which volumetric dissipation balances energy transfer from larger scales. The front can subsequently be identified with the dissipative range and gradually retreats to smaller k as the turbulence decays in the second phase of evolution. Similar conclusions are reached when examining the evolution of $e(k)$, whose spectral slope in the inertial range, near to -2.2, at the critical time appears insensitive to the parameters Ξ, β_w and β_v.

The energy cascade prior to T_c also takes place in n. This is apparent in the energy distribution, $B_n(k)$, in the $(k, n\pi)$ plane and also as an advancing spectral front of e_n, plotted as a function of n. Thus, the cascade to smaller scales takes place in both wall-parallel and wall-normal directions. Higher values of the maximum front location, which occurs at the critical time, are reached for k than for $n\pi$, which suggests that transfer in k is more effective than in n.

A striking effect of varying Ξ is that the spectral discontinuities become more apparent at lower Ξ.

Finally, near the critical time, wavelike oscillations appear in the spectra. These oscillations take place in both k and T.

6. DNS

In this chapter, the generation of an initial velocity field consistent with the initial wave-turbulence spectrum is described. The resolution of the full Navier-Stokes equations is performed for a single set of physical parameters by direct numerical simulation. The choice of the physical and numerical parameters are discussed as well as the evaluation of the statistics (kinetic energy, matrix correlation spectrum, etc.). Results obtained are described at the end of this chapter.

6.1. Numerical method

The direct numerical simulations were done with the `NadiaSpectral` code, developed in our research group [6]. It solves the incompressible Navier-Stokes equations between two parallel walls with a spectral method based on a Galerkin approximation of the velocity fields using Fourier expansions in both directions parallel to the walls and Chebyshev polynomials in the wall-normal direction. Incompressibility is ensured by working in an inherently divergence-free basis set for the velocity, eliminating the pressure from the discrete solver [23]. The time is discretized to equally spaced values and solved with a third-order Runge-Kutta scheme [28]. Performance in massive multi-cores platforms has been obtained with a hybrid MPI/OpenMP parallelization [21] and the wall-time spent per time step has been measured as 1.3s for a configuration of one billion modes on 8192 MPI processes of a BlueGene/Q. The solver is written in C++ whereas python is used to embed analysis (initialization, I/O and calculation of statistics, etc.) in the simulation, asynchronously to the solver [7]. This technique was used to initialize the turbulence and to calculate the annular spectra during the simulation.

6.2. Choice of physical and numerical parameters

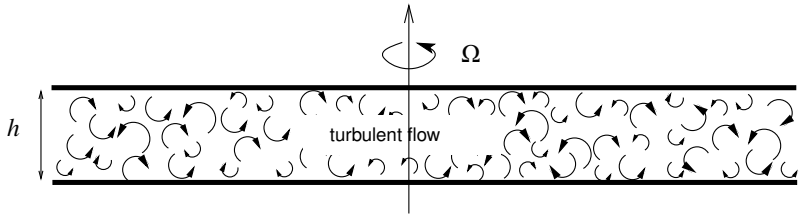

The physical geometry extends over the domain $L_1 \times L_2 \times h$ in x_1, x_2, x_3, where h is the channel width. Given the non-dimensionalization of earlier chapters, $h = 1$, so the turbulence occupies $0 < x_3 < 1$. Here $L_1 = L_2 \equiv L$ is the Fourier spatial period of the DNS. The wave-turbulence regime requires small Rossby number ε, which corresponds to high rotating speed of the walls, and small Ekman numbers E, to minimize the effect of the viscous force compared to the Coriolis force. The choice of L and of the numerical resolution are actually a compromise between several physical requirements and computational feasibility. The choice that has been made in this study is explained in the remainder of this section. Note that, although the choice is first described for the physical, then for the numerical parameters, in fact the two choices interact with each other, as will appear in what follows, so the final choice is obtained by iteration.

6.2.1. Physical parameters

The subject of this sub-section is the choice of the volumetric- and wall-damping parameters (resp. β_v and β_w) of the wave-turbulence model and its consequences for DNS. From the WTC analysis, the spectral width is chosen as $\Xi = 4$ to have distinguishable, but not dominant, spectral discontinuities. β_v and β_w are defined by

$$\beta_v = 2\varepsilon^{-2}\,\mathrm{E} \qquad \text{and} \qquad \beta_w = 2\varepsilon^{-2}\,\mathrm{E}^{1/2}$$

and $T = \varepsilon^2 t$ is the time variable of the wave-turbulence model. It should also be recalled that the time variable t is non-dimensionalized using the time scale $(2\Omega)^{-1}$ and that the highest frequency modal oscillation ($k = 0$), has period 2π with respect to t. The Ekman and Rossby numbers follow from the choice of β_v and β_w as

$$\varepsilon^2 = \frac{2\beta_v}{\beta_w^2} \qquad \text{and} \qquad \mathrm{E}^{1/2} = \frac{\beta_v}{\beta_w}.$$

The thickness of the Ekman layers is of order $\mathrm{E}^{1/2}$ [27], which should be small. Thus, $\beta_v/\beta_w \ll 1$ is a requirement of the WTC theory as already discussed in the chapter 4.

Another requirement is that there be many modal oscillations before nonlinearity becomes important. Let T_c be the critical time, taken as a measure of the time for significant nonlinearity. The corresponding $t_c = \varepsilon^{-2} T_c$ should be much larger than 2π. From a numerical point of view, too large a value of t_c would unnecessarily increase the calculation time, which we already expected to be at the limits of feasibility. We chose $t_c \approx 60$, corresponding to about 10 periods of the fastest oscillating mode.

A parametric study in which β_v and β_w were varied was carried out using the results of wave-turbulence theory to determine T_c and the location of the dissipative range. Given $t_c \approx 60$, there are two conflicting requirements: a) because the dissipative range wavenumber increases

rapidly as β_v is decreased, β_v should not be too small, otherwise the required number of DNS Fourier modes becomes excessive, and b) β_w should not be so large that wall damping kills the turbulence before nonlinearity has had a chance to express itself. The values $\beta_v = 0.019$ and $\beta_w = 3.4$ were judged to be satisfactory. These values correspond to $\varepsilon = 0.0573$ and $\mathrm{E} = 3.12 \cdot 10^{-5}$. The corresponding Ekman-layer thickness is $\mathrm{E}^{1/2} = 5.58 \cdot 10^{-3}$.

In summary, the chosen physical parameters are $\varepsilon = 0.0573$, $\mathrm{E} = 3.12 \cdot 10^{-5}$ and $\Xi = 4$. According to the wave-turbulence model the critical time occurs at $t_c = 60$.

6.2.2. Computational domain and numerical parameters

Requirements

Having chosen β_v and β_w, the DNS numerical parameters should be such that: a) the Ekman layers are well resolved, b) the dissipative range of wavenumbers is captured, c) the spatial period is large enough to avoid effects of periodicity, d) the time step is sufficiently small.

Condition (a) requires a large enough number of Chebyshev polynomials denoted as $T_b(x) = \cos(b\theta)$, where $x = 2x_3 - 1$, $\cos\theta = x$ and $0 \leq \theta \leq \pi$. Close to the wall at $x_3 = 1$, $\theta^2 \sim 4(1 - x_3)$, so that $\theta = O(\mathrm{E}^{1/4})$ in the Ekman layer. Thus, to resolve the Ekman layer, b is required to be large compared with $2\pi\mathrm{E}^{-1/4}$, which takes a value ≈ 84 for $\beta_v = 0.019$ and $\beta_w = 3.4$. This means that, say, 840 polynomials are required to resolve the Ekman layers.

Condition (b) means that the maximum wavenumber of DNS should include the dissipative range. The wave-turbulence closure gives $k_{dis} \approx 225$ for the given physical parameters. Thus, the maximum DNS wavenumber should be larger than 225. We chose a value $2\pi N_i/L = 452$, where N_i is the number of Fourier components in each of the directions x_1, x_2. Note that, because of truncation and the resulting aliasing problems, we do not expect the DNS results to be accurate all the way up to the maximum wavenumber. Here, we have taken the maximum wavenumber to be twice the dissipative one.

Concerning condition (c), the group velocity of waveguide modes is given by

$$c_n(\mathbf{k}) = \nabla_{\mathbf{k}}\omega_n(k) = -\frac{n\pi\mathbf{k}}{\left(k^2 + n^2\pi^2\right)^{3/2}},$$

which is equation (4.1) of [27]. The maximum of $\left|c_n\right|(k)$, arising from $n = 1$ and $k = \pi/\sqrt{2}$, is 0.12, hence modes propagate a maximum distance $0.12t_c$ up to the critical time. Thus, a spatial period of $L >> 0.12t_c$ is required to avoid effects of periodicity. Taking $t_c \approx 60$, the spatial period should be larger than $L \approx 8$. Taking $L = 32$ and $2\pi N_i/L = 452$, there should be $N_i \approx 2300$ Fourier components in both periodic directions. We carried out calculations for different values of L, hence different N_i, to see how the results converged as L increases.

Finally, condition (d) requires that the time step be small compared with the rotation time. The actual time step used was determined by numerical experimentation as explained in the

next section. Numerical stability also plays an important role in this choice.

Time and space resolution

As indicated in Table 6.1, DNS runs were performed for three different values of L and N_i determined by $2\pi N_i/L = 452$. 864 Chebyshev polynomials were used in all cases.

Case	$N_1 \times N_2$	L
DNS 576	576×576	8.0
DNS 1152	1152×1152	16.0
DNS 2304	2304×2304	32.0

Table 6.1.: DNS cases.

The time step is strongly constrained by numerical stability, described by a CFL number that should theoretically remain lower than $\sqrt{3}$. The used time step was $\Delta t = 0.001$, for which the CFL number is always below 1.2. The maximum CFL number was found to occur near the walls because it is there that the velocity gradients are large. It is the stable description of those parts of the flow that places the strongest restriction on the time step.

To study convergence with respect to the time step, we compared the DNS results with an exact analytical solution of the linearized Navier-Stokes equations in the rotating channel. There is a family of such solutions:

$$\begin{pmatrix} u_1 \\ u_2 \\ u_3 \end{pmatrix} = a \exp\left\{-\mathrm{E} l^2 \pi^2 t\right\} \sin l\pi x_3 \begin{pmatrix} \sin(t+\phi) \\ \cos(t+\phi) \\ 0 \end{pmatrix},$$

where a is an arbitrary amplitude, ϕ an arbitrary phase and l can take any positive integer value. We chose the case $\mathrm{E} = 10^{-3}$, $a = 0.2\sqrt{5}$, $l = 1$, $\phi = \pi/6$ and initialised the DNS using the above velocity field. Figure 6.1 shows DNS results. Rotation is apparent via the oscillations, whose non-dimensional frequency is very close to the value 1 of the analytical solution. Viscosity leads to exponential decay at a rate which is also close to the analytical value.

Figure 6.2 shows the results of a comparison between DNS and the analytical solution. It indicates that the time scheme is of the expected order, namely 3. The relative error is 10^{-6} for a time step of $\Delta t = 0.01$, which one would think an adequate accuracy. However, as noted above, stability imposes more stringent requirements than accuracy when we come to the full problem and $\Delta t = 0.001$ was used in the turbulence simulations. Note that these results verify correctness of the implementation of rotation in the DNS code.

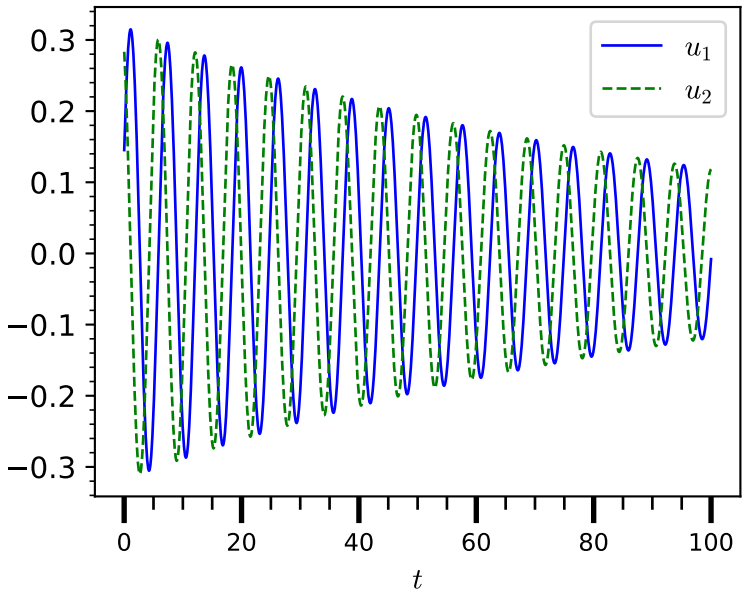

Figure 6.1.: Time evolution of the velocity components at $(x_1/L, x_2/L, x_3) = (0.5, 0.5, 0.25)$; $\Delta t = 0.01$.

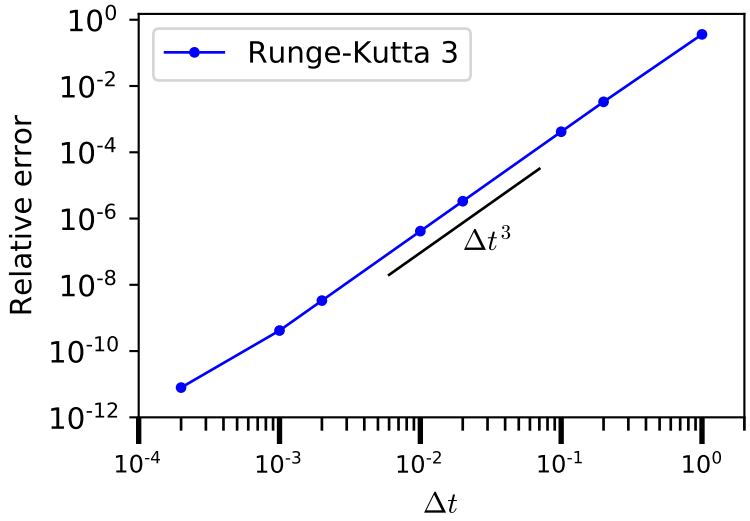

Figure 6.2.: Convergence of the DNS with respect to the time step.

6.3. Initialization

This section describes the construction of the initial flow field consistent with the initial energy spectrum used in the wave-turbulence simulations and with the velocity representation of the DNS code. This field is based on the inviscid wave-guide mode, so that even though no-slip conditions are imposed, at later times the initial condition involves slip. This means that the DNS has subsequently to impose no slip by creating Ekman layers of growing thickness at the walls.

6.3.1. Construction of the initial velocity field using the inviscid basis

The wave-turbulence model describes the time evolution of the energy spectra $B_n(k,T)$. Here $k = \left(k_1^2 + k_2^2\right)^{1/2}$ where (k_1, k_2) is the two-dimensional wave vector parallel to the walls and n the mode order associated with the wall-normal direction x_3. The initial form of the spectrum spectra is

$$B_n(k) = C \exp\left\{-\frac{k^2 + n^2\pi^2}{\Xi^2}\right\},$$

where Ξ is the spectral width and C a constant of normalisation ensuring that

$$2\pi \sum_{n=1}^{\infty} \int_0^{\infty} k B_n(k)\, \mathrm{d}k = 1.$$

The B_n are the diagonal elements of a spectral matrix, $A_{nm}(k,t)$, rescaled according to $B_n(k) = \varepsilon^{-2} A_{nn}(k)$. The initialization of the DNS consists in generating velocity components in the physical space, building a flow field that is consistent with given $A_{nm}(k,0)$.

Modal expression of the velocity field

In DNS, the velocity field is approximated as periodic in x_1 and x_2. For simplicity's sake we suppose equal periods in the two coordinates. Using the basis set of inviscid, inertial waveguide modes and truncating the modal order to $|n| \leq N$, the velocity components are defined in each physical point (x_1, x_2, x_3) by

$$u_i(x_1, x_2, x_3) = \sum_{n=-N}^{N} \sum_{k_1,k_2} \alpha_n(\mathbf{k}) W_i^{(n)}(x_3; \mathbf{k}) \exp\{\mathrm{i}k_1 x_1 + \mathrm{i}k_2 x_2\}, \tag{6.1}$$

where $\mathbf{k} = (k_1, k_2)$, $\alpha_n(\mathbf{k})$ are modal coefficients and $W_i^{(n)}(x_3; \mathbf{k})$ describes the modal structure in the cross-channel direction. The inner sum is over $k_1 = 2\pi l_1/L$ and $k_2 = 2\pi l_2/L$, where L is the spatial period and l_1 and l_2 are integers. The complex modal coefficients $\alpha_n(\mathbf{k})$ are random

variables, whose construction forms the main subject of this section. When $k \neq 0$, $W_i^{(n)}(x_3;\mathbf{k})$ is given by (3.6)-(3.8) and (3.10). However (3.6) and (3.7) involve a zero-by-zero division when $\mathbf{k} = 0$ and the construction of $W_i^{(n)}(x_3;0)$ requires special treatment, which is described next.

Taking the limit $\mathbf{k} \to 0$, equations (3.6)-(3.8) and (3.10) give

$$W_i^{(n)}(x_3;\mathbf{k}) \to V_i^{(n)}(x_3;\phi), \tag{6.2}$$

where $k = (k\cos\phi, k\sin\phi)$, $k = |\mathbf{k}| = \left(k_1^2 + k_2^2\right)^{1/2}$,

$$V_1^{(n)}(x_3;\phi) = (s_n\cos\phi + \mathrm{i}\sin\phi)\cos(n\pi x_3), \tag{6.3}$$

$$V_2^{(n)}(x_3;\phi) = (s_n\sin\phi - \mathrm{i}\cos\phi)\cos(n\pi x_3), \tag{6.4}$$

$$V_3^{(n)}(x_3;\phi) = 0, \tag{6.5}$$

$s_0 = 0$, $s_n = 1$ when $n > 0$ and $s_n = -1$ when $n < 0$. The angle ϕ represents the direction from which $\mathbf{k} = 0$ is approached. The quantity $W_i^{(n)}(x_3;0)$ in (6.1) is defined by

$$W_i^{(n)}(x_3;0) = \frac{1}{\sqrt{4M}}\sum_{r=0}^{4M-1} V_i^{(n)}(x_3;\phi_r)\exp\{\mathrm{i}\theta_r\}, \tag{6.6}$$

where $\phi_r = \pi r/2M$ and θ_r are random variables, uniformly distributed in $[0, 2\pi)$. The variables θ_r, $0 \leq r \leq 2M-1$ are statistically independent, while the remaining θ_r follow from

$$\theta_{2M+r} = -\theta_r \mod 2\pi \qquad 0 \leq r \leq 2M-1. \tag{6.7}$$

Equation (6.6) attempts to mimic the contribution to the integral in (3.11) from near $\mathbf{k} = 0$ as a sum over different directions of $\mathbf{k}$ in $0 \leq \phi < 2\pi$. We have in mind a largish value of M, say $M = 32$.

To summarise, when $\mathbf{k} \neq 0$, $W_i^{(n)}(x_3;\mathbf{k})$ is given by equations (3.6)-(3.8) is non-random, whereas $W_i^{(n)}(x_3;\mathbf{k})(x_3;0)$ is a random variable, given by (6.6). Equation (6.7) ensures that $W_i^{(-n)}(x_3;-\mathbf{k}) = W_i^{(n)*}(x_3;\mathbf{k})$ (* denotes complex conjugation) holds for $\mathbf{k} = 0$, as it does for $\mathbf{k} \neq 0$. It remains to construct the $\alpha_n(\mathbf{k})$ in (6.1), random variables which are chosen to be statistically independent of the θ_r.

Required properties of the $\alpha_n(\mathbf{k})$

To obtain a real velocity field, $\alpha_n(\mathbf{k})$ should satisfy $\alpha_n^*(\mathbf{k}) = \alpha_{-n}(-\mathbf{k})$ and, to ensure zero mean velocity, $\alpha_n(\mathbf{k})$ should have zero mean for $\mathbf{k} \neq 0$. Otherwise, the statistics are chosen according to a given spectral matrix, $A_{nm}(k)$. This matrix is Hermitian, positive semi-definite and has the

property $A_{-n,-m}(k) = A^*_{n,m}(k)$. The two-point velocity moments follow from (6.1) and statistical independence of $\alpha_n(\mathbf{k})$ and θ_r as

$$\overline{u_i(\mathbf{x})u_j(\mathbf{x}')} =$$

$$\sum_{n,m=-N}^{N} n \sum_{\substack{k_1,k_2\\ k_1',k_2'}} \overline{\alpha_n^*(\mathbf{k})\alpha_m(\mathbf{k}')}\,\overline{W_i^{(n)*}(x_3;\mathbf{k})W_j^{(m)}(x_3';\mathbf{k}')}\exp\{\mathrm{i}(k_1'x_1' - k_1x_1) + \mathrm{i}(k_2'x_2' - k_2x_2)\}. \tag{6.8}$$

Statistical homogeneity with respect to x_1 and x_2 implies that these moments only depend on $r_1 = x_1' - x_1$ and $r_2 = x_2' - x_2$, which is ensured by requiring

$$\overline{\alpha_n^*(\mathbf{k})\alpha_m(\mathbf{k}')} = \aleph_{nm}(\mathbf{k})\delta_{k_1k_1'}\delta_{k_2k_2'}, \tag{6.9}$$

where δ is the Kronecker delta. Thus (6.8) becomes

$$\overline{u_i(\mathbf{x})u_j(\mathbf{x}')} = \sum_{n,m=-N}^{N} \aleph_{nm}(0)\overline{W_i^{(n)*}(x_3;0)W_j^{(m)}(x_3';0)}$$

$$+ \sum_{n,m=-N}^{N}\sum_{\mathbf{k}\neq 0} \aleph_{nm}(\mathbf{k})W_i^{(n)*}(x_3;\mathbf{k})W_j^{(m)}(x_3';\mathbf{k})\exp\{\mathrm{i}k_1r_1 + \mathrm{i}k_2r_2\}, \tag{6.10}$$

where we have used the fact that $W_i^{(n*)}(x_3;\mathbf{k})W_j^{(m)}(x_3';\mathbf{k})$ is non-random when $\mathbf{k} \neq 0$. Equation (6.10) should yield an approximation of equation (3.4) of [27]. To represent the integral in that equation, the (k_1, k_2) plane is divided into small squares, each square being centred at one of the discrete values of $\mathbf{k}$ and having sides of length $2\pi/L$ in both the k_1 and k_2 directions. The first sum on the right-hand side of (6.10) represents the contribution from the square centred at $\mathbf{k} = 0$, whereas the second expresses contributions from all others. To obtain results that correspond, we take

$$\aleph_{nm}(\mathbf{k}) = \frac{4\pi^2}{L^2}A_{nm}(k) \qquad -N \le n, m \le N \tag{6.11}$$

for $\mathbf{k} \neq 0$ and

$$\aleph_{nm}(0) = \frac{4\pi^2}{L^2}A_{nm}(0) \qquad 0 \le n, m \le N. \tag{6.12}$$

The latter also holds for $-N \le n, m \le 0$ because $\aleph_{-n,-m}(0) = \aleph^*_{nm}(0)$ and $A_{-n,-m}(0) = A^*_{nm}(0)$. However, there is a significant difference with (6.11): there is no constraint on $\aleph_{nm}(0)$ for nonzero n and m having opposite signs. More details are given in Appendix G.

To summarise, the random coefficients $\alpha_k(\mathbf{k})$ should be such that $\alpha_n^*(\mathbf{k}) = \alpha_{-n}^*(-\mathbf{k})$, $\overline{\alpha_n(\mathbf{k})} = 0$ when $\mathbf{k} \neq 0$ and (6.9) holds, where $\aleph_{nm}(\mathbf{k})$ is given by (6.11) for $\mathbf{k} \neq 0$ and (6.12) for $\mathbf{k} = 0$. A final requirement is that (6.1) should yield a velocity field which is statistically homogeneous with respect to x_1 and x_2. This is ensured by (6.9) for the second-order moments, but the requirement of full statistical homogeneity is stronger.

Construction of the $\alpha_n(\mathbf{k})$

We first construct suitable $\alpha_n(\mathbf{k})$ for $\mathbf{k} \neq 0$. Since $A_{nm}(k)(-N \leq n, m \leq N)$ is Hermitian and positive semi-definite, it has a complete set of $2N+1$ complex eigenvectors, $X_n^{(p)}(k)$, having real eigenvalues $\lambda^{(p)}(k) \geq 0$. The $X_n^{(p)}(k)$ are orthogonal in the sense that

$$\sum_{n=-N}^{N} X_n^{(p)*}(k) X_n^{(q)}(k) = \delta_{pq}. \tag{6.13}$$

This relation expresses both orthogonality and normalisation of the eigenvectors. As shown at the end of appendix G, the matrix $A_{nm}(k)$ can be expressed as a sum over its eigenvectors as

$$A_{nm}(k) = \sum_p \lambda^{(p)}(k) X_n^{(p)}(k) X_m^{(p)*}(k) \qquad -N \leq n, m \leq N \tag{6.14}$$

Since $A_{-n,-m}(k) = A_{n,m}^*(k)$, it can be shown that the eigenvectors may be chosen such that $X_{-n}^{(p)}(k) = X_n^{(p)*}(k)$, which we assume is the case. The coefficients $\alpha_n(\mathbf{k})$ are determined using

$$\alpha_n(\mathbf{k}) = \frac{2\pi}{L} \sum_p \sqrt{\lambda^{(p)}(k)} X_n^{(p)*}(k) \exp\{\mathrm{i}\psi_p(\mathbf{k})\} \qquad -N \leq n, m \leq N, \tag{6.15}$$

where $\psi_p(\mathbf{k})$ are random phases, uniformly distributed in $[0, 2\pi)$. To ensure that $\alpha_n^*(\mathbf{k}) = \alpha_{-n}(-\mathbf{k})$, we require that

$$\psi_p(-\mathbf{k}) = -\psi_p(\mathbf{k}) \mod 2\pi. \tag{6.16}$$

Apart from (6.16), the $\psi_p(\mathbf{k})$ are statistically independent. Note that the eigenvectors and eigenvalues should be determined as described in Appendix G, otherwise there is no guarantee that $X_{-n}^{(p)}(k) = X_n^{(p)*}(k)$.

Next consider the case $\mathbf{k} = 0$. The approach used is similar to that for $\mathbf{k} \neq 0$. Since $A_{nm}(0)$ $(0 \leq n, m \leq N)$ is Hermitian and positive semi-definite, it has a complete set of $N+1$ complex eigenvectors, $X_n^{(p)}(0)$, having real eigenvalues $\lambda^{(p)}(0) \geq 0$. The $X_n^{(p)}(0)$ are orthonormal in the sense that

$$\sum_{n=0}^{N} X_n^{(p)*}(k) X_n^{(q)}(k) = \delta_{pq}. \tag{6.17}$$

Using reasoning similar to that employed to derive (6.14)

$$A_{nm}(0) = \sum_p \lambda^{(p)}(0) X_n^{(p)}(0) X_m^{(p)*}(0) \qquad 0 \leq n, m \leq N. \tag{6.18}$$

Let

$$\beta_n = \frac{2\pi}{L} \sum_p \sqrt{\lambda^{(p)}(0)} X_n^{(p)*}(0) \exp\left\{\mathrm{i}\tau_p\right\} \qquad 0 \leq n \leq N, \tag{6.19}$$

where the τ_p are random phases, uniformly distributed in $[0, 2\pi)$ and statistically independent of each other and of the $\psi_p(\mathbf{k})$. If $\beta_0 = 0$ we take $\alpha_n(0) = \beta_n$, otherwise, writing $\beta_0 = |\beta_0| \exp\{\mathrm{i}\gamma\}$, $\alpha_n(0) = \beta_n \exp\{-\mathrm{i}\gamma\}$. This defines $\alpha_n(0)$ for $0 \le n \le N$, while $\alpha_{-n}(0) = \alpha_n^*(0)$ for $1 \le n \le N$ is used to complete the $\alpha_n(0)$. Note that $\alpha_0(0)$ is real, hence $\alpha_{-n}(0) = \alpha_n^*(0)$ for all $|n| \le N$.

We now want to show that the $\alpha_n(\mathbf{k})$, given by (6.15) for $k \neq 0$ and the above procedure for $\mathbf{k} = 0$ satisfy all the requirements described at the end of the previous section. It is evident from (6.15) that the mean value of $\alpha_n(\mathbf{k})$ is zero for $\mathbf{k} \neq 0$, as it should be. Furthermore, (6.16) for $\mathbf{k} \neq 0$ and $\alpha_{-n}(0) = \alpha_n^*(0)$ imply $\alpha_n^*(\mathbf{k}) = \alpha_{-n}(-\mathbf{k})$ for all $\mathbf{k}$. Concerning statistical homogeneity, using (6.15) in (6.1),

$$\begin{aligned} u_i &= \sum_{n=-N}^{N} \alpha_n(0) W_i^{(n)}(x_3; 0) \\ &+ \frac{2\pi}{L} \sum_{n=-N}^{N} \sum_{\mathbf{k}\neq 0} \sum_p \sqrt{\lambda^{(p)}(k)}\, X_n^{(p)*}(k) W_i^{(n)}(x_3; \mathbf{k}) \exp\Big\{\mathrm{i}k_1 x_1 + \mathrm{i}k_2 x_2 + \mathrm{i}\psi_p(\mathbf{k})\Big\}. \end{aligned} \tag{6.20}$$

The translation $x_1 \mapsto x_1 + d_1$, $x_2 \mapsto x_2 + d_2$ yields the velocity field

$$\begin{aligned} u_i &= \sum_{n=-N}^{N} \alpha_n(0) W_i^{(n)}(x_3; 0) \\ &+ \frac{2\pi}{L} \sum_{n=-N}^{N} \sum_{\mathbf{k}\neq 0} \sum_p \sqrt{\lambda^{(p)}(k)}\, X_n^{(p)*}(k) W_i^{(n)}(x_3; \mathbf{k}) \exp\Big\{\mathrm{i}k_1 x_1 + \mathrm{i}k_2 x_2 + \mathrm{i}\tilde{\psi}_p(\mathbf{k})\Big\}, \end{aligned} \tag{6.21}$$

where

$$\tilde{\psi}_p(\mathbf{k}) = \psi_p(\mathbf{k}) + k_1 d_1 + k_2 d_2 \mod 2\pi. \tag{6.22}$$

Given the definition of the $\psi_p(\mathbf{k})$, the statistics of the $\tilde{\psi}_p(\mathbf{k})$ are the same as those of $\psi_p(\mathbf{k})$, hence the velocity field resulting from (6.20) is statistically homogeneous with respect to x_1 and x_2. Using (6.15),

$$\overline{\alpha_n^*(\mathbf{k})\alpha_m(\mathbf{k}')} = \frac{4\pi^2}{L^2} \sum_{p,q} \sqrt{\lambda^{(p)}(k)\lambda^{(q)}(k')}\, X_n^{(p)}(k) X_m^{(q)*}(k') \overline{\exp\Big\{\mathrm{i}\Big(\psi_q(\mathbf{k}') - \psi_p(\mathbf{k})\Big)\Big\}} \tag{6.23}$$

for nonzero $\mathbf{k}$ and $\mathbf{k}'$. Given the definition of the $\psi_p(\mathbf{k})$, the average on the right-hand side is zero unless $\mathbf{k}' = \mathbf{k}$ and $q = p$. Thus, using (6.14), we obtain (6.9) with $\aleph_{nm}(\mathbf{k})$ given by (6.11). Since the $\alpha_n(\mathbf{k})$ for $\mathbf{k} \neq 0$ are of zero mean and statistically independent of the $\alpha_n(0)$, $\overline{\alpha_n^*(\mathbf{k})\alpha_m(0)} = \overline{\alpha_n^*(0)\alpha_m(\mathbf{k}')} = 0$, i.e. (6.9) also holds when one of $\mathbf{k}$ and $\mathbf{k}'$ is zero and the other

nonzero. Finally,

$$\begin{aligned}\overline{\alpha_n^*(0)\alpha_m(0)} &= \overline{\beta_n^*\beta_m} \\ &= \frac{4\pi^2}{L^2}\sum_{p,q}\sqrt{\lambda^{(p)}(0)\lambda^{(q)}(0)}\,X_n^{(p)}(0)X_m^{(q)*}(0)\overline{\exp\left\{\mathrm{i}\left(\tau_q-\tau_p\right)\right\}}\end{aligned} \tag{6.24}$$

for $0 \le n, m \le N$. Given the definition of the τ_p, the average on the right-hand side is zero unless $q = p$. Thus, using (6.18), we obtain (6.12).

Construction of the velocity field

Equations (6.1) and (6.6) imply

$$u_i = \frac{1}{\sqrt{4M}}\sum_{n=-N}^{N}\sum_{r=0}^{4M-1}\alpha_n(0)V_i^{(n)}(x_3;\phi_r)\exp\{\mathrm{i}\theta_r\} + \sum_{n=-N}^{N}\sum_{\mathbf{k}\neq 0}\alpha_n(\mathbf{k})W_i^{(n)}(x_3;\mathbf{k})\exp\{\mathrm{i}k_1x_1+\mathrm{i}k_2x_2\}. \tag{6.25}$$

Because

$$\alpha_{-n}(0)V_i^{(-n)}(x_3;\phi_{2M+r})\exp\{\mathrm{i}\theta_{2M+r}\} = \left(\alpha_n(0)V_i^{(n)}(x_3;\phi_r)\exp\{\mathrm{i}\theta_r\}\right)^* \tag{6.26}$$

for $0 \le r \le 2M-1$ and

$$\alpha_{-n}(-\mathbf{k})W_i^{(-n)}(x_3;-\mathbf{k})\exp\{-\mathrm{i}k_1x_1-\mathrm{i}k_2x_2\} = \left(\alpha_n(\mathbf{k})W_i^{(n)}(x_3;\mathbf{k})\exp\{\mathrm{i}k_1x_1+\mathrm{i}k_2x_2\}\right)^* \tag{6.27}$$

for $\mathbf{k} \neq 0$, (6.25) can be written as

$$\begin{aligned}u_i =& \frac{1}{\sqrt{4M}}\sum_{n=-N}^{N}\sum_{r=0}^{2M-1}\alpha_n(0)V_i^{(n)}(x_3;\phi_r)\exp\{\mathrm{i}\theta_r\} \\ &+ \sum_{n=-N}^{N}\sum_{\mathbf{k}\in H}\alpha_n(\mathbf{k})W_i^{(n)}(x_3;\mathbf{k})\exp\{\mathrm{i}k_1x_1+\mathrm{i}k_2x_2\} + c.c.,\end{aligned} \tag{6.28}$$

where H represents $\mathbf{k}$ such that either $k_1 > 0$ or $k_1 = 0, k_2 > 0$ and $+c.c.$ denotes addition of the complex conjugate. The result can be expressed as

$$u_i = \sum_{n=-N}^{N}\alpha_n(0)\breve{W}_i^{(n)}(x_3) + \sum_{n=-N}^{N}\sum_{\mathbf{k}\in H}\alpha_n(\mathbf{k})W_i^{(n)}(x_3;\mathbf{k})\exp\{\mathrm{i}k_1x_1+\mathrm{i}k_2x_2\} + c.c., \tag{6.29}$$

where

$$\breve{W}_i^{(n)}(x_3) = \frac{1}{\sqrt{4M}}\sum_{r=0}^{2M-1}V_i^{(n)}(x_3;\phi_r)\exp\{\mathrm{i}\theta_r\} \tag{6.30}$$

(6.29) has the advantage over (6.1) that we can forget about the constraints (6.7) and (6.16). The required random variables, θ_r $(0 \le r \le 2M-1)$, $\psi_p(\mathbf{k})$ $(\mathbf{k} \in H)$ and τ_p, are statistically independent.

Choice of spectral matrix

The diagonal elements of the spectral matrix, $A_{nm}(k)$, employed in the construction of the initial velocity field, are taken to match the initial conditions of the wave-turbulence calculation, i.e. $A_{nn}(k) = \varepsilon^2 B_n(k)$ for $t = 0$. However, this does not give $A_{00}(k)$, nor the off-diagonal elements of $A_{nm}(k)$, which must be chosen such that $A_{nm}(k)$ has the required properties, i.e. it is Hermitian, positive semi-definite and $A_{-n,-m}(k) = A^*_{nm}(k)$. One such choice is

$$A_{nm}(k) = aA_{nn}(k)\delta_{nm} + (1-a)\zeta_{n-m}\sqrt{A_{nn}(k)A_{mm}(k)}, \tag{6.31}$$

where $\zeta_p = 1$ for even p and $\zeta_p = 0$ for odd p. (6.31) provides a whole family of possible spectral matrices, parameterised by $0 \le a \le 1$. The factor ζ_{n-m} makes inertial modes of even order independent of those of odd order, which ensures that the velocity field is statistically symmetric under reflection ($x_3 \mapsto 1 - x_3$) about the channel centre plane. Note that the $A_{nm}(k)$ given by (6.31) is diagonal when $a = 1$ and deficient (of rank 2) when $a = 0$. Hence, an intermediate value, $a = 1/2$, has been used.

The wave-turbulence code uses the initial values

$$B_n(k) = C\exp\left\{-\frac{k^2 + n^2\pi^2}{\Xi^2}\right\}, \tag{6.32}$$

where Ξ determines the spectral width and

$$C = \frac{1}{\pi\Xi^2\sum_{n=1}^{\infty}\exp\left\{-n^2\pi^2/\Xi^2\right\}}. \tag{6.33}$$

This implies

$$A_{nn}(k) = \varepsilon^2 C\exp\left\{-\frac{k^2 + n^2\pi^2}{\Xi^2}\right\} \tag{6.34}$$

for $n \neq 0$, which, for simplicity's sake, is extended to $n = 0$. Using (6.34), (6.31) becomes

$$A_{nm}(k) = \varepsilon^2 C\Phi_{nm}(k)\exp\left\{-\frac{k^2}{\Xi^2}\right\}, \tag{6.35}$$

where

$$\Phi_{nm}(k) = a\exp\left\{-\frac{n^2\pi^2}{\Xi^2}\right\}\delta_{nm} + (1-a)\zeta_{n-m}\exp\left\{-\frac{(n^2+m^2)\pi^2}{2\Xi^2}\right\}. \tag{6.36}$$

6.4. Annular spectra, energy and volumetric dissipation

6.4.1. Approximation of the spectral matrix

DNS gives a periodic approximation of the turbulent velocity field of the form

$$u_i = \sum_{k_1,k_2} \breve{u}_i(x_3;\mathbf{k})\exp\{\mathrm{i}k_1x_1 + \mathrm{i}k_2x_2\}, \tag{6.37}$$

where $\mathbf{k} = (k_1, k_2)$, the sum is over $k_1 = 2\pi l_1/L$, $k_2 = 2\pi l_2/L$, L is the spatial period, and l_1, l_2 are integers. DNS provides the coefficients in the expansion

$$\breve{u}_i(x_3;\mathbf{k}) = \sum_{b=0}^{N_b} \hat{u}_i^b(\mathbf{k}) T_b(x), \tag{6.38}$$

where $x = 2x_3 - 1$ and $T_b(x)$ are the Chebyshev polynomials.

According to (6.37), the two-point velocity correlations are

$$\overline{u_i(\mathbf{x})u_j(\mathbf{x}')} = \sum_{\mathbf{k},\mathbf{k}'} \overline{\breve{u}_i^*(x_3;\mathbf{k})\breve{u}_j(x_3';\mathbf{k}')} \exp\{\mathrm{i}(k_1'x_1' - k_1x_1) + \mathrm{i}(k_2'x_2' - k_2x_2)\}. \tag{6.39}$$

Statistical homogeneity of the flow (which is preserved by DNS) implies that only terms with $\mathbf{k}' = \mathbf{k}$ are nonzero, thus

$$\overline{u_i(\mathbf{x})u_j(\mathbf{x}')} = \sum_{\mathbf{k}} \overline{\breve{u}_i^*(x_3;\mathbf{k})\breve{u}_j(x_3;\mathbf{k})} \exp\{\mathrm{i}k_1r_1 + \mathrm{i}k_2r_2\}, \tag{6.40}$$

where $r_1 = x_1' - x_1$ and $r_2 = x_2' - x_2$. Expressing the Fourier coefficients $\breve{u}_i(x_3;\mathbf{k})$ for $\mathbf{k} \neq 0$ using the basis set $W_i^{(n)}(x_3;\mathbf{k})$,

$$\breve{u}_i(x_3;\mathbf{k}) = \sum_{-\infty}^{\infty} \breve{v}_n(\mathbf{k}) W_i^{(n)}(x_3;\mathbf{k}), \tag{6.41}$$

where

$$\breve{v}_n(\mathbf{k}) = \int_0^1 \breve{u}_i(x_3;\mathbf{k}) W_i^{(n)*}(x_3;\mathbf{k})\, \mathrm{d}x_3 \tag{6.42}$$

follows from orthogonality, (2.11) of [27], of the $W_i^{(n)}(x_3;\mathbf{k})$. Using (6.41) in (6.40),

$$\begin{aligned}\overline{u_i(\mathbf{x})u_j(\mathbf{x}')} &= \overline{\breve{u}_i^*(x_3;0)\breve{u}_j(x_3';0)} \\ &\quad + \sum_{n,m}\sum_{\mathbf{k}\neq 0} \overline{\breve{v}_n^*(\mathbf{k})\breve{v}_m(\mathbf{k})} W_i^{(n)*}(x_3;\mathbf{k}) W_i^{(n)}(x_3';\mathbf{k}) \exp\{\mathrm{i}k_1r_1 + \mathrm{i}k_2r_2\},\end{aligned} \tag{6.43}$$

in which the first term on the right-hand side represents the $\mathbf{k} = 0$ contribution.

The two-point moments can also be expressed using equation (3.4) of [27]. As in the last section, the integral is approximated as a sum of contributions from small squares in the $\mathbf{k}$-plane. Identifying $\mathbf{k} \neq 0$ terms in the resulting sum with those of (6.43) and using (3.6) of [27], gives the approximation of the spectral matrix

$$A_{nm}(k) = \frac{L^2}{4\pi^2} \overline{\breve{w}_n^*(\mathbf{k})\breve{w}_m(\mathbf{k})}, \tag{6.44}$$

where $\breve{w}_n(\mathbf{k}) = \exp\{\mathrm{i}\omega_n(k)t\}\breve{v}_n(\mathbf{k})$. Note that the factor $\exp\{\mathrm{i}\omega_n(k)t\}$ in the definition of $\breve{w}_n(\mathbf{k})$ suppresses the modal oscillations of linear, inviscid theory. As in the last section, the case $\mathbf{k} = 0$ is singular because it gives rise to a zero by zero division in the definition of $W_i^{(n)}(x_3;\mathbf{k})$. Rather than trying to handle this special case, we simply do not calculate the spectral matrix for $\mathbf{k} = 0$.

Calculation of the $\breve{v}_n(\mathbf{k})$

Equations (3.6)-(3.8) give $W_1^{(n)*}(x_3;\mathbf{k}) = Z_1^{(n)}(\mathbf{k})\ \cos n\pi x_3$, $W_2^{(n)*}(x_3;\mathbf{k}) = Z_2^{(n)}(\mathbf{k})\ \cos n\pi x_3$ and $W_3^{(n)*}(x_3;\mathbf{k}) = Z_3^{(n)}(\mathbf{k})\ \sin n\pi x_3$, where

$$Z_1^{(n)}(\mathbf{k}) = \frac{k_1\omega_n(k) - \mathrm{i}k_2}{k}, \tag{6.45}$$

$$Z_2^{(n)}(\mathbf{k}) = \frac{k_2\omega_n(k) + \mathrm{i}k_1}{k}, \tag{6.46}$$

$$Z_3^{(n)}(\mathbf{k}) = \frac{\mathrm{i}k}{(k^2 + n^2\pi^2)^{1/2}}\ . \tag{6.47}$$

Writing $x = \cos\theta\ \ (0 \le \theta \le \pi)$ equations (6.38) and (6.43) yield

$$\breve{v}_n(\mathbf{k}) = \frac{1}{2}\,\sigma_i^{(n)}\,Z_i^{(n)}(\mathbf{k}), \tag{6.48}$$

where it should be recalled that there is an implicit sum over i. The $\sigma_i^{(n)}$ are given by

$$\sigma_1^{(n)}(\mathbf{k}) = \sum_{b=0}^{N_b} H_{bn}\hat{u}_1^b(\mathbf{k}), \tag{6.49}$$

$$\sigma_2^{(n)}(\mathbf{k}) = \sum_{b=0}^{N_b} H_{bn}\hat{u}_2^b(\mathbf{k}), \tag{6.50}$$

$$\sigma_3^{(n)}(\mathbf{k}) = \sum_{b=0}^{N_b} G_{bn}\hat{u}_3^b(\mathbf{k}) \tag{6.51}$$

with

$$G_{bn} = \int_0^\pi \sin\theta\cos b\theta\sin(\frac{1}{2}\,n\pi(1+\cos\theta))d\theta, \tag{6.52}$$

$$H_{bn} = \int_0^\pi \sin\theta\cos b\theta\cos(\frac{1}{2}\,n\pi(1+\cos\theta))d\theta \tag{6.53}$$

and we have used $T_b(\cos\theta) = \cos b\theta$. Note that

$$\sigma_1^{(-n)}(\mathbf{k}) = \sigma_1^{(n)}(\mathbf{k}), \qquad \sigma_2^{(-n)}(\mathbf{k}) = \sigma_2^{(n)}(\mathbf{k}), \qquad \sigma_3^{(-n)}(\mathbf{k}) = -\sigma_3^{(n)}(\mathbf{k}) \tag{6.54}$$

can be used to treat negative n.

Implementation of the above procedure requires calculation of G_{bn} and H_{bn}, which in turn involves the evaluation of the integrals appearing in their definitions. Rather than employing a standard numerical integration rule, we used an analytic representation for the integrals as sums over Bessel functions. We do not give details here, but the results are much more accurate and robust to large values of n or b.

Annular averaging

Taken literally, the evaluation of the ensemble average in (6.44) would require a large number of DNS runs with randomly varying initial conditions. This is not feasible and we use a method that approximates the average using a single run of DNS, i.e. just one realisation of the ensemble. Given statistical isotropy, the obvious method, adopted here, consists of averaging over annular regions in the $\mathbf{k}$-plane. Let $0 \le k_- < k_+$ and define the average of $\breve{w}_n^*(\mathbf{k})\breve{w}_m(\mathbf{k})$ over the annulus $k_- < k \le k_+$:

$$\langle \breve{w}_n^*(\mathbf{k})\breve{w}_m(\mathbf{k})\rangle = \frac{1}{K}\sum_{\mathbf{k}\in D} \breve{w}_n^*(\mathbf{k})\breve{w}_m(\mathbf{k}), \tag{6.55}$$

where K is the number of discrete $\mathbf{k}$ inside the annulus, denoted D . Note that K should be nonzero, otherwise division by zero occurs. Note also that, because we have disallowed $\mathbf{k} = 0$, none of the annuli include this wave vector. The hope is that (6.55), which varies randomly from one realisation to another in the statistical ensemble of flows, provides an approximation to the ensemble average in (6.44). According to the general principles of statistics, this requires large K, otherwise the statistical fluctuations in $\breve{w}_n^*(\mathbf{k})\breve{w}_m(\mathbf{k})$ will be comparable with $\overline{\breve{w}_n^*(\mathbf{k})\breve{w}_m(\mathbf{k})}$ and it will not yield an approximation of the ensemble average. Note that $\breve{w}_n(-\mathbf{k}) = \breve{w}_{-n}^*(\mathbf{k})$, hence $\breve{w}_n^*(-\mathbf{k})\breve{w}_m(-\mathbf{k}) = \breve{w}_{-m}^*(\mathbf{k})\breve{w}_{-n}(\mathbf{k})$ and (6.55) can be written as

$$\langle \breve{w}_n^*(\mathbf{k})\breve{w}_m(\mathbf{k})\rangle = \Sigma_{nm} \ + \Sigma_{-m,-n}, \tag{6.56}$$

where

$$\Sigma_{nm} \ = \frac{1}{K}\sum_{\mathbf{k}\in D_h} \breve{w}_n^*(\mathbf{k})\breve{w}_m(\mathbf{k}) \tag{6.57}$$

and D_h represents half the wave vectors in D. Specifically, D is split into two disjoint subsets, D_h and its partner, obtained via $\mathbf{k} \mapsto -\mathbf{k}$. (6.56) and (6.57) are advantageous from a numerical point of view because they reduce the calculation time. Note also that the matrix Σ_{nm} is Hermitian, allowing a further improvement in numerical speed.

Taking the ensemble average of (6.55) and using (6.44),

$$\frac{L^2}{4\pi^2}\overline{\langle \breve{w}_n^*(\mathbf{k})\breve{w}_m(\mathbf{k})\rangle} = \frac{L^2}{4\pi^2 K}\sum_{\mathbf{k}\in D}\overline{\breve{w}_n^*(\mathbf{k})\breve{w}_m(\mathbf{k})} = \frac{1}{K}\sum_{\mathbf{k}\in D} A_{nm}(k). \tag{6.58}$$

Thus, the ensemble average of $\langle \breve{w}_n^*(\mathbf{k})\breve{w}_m(\mathbf{k})\rangle$ yields the annular average of the spectral matrix. If $k_+ - k_-$ is small, the result approximates $A_{nm}(k)$ at $k = (k_+ + k_-)/2$. On the other hand, as noted above, we require a large number of $\mathbf{k}$ inside the annulus, so $k_+ - k_-$ must not be too small.

To be more specific, let us number the annuli $1 \le l \le N_a$, where N_a is the total number. Annulus l has $k_- = 2\pi r_{l-1}/L$ and $k_+ = 2\pi r_l/L$, where $0 = r_0 < r_1 < \cdots < r_{N_a} = r_{max}$ define the boundaries between neighbouring annuli. Thus, taken together, the annuli cover the range

$0 < k \leq 2\pi r_{max}/L$. Various choices of the r_l may be envisaged. One such makes r_l proportional to $l^{1/2}$, making the surface area the same for all annuli. Given the uniform distribution of DNS wave vectors in the **k**-plane, this yields approximately constant K. More precisely, let $r_l = \beta l^{1/2}$, then

$$K = \pi\beta^2, \tag{6.59}$$

obtained by multiplying the annular surface area by the density of wave vectors, should be a good approximation provided β is large (as it should be because we require large K). Another possibility is to take r_l proportional to l, in which case we expect K to increase with l in rough proportion. The problem with the latter choice is that it tends to place very few wave vectors in the first few annuli, thus calling into question the approximation of the ensemble average by the annular one. On the other hand, the former choice tends to make the number of annuli unnecessarily large because the annular width, $k_+ - k_-$, decreases as l increases. A third choice, namely

$$\frac{r_l^2}{r_l + \alpha} = l, \tag{6.60}$$

where $\alpha > 0$ is constant, is a compromise between the two previous choices. When $r_l \ll \alpha$ it yields $r_l \sim l^{1/2}$, whereas $r_l \sim l$ when $r_l \gg \alpha$. (6.60) yields annuli whose surface area increases with l, hence K also tends to increase. The number of wave vectors in the first annulus can be estimated as πr_1^2. Let K_m denote the desired number of such wave vectors, then $\pi r_1^2 = K_m$ gives r_1 and (6.60) implies

$$\alpha = r_1(r_1 - 1) \tag{6.61}$$

for the constant α.

Using the annular average to approximate $A_{nm}(k)$, the result has random fluctuations from realisation to realisation. To obtain a good approximation, these fluctuations should be small compared with $A_{nm}(k)$ itself. Figure 6.3 and Figure 6.4 show results of using annular averaging at the initial time. The annuli were chosen according to $r_l = \beta l^{1/2}$, where β was calculated from (6.59) with the desired value $K = 50$ for the number of wave vectors per annulus. The value $L = 16$ was used. Figure 6.3 shows results of three independent realisations, as well as the exact initial spectra. The fluctuations about the exact spectra are apparent, but are moderately small (about 28%). The low-order modes tend to have smaller percentage fluctuations than the higher-order ones. Figure 6.4 illustrates the effects of varying the desired K for the modal order $n = 3$. For $K = 10$, the spectra cannot be calculated in some annuli because they contain no wave vectors (this is shown with discontinuities of the corresponding line). In addition, the fluctuations are unacceptably large for this value of K. As expected, the fluctuations decrease with increasing K and, in keeping with our conclusions concerning Figure 6.3, are found to be moderately small for $K = 50$.

In the DNS runs whose results are described in section 6.5, we used (6.60) and, to give some breathing space, we choose $K_m = 200$ for the desired minimal number of wave vectors.

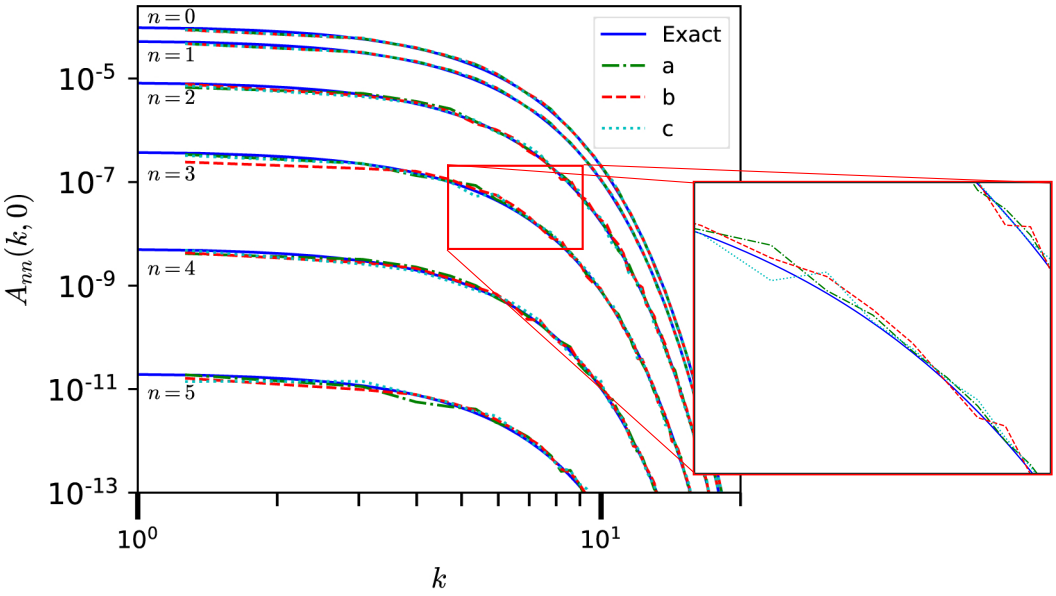

Figure 6.3.: The initial energy spectra obtained by annular averaging for three independent realizations a, b and c. Also shown are the exact spectra.

The calculation of $A_{nm}(k)$ was performed during the simulation, asynchronously to the Navier-Stokes solver.

6.4.2. Energy calculation

Let us define the energy as

$$E = \frac{1}{2}\int_0^1 [u_i u_i] dx_3, \tag{6.62}$$

where [] represents averaging with respect to x_1 and x_2. Thus, E (not to be confused with the Ekman number, E) is the energy per unit area in the (x_1, x_2)-plane, averaged across the channel. Using (6.1)

$$\begin{aligned}
[u_i u_i] &= \sum_{\mathbf{k},\mathbf{k}'} \breve{u}_i^*(x_3;\mathbf{k})\breve{u}_i(x_3;\mathbf{k}')[\exp\{\mathrm{i}(k_1' - k_1)x_1 + \mathrm{i}(k_2' - k_2)x_2\}] \\
&= \sum_{\mathbf{k}} \breve{u}_i^*(x_3;\mathbf{k})\breve{u}_i(x_3;\mathbf{k}) \\
&= \breve{u}_i^2(x_3;0) + \sum_{\mathbf{k}\neq 0} \breve{u}_i^*(x_3;\mathbf{k})\breve{u}_i(x_3;\mathbf{k}),
\end{aligned} \tag{6.63}$$

where we have used the facts that $\breve{u}_i(x_3;0)$ is real (by Hermitian symmetry) and that the $x_1 - x_2$ average of the exponential is zero if $\mathbf{k}' \neq \mathbf{k}$ and equal to 1 when $\mathbf{k}' = \mathbf{k}$. Employing (6.41) and

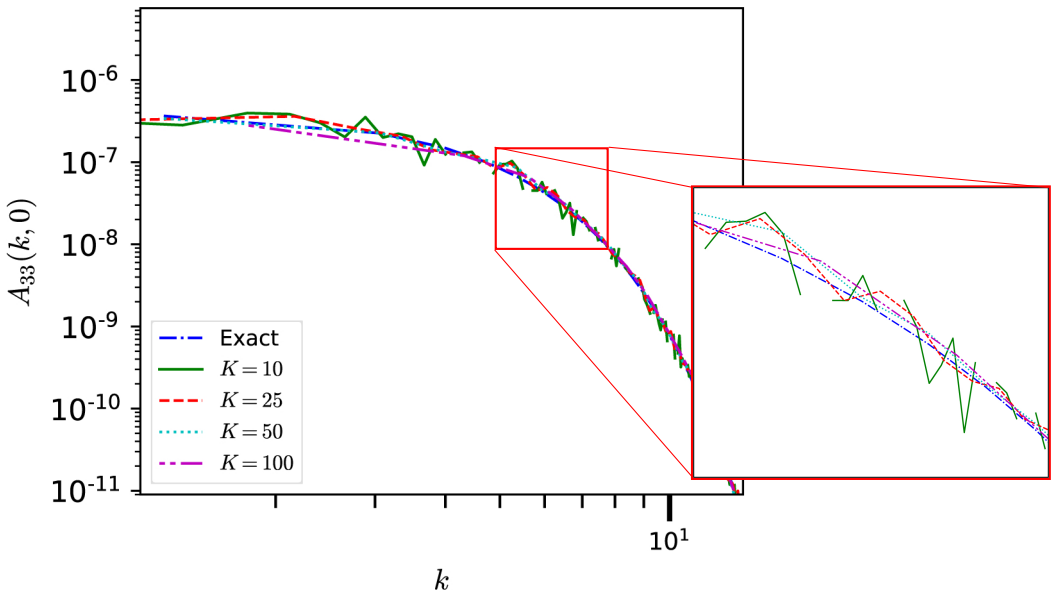

Figure 6.4.: Influence of the desired K on $A_{nn}(k,0)$ for $n=3$.

(2.21) of [27],

$$\int_0^1 \breve{u}_i^*(x_3;\mathbf{k})\breve{u}_i(x_3;\mathbf{k})\,\mathrm{d}x_3 = \sum_{n=-\infty}^{\infty} \left|\breve{v}_n(\mathbf{k})\right|^2. \tag{6.64}$$

Summing over $\mathbf{k}\neq 0$, we obtain the contribution

$$\frac{1}{2}\sum_{\mathbf{k}\neq 0}\sum_n \left|\breve{v}_n(\mathbf{k})\right|^2 \tag{6.65}$$

to E, where the summation over n is truncated to the finite range, $n\leq N$, which is treated numerically. Assuming the annuli used for averaging cover the range of nonzero wave vectors which have significant energy, we can approximate (6.65) as

$$\sum_{D_h}\sum_{\mathbf{k}\in D_h}\sum_n \left|\breve{v}_n(\mathbf{k})\right|^2, \tag{6.66}$$

where we have used $\left|\breve{v}_{-n}(-\mathbf{k})\right|^2 = \left|\breve{v}_n(\mathbf{k})\right|^2$. Since $\breve{v}_n(\mathbf{k})$ has already been calculated for the annular average, very little extra numerical work is required to compute (6.66).

Because we have restricted attention to $\mathbf{k}\neq 0$, the $\mathbf{k}=0$ contribution is treated differently. We have

$$\breve{u}_i(x_3;0) = \sum_{b=0}^{N_b} \hat{u}_i^b(0)T_b(x), \tag{6.67}$$

hence

$$\frac{1}{2}\int_0^1 \breve{u}_i^2(x_3;0)\,\mathrm{d}x_3 = \frac{1}{4}\sum_{b,b'=0}^{N_b} I_{bb'}\hat{u}_i^b(0)\hat{u}_i^{b'}(0) \tag{6.68}$$

is the $\mathbf{k} = 0$ contribution to E, where

$$\begin{aligned} I_{bb'} &= 2\int_0^1 T_b(x)T_{b'}(x)\,\mathrm{d}x_3 \\ &= \int_0^\pi \sin\theta\cos b\theta\cos b'\theta\,\mathrm{d}\theta. \end{aligned} \tag{6.69}$$

The integral can be evaluated as

$$I_{bb'} = \frac{1}{1-(b+b')^2} + \frac{1}{1-(b-b')^2} \tag{6.70}$$

if b and b' have the same parity and $I_{bb'} = 0$ otherwise.

Because the wave-turbulence model does not treat $n = 0$ modes, these modes must be excluded from the DNS energy calculation when comparing with WTC. This is achieved for the nonzero k contribution, (6.66), by dropping the $n = 0$ contribution. However, there is no obvious way of removing $n = 0$ modes from (6.68) so we simply neglect the $k = 0$ contribution to the energy. Because $k = 0$ represents one Fourier component of many, the result should be very close to what it would have been had $k = 0$ been included.

6.4.3. D_v calculation

D_v is defined by equation (5.4). It represents the volumetric viscous dissipation appearing in the wave-turbulence model and only includes modes with $n \neq 0$. Thus, it represents only part of the overall dissipation. The contribution to the integral in (5.4) from each annulus is approximated by

$$\pi\varepsilon^{-2}\beta_v\left(k_+^2 - k_-^2\right)\sum_{n=1}^{N}\left(\frac{1}{2}\left(k_+^2 + k_-^2\right) + n^2\pi^2\right)A_{nn}, \tag{6.71}$$

where A_{nn} is the result of annular averaging. The sum of (6.71) over all annuli yields D_v.

6.5. Results

Appendix I compares DNS results for the three cases indicated in Table 6.1. It is found that the case $N_i = 576$ differs from the other two, which are quite close, indicating convergence for higher N_i.

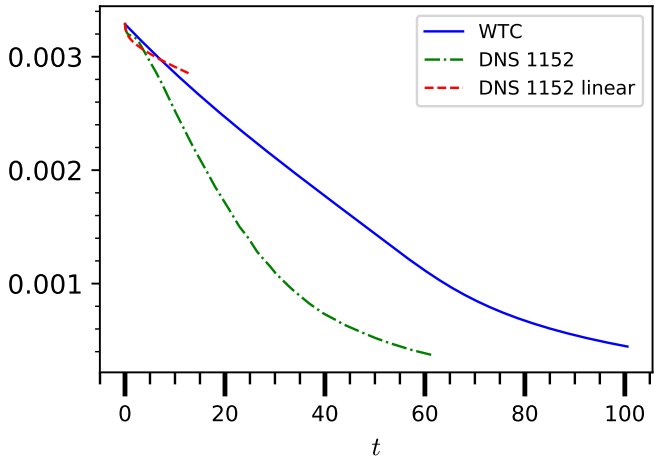

Figure 6.5.: Evolution of energy (excluding $n = 0$ and $k = 0$) with time, t.

Because WTC does not treat modes with $n = 0$, such modes are excluded when comparing with DNS. Figure 6.5 shows the evolution of the energy, excluding $n = 0$ and $k = 0$ as described earlier, as a function of time, t. Results are given for WTC, DNS and a version of DNS in which nonlinearity is dropped. The WTC and DNS results differ noticeably by about $t = 10$. Linear and nonlinear DNS have significant differences by about the same time, indicating that nonlinearity is important at such times. Recalling that the critical time according to WTC is $t \approx 60$, this is the time required for nonlinear transfer to produce a full spectrum and for a volumetric dissipative range to form according to WTC. DNS predicts the much more rapid appearance of nonlinearity and greater dissipation.

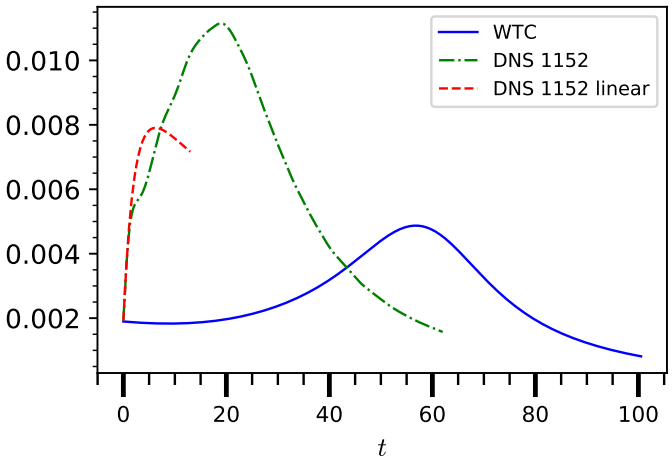

Figure 6.6.: Evolution of D_v with time.

Figure 6.6 shows $D_v(t)$. There are considerable differences between WTC and DNS. The DNS equivalent of the critical time is about one third of the WTC one and the level of DNS dissipation is higher. The departure of linear from nonlinear DNS again indicates a time for significant nonlinearity of about 10.

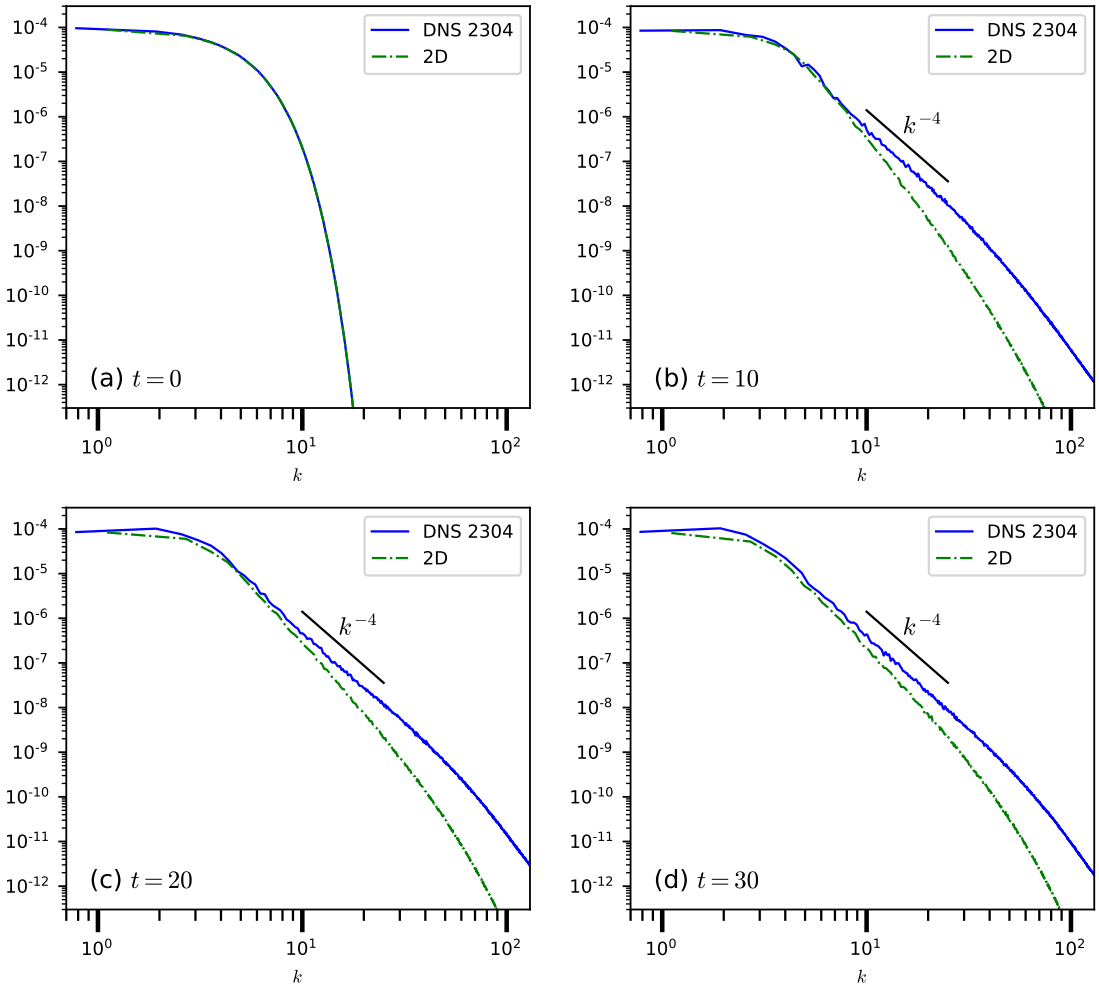

Figure 6.7.: Spectrum $A_{00}(k)$.

In summary, there are considerable differences between WTC and DNS which appear to be due to stronger nonlinearity in the latter approach. The time, $t \approx 10$, for significant nonlinearity in DNS is much too short for wave-turbulence theory to apply. That theory is based on modal oscillations which are rapid on the nonlinear time scale. Given that the period of the most rapidly oscillating modes ($k = 0$) is 2π, if nonlinearity occurs at $t = 10$, as in the DNS, there are not enough periods to make WTC work. At such short times, the mechanism which makes resonant triads dominant is ineffective and all triads can contribute to energy transfer,

thus making the process more rapid. In any case, it is apparent that there is no point in detailed comparison of WTC and DNS results because they differ significantly. This is not to say that turbulence evolution according to DNS and WTC show no similarities, they appear to be qualitatively similar, but with different time scales. Thus, in what follows, we present DNS results without direct comparison with WTC.

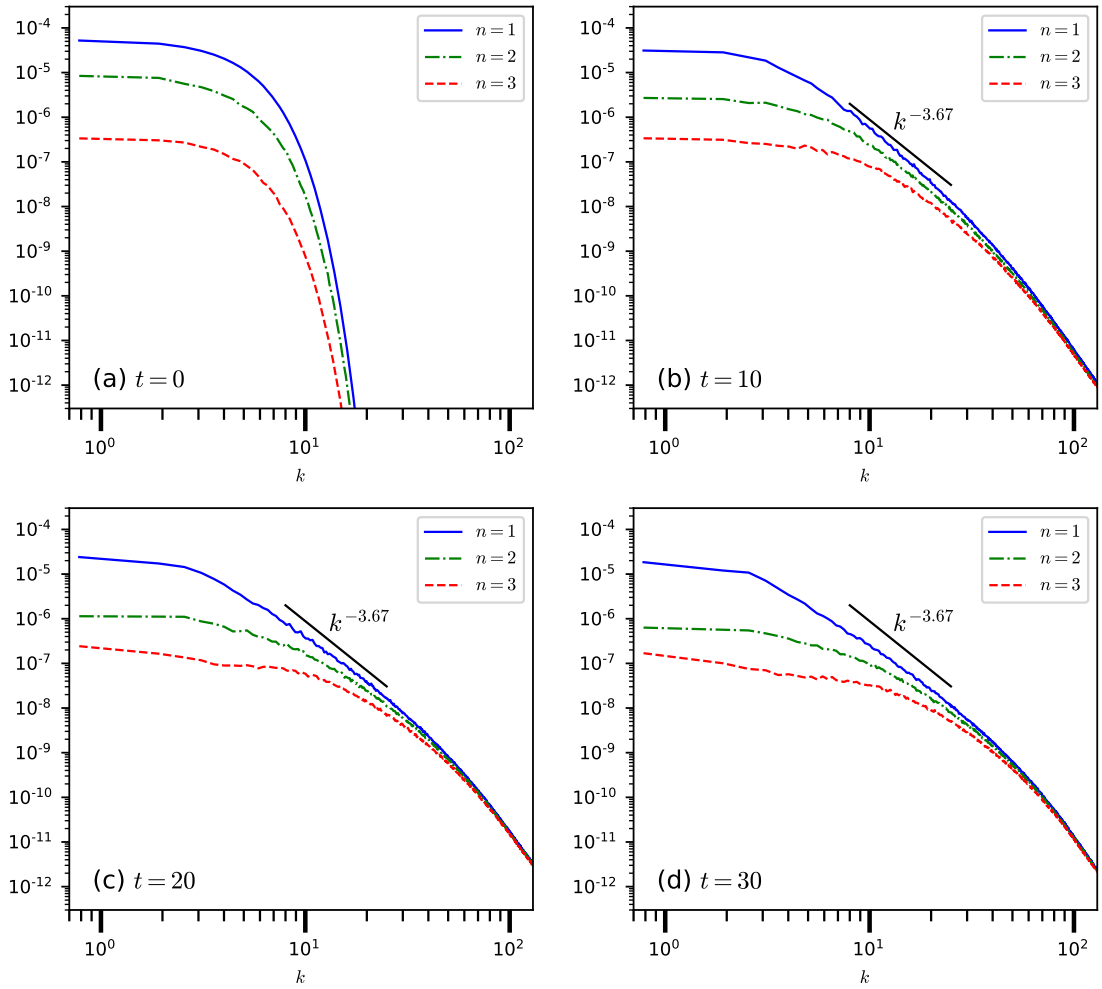

Figure 6.8.: Spectra $A_{nn}(k)$ for $n = 1, 2, 3$.

Figure 6.7 shows the spectrum, $A_{00}(k)$, at different times. In [27] it was conjectured that this component of the flow should evolve according to equations (4.10) and (4.11) of that article. These are essentially the 2D Navier-Stokes equations, but with an additional term representing wall damping. It is thus interesting to compare 3D DNS with a 2D DNS including wall damping. Figure 6.7 shows that they are quite close at smaller wavenumbers, but differ at larger ones. In particular, 3D DNS appears to be less dissipative so the spectral levels are higher and

the dissipative range occurs at larger k. Because $A_{00}(k)$ needs to be multiplied by $2\pi k$ to obtain the usual 2D energy spectrum, the indicated slope of -4 corresponds to the k^{-3} spectrum of 2D turbulence theory. Some additional results of 2D DNS are given in Appendix J.

Figure 6.8 shows $A_{nn}(k)$ for n other than 0 at different times. The results again indicate the rapidity of nonlinear energy transfer with the formation of a full spectrum and a dissipative range by about $t = 20$. They also show an inertial range for $n = 1$. Interestingly, the spectral slope is not far from the value -3.67 which was found using WTC (recall Figure 5.9 and Figure 5.10). Given the differences between the WTC and DNS results noted above, this may well be coincidental.

Finally, it may be of interest to visualize the flow in physical space. Figures (6.9)-(6.12) show gray-scale plots of the x_3 component of vorticity in a plane parallel to the walls for $N_i = 576$ and $N_i = 1152$ at different times. Given the qualitative character of these figures, the vorticity has been normalized to lie between -1 and $+1$. However, the normalization respects zero vorticity and is the same for all figures. Both 3D and 2D results are given. In the 2D plots, only the $n = 0$ component of the flow is relevant. It will be seen that there are many vortices, the number increasing with N_i because L is larger according to Table 6.1. More fine structure is visible for 3D than for 2D DNS.

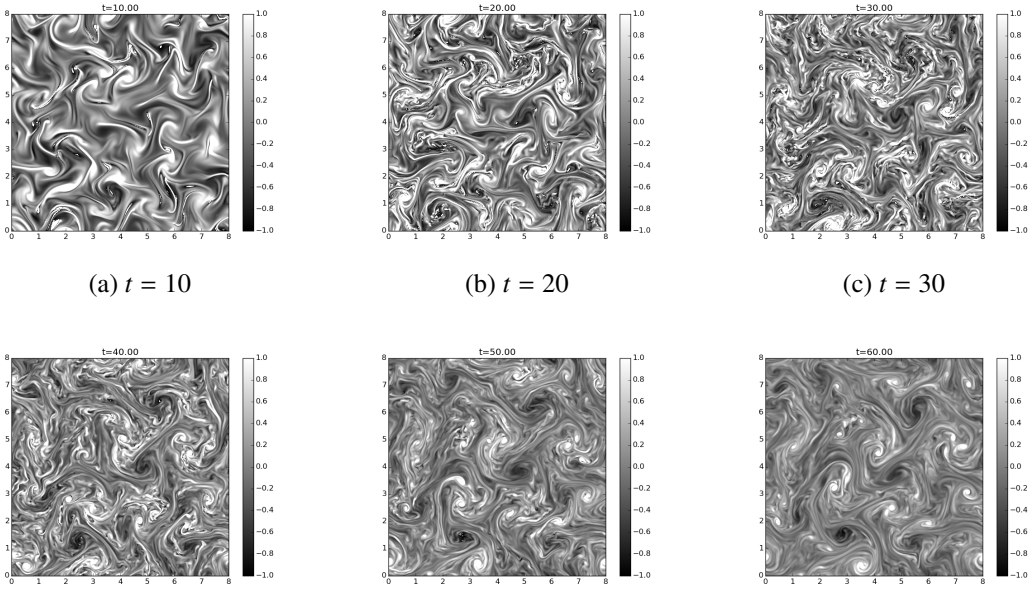

(a) $t = 10$ (b) $t = 20$ (c) $t = 30$

(d) $t = 40$ (e) $t = 50$ (f) $t = 60$

Figure 6.9.: Vorticity; DNS 576, $x_3 = 0.25$

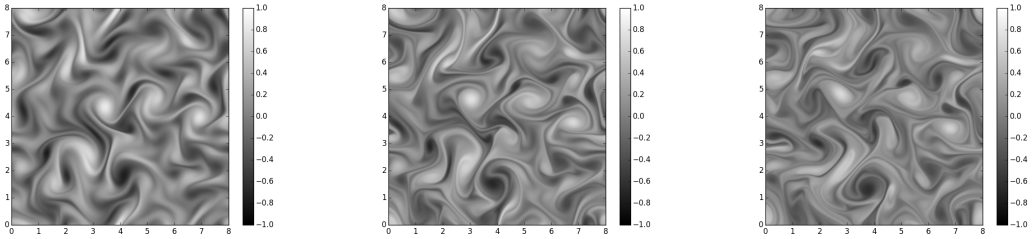

(a) $t = 10$ (b) $t = 20$ (c) $t = 30$

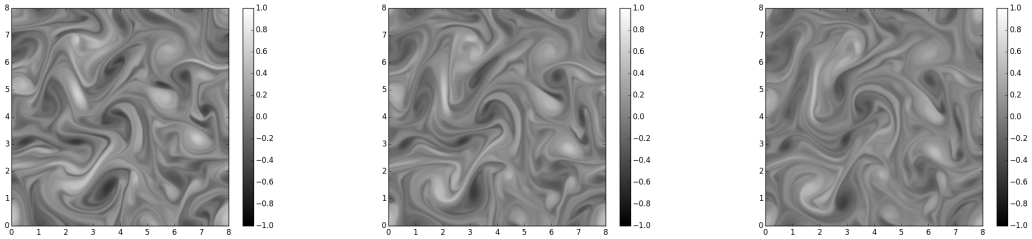

(d) $t = 40$ (e) $t = 50$ (f) $t = 60$

Figure 6.10.: Vorticity; DNS 2D 576.

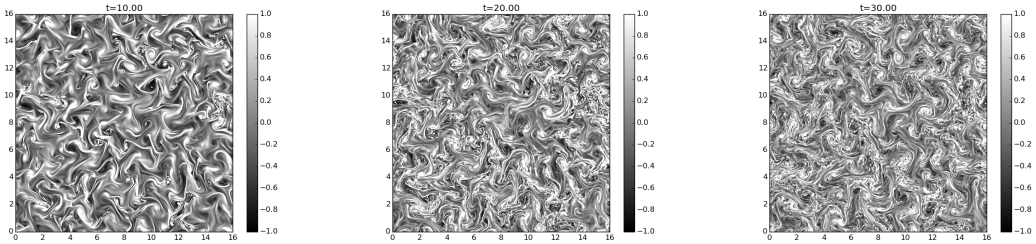

(a) $t = 10$ (b) $t = 20$ (c) $t = 30$

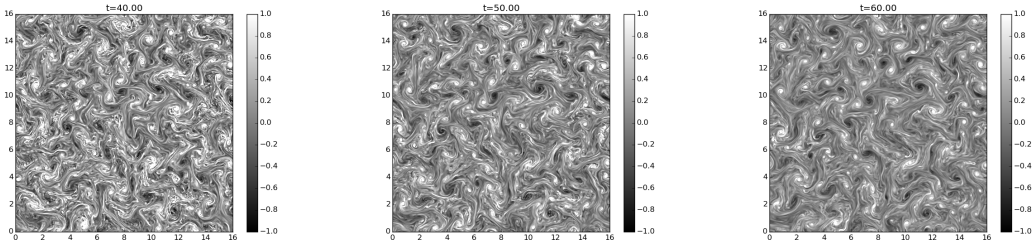

(d) $t = 40$ (e) $t = 50$ (f) $t = 60$

Figure 6.11.: Vorticity; DNS 1152, $x_3 = 0.25$

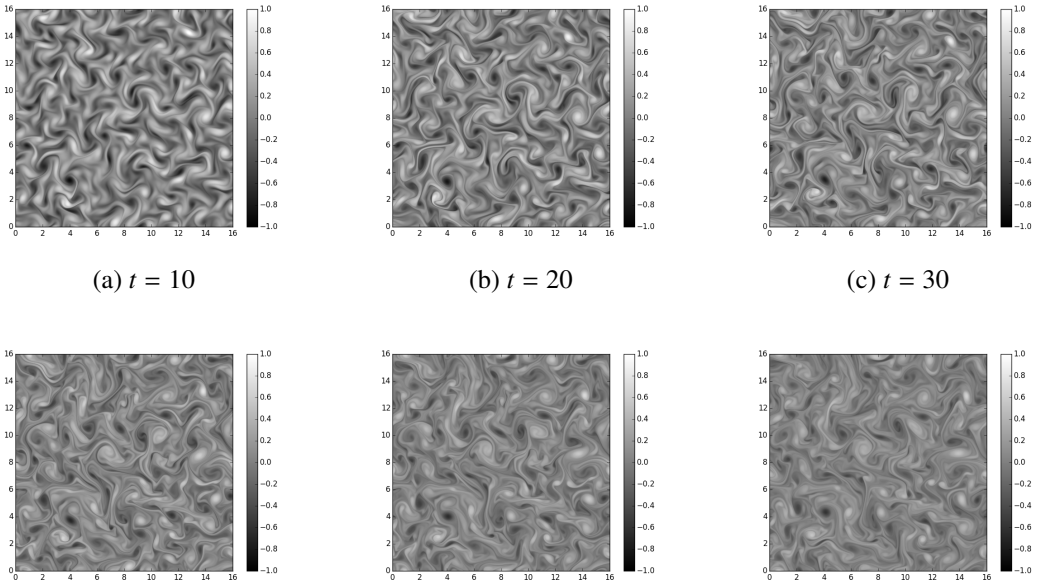

(a) $t = 10$ (b) $t = 20$ (c) $t = 30$

(d) $t = 40$ (e) $t = 50$ (f) $t = 60$

Figure 6.12.: Vorticity; DNS 2D 1152.

7. Conclusion

This thesis describes results for decaying turbulence in a rapidly rotating channel, the axis of rotation being perpendicular to the channel walls. The turbulence is homogeneous and isotropic parallel to the walls, but their existence makes it inhomogeneous in the wall-normal direction. Rapid rotation means a small Rossby number for which the effects of rotation dominate nonlinearity. This, in turn, suggests the use of wave-turbulence theory. The unbounded case, homogeneous in all directions, was treated in [3]. The rotating channel was analysed in [27], the wave-turbulence equations for the energy spectra being derived and some of their consequences discussed. However, detailed results were not available at that stage because there was no numerical implementation of the equations. The consequent objectives of this PhD were to implement the spectral-evolution equations of [27], to determine their consequences and to attempt a comparison with DNS.

Chapter 2 concerns the linear, inertial waveguide modes which are building blocks of the wave-turbulence closure of [27]. Starting with the classical case of plane inertial waves in an unbounded domain, the complex dispersion relation and helical modes were derived. The former is important in two respects: the real part of the modal frequency follows the well-known inviscid dispersion relation, while the imaginary part represents one of the two viscous-damping mechanisms, namely volumetric damping, which later plays an important role in spectral evolution according to wave-turbulence theory. The helical modes, i.e. the velocity fields of plane waves, are often used in spectral analysis of unbounded rotating turbulence such as [3], but are insufficient for the wall-bounded flows considered here because they take no account of the walls.

The second part of chapter 2 allows for the walls, located at $x_3 = 0, 1$ in the Cartesian system (x_1, x_2, x_3), which is used to describe the flow. The inviscid waveguide modes are derived. These modes are essential to the wave-turbulence closure of [27] and their detailed analysis in chapter 2 is intended to help the reader to understand the origin of equations (3.6)-(3.9) of chapter 3, which may otherwise appear somewhat opaque. They can be interpreted as the sum of two plane waves, the one being the reflection by the walls of the other. An important consequence of confinement is the discretisation of the wall-normal component of the wave vectors of these waves to be $\pm n\pi$, where n is an integer, referred to as the modal order. The component parallel to the walls, $\mathbf{k} = (k_1, k_2)$, of the waves is the same, hence $\mathbf{K} = (k_1, k_2, \pm n\pi)$ are the three-dimensional wave vectors of the two waves. Thus, the inviscid waveguide modes are parameterised by $\mathbf{k}$ and n.

Viscosity leads to modal damping, which is the sum of two components: volumetric and wall damping. The volumetric damping rate is $\mathrm{E}K^2$, just as for plane waves, whereas the wall-damping rate depends only on the direction of $\mathbf{K}$ relative to the rotation vector and is thus independent of $K = |\mathbf{K}|$. Thinking in terms of different scales of a turbulent flow, volumetric damping behaves in the usual manner and should thus stop any cascade to scales which are too small, whereas wall-damping will not.

Chapter 3 describes the essentials of the wave-turbulence theory of [27]. The velocity field is expressed as a sum over the inviscid waveguide modes, each having a modal amplitude $a_n(\mathbf{k})$. These amplitudes evolve in time according to equations which allow for the viscous effects discussed above, but there are additional nonlinear terms representing interactions between modes. A spectral matrix, $A_{nm}(k)$, is defined, whose diagonal elements represent the distribution of energy over the different modes. The velocity field is separated into a two-dimensional component, $n = 0$, and a wave component, $n \neq 0$. The former is incompatible with wave-turbulence analysis, because $n = 0$ modes are non-dispersive, whereas the latter has diagonal elements which evolve according to equation (3.20), which is the wave-turbulence energy equation. According to the wave-turbulence closure, this equation governs the time evolution of the energy spectra, $A_{nn}(k)$, for $n \neq 0$.

The linear term in (3.20) expresses the viscous damping mechanisms discussed earlier. The nonlinear term consists of an integral and represents interactions with two other waveguide modes, $\mathbf{p}$, n_p and $\mathbf{q}$, n_q, which requires $\mathbf{k} + \mathbf{p} + \mathbf{q} = 0$ and that one of the four conditions $n \pm n_p \pm n_q = 0$ be satisfied. The integral is over the resonance curve, $C_{nn_pn_q}(\mathbf{k})$, in the $\mathbf{p}$-plane defined by $\omega_n(k) + \omega_{n_p}(p) + \omega_{n_q}(|\boldsymbol{k} + \boldsymbol{p}|) = 0$, a condition for resonant triads which arises from wave-turbulence theory. This condition expresses dominance of near resonant interactions in the weak turbulence limit for which wave-turbulence closure applies.

One consequence of the dominance of resonant interactions arises because a resonance curve with given n, n_p and n_q can shrink to zero size, then disappear, as k is decreased. When that happens, the integral in (3.20) drops from a nonzero limiting value to zero. Although the initial spectra employed in this study are smooth functions of k, such discontinuous jumps in the nonlinear transfer term lead to spectral discontinuities at later times. Of course, we do not expect discontinuities in the real spectra, just rapid variations near the values of k for which wave-turbulence theory predicts a discontinuity. These rapid changes in the spectra should become more and more rapid the smaller the Rossby number.

Chapter 4 concerns the numerical implementation of (3.20) and its verification. Firstly, a Rossby number, ε, is explicitly introduced by making the change of variables $B_n(k) = \varepsilon^{-2}A_{nn}(k)$, $T = \varepsilon^2 t$. This does not alter the form of (3.20), which implies (4.1) with (4.2)-(4.5). It does however introduce the scaled time variable $T = \varepsilon^2 t$ which is appropriate to the slow spectral evolution at small ε. The viscous damping term in equation (4.2) is given by (4.5). The coefficients β_w and β_v correspond to wall and volumetric damping. The initial spectra are taken to have the Gaussian form (4.7), which is normalised using (4.6). This normalisation

can be thought of as providing a precise definition of the Rossby number. The quantity Ξ appearing in the initial spectra is referred to as the spectral width. It completes the set of three parameters, Ξ, β_w and β_v, of the problem.

For numerical purposes, k is discretised and the corresponding values of $B_n(k)$ used to describe the spectra. The main numerical task is the evaluation of integrals over the resonance curves. Small steps are taken along the curve and the contribution of each step to the integral obtained by multiplying the step length by the value of the integrand at mid-step. The latter involves interpolation of the spectra between adjacent discrete k. Another issue is the time stepping scheme, which is second order and chosen so that the spectra cannot become negative, a condition known as realizability.

The numerical scheme was tested in a variety of ways including accuracy of the resonance-curve integrals and energy conservation by the nonlinear transfer terms. The numerical parameters were varied to verify that the expected orders of convergence were respected.

Chapter 5 gives results. Firstly, the time evolution of the overall energy, volumetric and wall dissipation rates were presented. For small enough β_v, there is an abrupt transition between two phases of evolution at a time referred to as the critical time, T_c. Prior to the critical time, wall dissipation dominates volumetric dissipation and there is a decay in the energy which becomes more marked the larger β_w. Following the critical time, volumetric damping takes over as the dominant dissipative mechanism and power-law dependency on T is found. The critical time is insensitive to β_w and β_v provided the latter is small enough, but it depends strongly on the spectral width: the larger Ξ the smaller T_c.

Results concerning the time evolution of the spectra are described in the second half of chapter 5. Again focussing on the case of small β_v, prior to the critical time it is found that a spectral front advances towards larger k, leaving an inertial range behind it. Evidently this is a reflection of an energy cascade from large to small scales. Approximate power-law behaviour occurs in the inertial range, the term approximate being used because the appearance of spectral discontinuities muddies the picture. The front moves more and more rapidly as the critical time is approached. At the critical time, the front comes to a halt and a dissipative range is formed due to volumetric damping. Subsequently, volumetric dissipation balances transfer from the larger scales. The rapidity of advancement of the front just prior to the critical time is the reason that the transition between the two phases of evolution of the energy is so abrupt. Following the critical time one can identify the dissipative range as a spectral front which gradually retreats. Oscillations of the spectra in the inertial range are observed close to and following the critical time.

Contour plots of $B_n(k)$ in the $(k, n\pi)$ plane show that the energy cascade takes place not only in k but also in n. This is not surprising because it is the overall wavenumber, $K = \left(k^2 + n^2\pi^2\right)^{1/2}$, which is inversely related to scale size. Thus, the cascade to small scales generates large k, but also large $n\pi$. However, the range attained in $n\pi$ before volumetric dis-

sipation intervenes is found to be considerably smaller than that attained in k, which suggests that the transfer in n is less efficient than that in k.

$B_n(k)$ gives the energy distribution over both k and n. For given k, one can include all values of n to get the distribution, $e(k)$, over k. Likewise, including all k for a given n yields e_n, the distribution over n. Not surprisingly, plotting $e(k)$ as a function of k or e_n as a function of n prior to the critical time shows an advancing spectral front, leaving behind an inertial range. A dissipative range is then established and the front subsequently retreats. The inertial-range power law of $e(k)$ appears to have an exponent of -2.2 which is insensitive to changes in the parameters of the problem.

As noted earlier, spectral discontinuities appear following spectral evolution. The strength of these discontinuities has a striking dependence on Ξ. The smaller Ξ, the stronger the discontinuities become.

Chapter 6 concerns DNS calculations, carried out using the NadiaSpectral code[1], adapted to include the effects of rotation, on various calculation clusters, including the supercomputer Turing[2] provided by IDRIS[3]. We knew from the start that such calculations were ambitious, being at the limits of the available compute power. Thus, there could only be a few.

Before embarking on such calculations, we needed to define the physical and numerical parameters, a process described in section 6.2 and which leads to a definite choice of all physical parameters and to the three DNS cases of Table 6.1. There was also an obvious need for initialization of the DNS having spectra consistent with WTC, the development of which is discussed in section 6.3. Section 6.4 concerns the methods used to extract the desired results, namely the spectra, energy and volumetric dissipation rate, from the DNS results.

Finally, section 6.5 gives results of the DNS calculations. Unfortunately, it turns out that nonlinearity is much stronger than predicted by WTC. This is no doubt because the time scale, $t \approx 10$, for significant nonlinearity given by DNS is too small to restrict the interacting wave vector triads to be near resonant. This would require a yet smaller Rossby number, which is not feasible given current computer resources.

[1] Visit the home page of NadiaSpectral code, https://perso.univ-lyon1.fr/marc.buffat/NadiaSpectral/index.html.

[2] Turing is an IBM Blue Gene/Q machine which has a remarkable energy efficiency (2.17 Gflops/W). For further information visit http://www.idris.fr/eng/turing/turing-presentation-eng.html.

[3] The Institute for Development and Resources in Intensive Scientific Computing. Find more information on the following page http://www.idris.fr/eng/info/missions-eng.html.

A. Expressions for the nonlinear coefficients

According to (A.8) and (A.9) of [27],

$$N_{nn_pn_q}(\mathbf{k},\mathbf{p}) = \frac{1}{2}\Big(I_{nn_pn_q}(\mathbf{k},\mathbf{p},-\mathbf{k}-\mathbf{p}) + I_{nn_qn_p}(\mathbf{k},-\mathbf{k}-\mathbf{p},\mathbf{p})\Big), \tag{A.1}$$

where

$$\begin{aligned}
I_{nn_pn_q}(\mathbf{k},\mathbf{p},\mathbf{q}) = {} & \frac{k_1p_2 - k_2p_1 + \mathrm{i}\,\mathbf{k}\cdot\mathbf{p}\,\omega_{n_p}(p)}{4kpq}\Big(\delta_{n-n_p-n_q} + \delta_{n+n_p-n_q} + \delta_{n-n_p+n_q} + \delta_{n+n_p+n_q}\Big) \\
& \times \Big(\mathbf{k}\cdot\mathbf{q}\,(1-\omega_n(k)\omega_{n_q}(q)) + \mathrm{i}(k_1q_2-k_2q_1)(\omega_n(k)-\omega_{n_q}(q))\Big) \\
& + \frac{kq(k_1p_2 - k_2p_1 + \mathrm{i}\,\mathbf{k}\cdot\mathbf{p}\,\omega_{n_p}(p))}{4p(k^2+n^2\pi^2)^{1/2}(q^2+n_q^2\pi^2)^{1/2}}\Big(\delta_{n-n_p-n_q} + \delta_{n+n_p-n_q} - \delta_{n-n_p+n_q} - \delta_{n+n_p+n_q}\Big) \\
& + \frac{\mathrm{i}n\pi p}{4kq(p^2+n_p^2\pi^2)^{1/2}}\Big(\delta_{n-n_p-n_q} - \delta_{n+n_p-n_q} + \delta_{n-n_p+n_q} - \delta_{n+n_p+n_q}\Big) \\
& \times \Big(\mathbf{k}\cdot\mathbf{q}\,(1-\omega_n(k)\omega_{n_q}(q)) + \mathrm{i}(k_1q_2-k_2q_1)(\omega_n(k)-\omega_{n_q}(q))\Big) \\
& + \frac{\mathrm{i}n\pi kpq}{4(k^2+n^2\pi^2)^{1/2}(p^2+n_p^2\pi^2)^{1/2}(q^2+n_q^2\pi^2)^{1/2}} \\
& \times \Big(\delta_{n-n_p-n_q} - \delta_{n+n_p-n_q} - \delta_{n-n_p+n_q} + \delta_{n+n_p+n_q}\Big),
\end{aligned} \tag{A.2}$$

and $\delta_0 = 1$ and $\delta_m = 0$ for $m \neq 0$. Observe that $I_{nn_pn_q}(\mathbf{k},\mathbf{p},\mathbf{q})$, and hence $N_{nn_pn_q}(\mathbf{k},\mathbf{p})$, is zero unless $n \pm n_p \pm n_q = 0$. Note also that $N_{nn_pn_q}(\mathbf{k},\mathbf{p})$ has the following symmetry property under the transformation $n_p \leftrightarrow n_q$, $\mathbf{p} \leftrightarrow -\mathbf{k}-\mathbf{p}$

$$N_{nn_pn_q}(\mathbf{k},\mathbf{p}) = N_{nn_qn_p}(\mathbf{k},-\mathbf{k}-\mathbf{p}). \tag{A.3}$$

We also introduce two functions, $\Lambda_{nn_pn_q}(p)$ and $\Xi_{nn_pn_q}(p)$, which are later used in expressions for $N_{nn_pn_q}(\mathbf{k},\mathbf{p})$ and $N_{n_qn_pn}(-\mathbf{k}-\mathbf{p},\mathbf{p})$ as $k \to 0$:

$$\Lambda_{nn_pn_q}(p) = \frac{n\pi}{4} p\Bigg[\frac{1-\omega_{n_q}(p)}{\left(p^2+n_p^2\pi^2\right)^{1/2}}\left(\delta_{n-n_p-n_q} - \delta_{n+n_p-n_q} + \delta_{n-n_p+n_q} - \delta_{n+n_p+n_q}\right) \\ - \frac{1-\omega_{n_p}(p)}{\left(p^2+n_q^2\pi^2\right)^{1/2}}\left(\delta_{n-n_p-n_q} + \delta_{n+n_p-n_q} - \delta_{n-n_p+n_q} - \delta_{n+n_p+n_q}\right)\Bigg], \quad \text{(A.4)}$$

$$\Xi_{nn_pn_q}(p) = -\frac{n\pi p}{2\left(p^2+n_p^2\pi^2\right)^{1/2}}(1-\omega_{n_q}(p))\left(\delta_{n-n_p-n_q} - \delta_{n+n_p-n_q} + \delta_{n-n_p+n_q} - \delta_{n+n_p+n_q}\right) \\ - \frac{1}{2}p(1-\omega_{n_p}(p)\omega_{n_q}(p))\left(\delta_{n-n_p-n_q} + \delta_{n+n_p-n_q} + \delta_{n-n_p+n_q} + \delta_{n+n_p+n_q}\right) \quad \text{(A.5)} \\ - \frac{p^3}{2\left(p^2+n_p^2\pi^2\right)^{1/2}\left(p^2+n_q^2\pi^2\right)^{1/2}}\left(\delta_{n-n_p-n_q} - \delta_{n+n_p-n_q} - \delta_{n-n_p+n_q} + \delta_{n+n_p+n_q}\right).$$

B. Proofs of identities used in [27] to show independence of the wave from the two-dimensional component

This appendix is devoted to analytical proofs of the identities,

$$\eta_{nn_p0}(\mathbf{k},\mathbf{p}) = 0 \tag{B.1}$$

for $|\mathbf{p}| = k$ and $n_p = -n \neq 0$ and

$$\eta_{n0n_q}(\mathbf{k},\mathbf{p}) + 2\lambda_{n0n_q}(\mathbf{k},\mathbf{p}) = 0 \tag{B.2}$$

for $|\mathbf{k}+\mathbf{p}| = k$ and $n_q = -n \neq 0$. These identities were used in section 5.4 of [27] to show that the 2D component of the flow does not influence the evolution of the wave component according to wave-turbulence theory. That is, the contribution of $n_p = 0$ or $n_q = 0$ to the sum in (3.20) is zero, leading to closure of that equation. This remarkable conclusion was justified in [27] by the numerical finding that the identities are satisfied to machine precision. Since then, we have obtained analytical proofs of the identities and it is perhaps of interest to give these proofs here.

First identity

To prove (B.1), from (A.2) for $p = k$ (here $p = |\mathbf{p}|$) and $n_p = -n \neq 0$ we obtain

$$\begin{aligned} I_{0n_pn}(-\mathbf{k}-\mathbf{p},\mathbf{p},\mathbf{k}) =& \frac{1}{2k^2|\mathbf{k}+\mathbf{p}|}(k_1p_2 - k_2p_1 - \mathrm{i}\omega_n(k)\mathbf{p}\cdot(\mathbf{k}+\mathbf{p})) \\ & \times(\mathbf{k}\cdot(\mathbf{k}+\mathbf{p}) + \mathrm{i}\omega_n(k)(k_1p_2 - k_2p_1)), \end{aligned} \tag{B.3}$$

$$\begin{aligned} I_{0nn_p}(-\mathbf{k}-\mathbf{p},\mathbf{k},\mathbf{p}) =& \frac{1}{2k^2|\mathbf{k}+\mathbf{p}|}(k_2p_1 - k_1p_2 + \mathrm{i}\omega_n(k)\mathbf{k}\cdot(\mathbf{k}+\mathbf{p})) \\ & \times(\mathbf{p}\cdot(\mathbf{k}+\mathbf{p}) - \mathrm{i}\omega_n(k)(k_2p_1 - k_1p_2)). \end{aligned} \tag{B.4}$$

B. Proofs of identities used in [27] to show independence of the wave from the two-dimensional component

Using these results in (A.1),

$$N_{0n_pn}(-\mathbf{k}-\mathbf{p},\mathbf{p}) = \frac{1-\omega_n^2(k)}{4k^2|\mathbf{k}+\mathbf{p}|}(k_1p_2-k_2p_1)(\mathbf{k}\cdot(\mathbf{k}+\mathbf{p})-\mathbf{p}\cdot(\mathbf{k}+\mathbf{p})), \tag{B.5}$$

gives zero because $\mathbf{k}\cdot(\mathbf{k}+\mathbf{p})-\mathbf{p}\cdot(\mathbf{k}+\mathbf{p}) = k^2-p^2 = 0$. Thus, (3.21) yields (B.1).

Second identity

According to (A.3), (3.21) and (3.22)

$$\eta_{nn_pn_q}(\mathbf{k},\mathbf{p}) + \eta_{nn_qn_p}(\mathbf{k},\mathbf{q}) + 2\lambda_{nn_pn_q}(\mathbf{k},\mathbf{p}) = \\ 8\,\mathrm{Re}\Big\{N^*_{nn_pn_q}(\mathbf{k},\mathbf{p})\Big(N_{n_qn_pn}(\mathbf{q},\mathbf{p}) + N_{n_pn_qn}(\mathbf{p},\mathbf{q}) + N_{nn_pn_q}(\mathbf{k},\mathbf{p})\Big)\Big\}, \tag{B.6}$$

where $\mathbf{q} = -\mathbf{k}-\mathbf{p}$. Using (A.1) we write

$$N_{n_qn_pn}(\mathbf{q},\mathbf{p}) + N_{n_pn_qn}(\mathbf{p},\mathbf{q}) + N_{nn_pn_q}(\mathbf{k},\mathbf{p}) = \\ \frac{1}{2}\Big(I_{n_qn_pn}(\mathbf{q},\mathbf{p},\mathbf{k}) + I_{n_qnn_p}(\mathbf{q},\mathbf{k},\mathbf{p}) + I_{n_pn_qn}(\mathbf{p},\mathbf{q},\mathbf{k}) + I_{n_pnn_q}(\mathbf{p},\mathbf{k},\mathbf{q}) \\ + I_{nn_pn_q}(\mathbf{k},\mathbf{p},\mathbf{q}) + I_{nn_qn_p}(\mathbf{k},\mathbf{q},\mathbf{p})\Big). \tag{B.7}$$

Integrating equation (F.1) of [27] over $\mathbf{p}$ gives

$$I_{nn_pn_q}(\mathbf{k},\mathbf{p},\mathbf{q}) = -I_{n_qn_pn}(\mathbf{q},\mathbf{p},\mathbf{k}). \tag{B.8}$$

Cyclic permutation of $(\mathbf{k},\mathbf{p},\mathbf{q})$ and (n,n_p,n_q) leads to

$$I_{n_pn_qn}(\mathbf{p},\mathbf{q},\mathbf{k}) = -I_{nn_qn_p}(\mathbf{k},\mathbf{q},\mathbf{p}) \tag{B.9}$$

and

$$I_{n_qnn_p}(\mathbf{q},\mathbf{k},\mathbf{p}) = -I_{n_pnn_q}(\mathbf{p},\mathbf{k},\mathbf{q}). \tag{B.10}$$

These results indicate that (B.7) is zero, hence (B.6) gives

$$\eta_{nn_pn_q}(\mathbf{k},\mathbf{p}) + \eta_{nn_qn_p}(\mathbf{k},\mathbf{q}) + 2\lambda_{nn_pn_q}(\mathbf{k},\mathbf{p}) = 0. \tag{B.11}$$

Taking $q = k$, $n_q = -n \neq 0$, $n_p = 0$ and applying (B.1) to the second term of (B.11) give (B.2).

C. Equipartition of energy

Dropping the dissipative term, (3.20) becomes

$$\frac{\partial A_{nn}(k)}{\partial t} = \sum_{n_p,n_q\neq 0} \oint_{C_{nn_pn_q}(\mathbf{k})} \frac{A_{n_pn_p}(p)\Big(\eta_{nn_pn_q}(\mathbf{k},\mathbf{p})A_{nn}(k) + \lambda_{nn_pn_q}(\mathbf{k},\mathbf{p})A_{n_qn_q}(|\mathbf{k}+\mathbf{p}|)\Big)}{\Gamma_{n_pn_q}(\mathbf{k},\mathbf{p})} |\,\mathrm{d}\mathbf{p}| \tag{C.1}$$

for $n \neq 0$. $C_{nn_pn_q}(\mathbf{k})$, $\lambda_{nn_pn_q}(\mathbf{k},\mathbf{p})$ and $\Gamma_{n_pn_q}(\mathbf{k},\mathbf{p})$ are symmetric under the transformation $n_p \leftrightarrow n_q$ and $\mathbf{p} \leftrightarrow -\mathbf{k}-\mathbf{p}$. Thus, (C.1) is equivalent to

$$\begin{aligned}\frac{\partial A_{nn}(k)}{\partial t} = \frac{1}{2}\sum_{n_p,n_q\neq 0} \oint_{C_{nn_pn_q}(\mathbf{k})} \Bigg[&\frac{A_{nn}(k)\Big(\eta_{nn_pn_q}(\mathbf{k},\mathbf{p})A_{n_pn_p}(p) + \eta_{nn_qn_p}(\mathbf{k},-\mathbf{k}-\mathbf{p})A_{n_qn_q}(|\mathbf{k}+\mathbf{p}|)\Big)}{\Gamma_{n_pn_q}(\mathbf{k},\mathbf{p})} \\ &+ \frac{2\lambda_{nn_pn_q}(\mathbf{k},\mathbf{p})A_{n_pn_p}(p)A_{n_qn_q}(|\mathbf{k}+\mathbf{p}|)}{\Gamma_{n_pn_q}(\mathbf{k},\mathbf{p})}\Bigg] |\,\mathrm{d}\mathbf{p}|. \end{aligned} \tag{C.2}$$

Equipartition may occur if, in addition to neglecting dissipation, the ranges of n and k are truncated. Thus, attention is restricted to $A_{nn}(k)$ for which $k \leq k_{max}$, $0 < |n| \leq n_{max}$ and (C.2) only applied to these values. Furthermore, the sum in (C.2) is restricted to $0 < |n_p| \leq n_{max}$, $0 < |n_q| \leq n_{max}$ and the integral to that part of $C_{nn_pn_q}(\mathbf{k})$ for which $p \leq k_{max}$ and $|\mathbf{k}+\mathbf{p}| \leq k_{max}$. Equipartition means that $A_{nn}(k)$ has the same value for all $k \leq k_{max}$ and $n \leq n_{max}$. In that case, the right-hand side is zero, according to (B.11). Thus, the dissipationless wave-turbulence equations, truncated in the above manner, respect equipartition.

D. The resonance curve in the limit $k \to \infty$

Defining

$$\hat{\boldsymbol{p}} = \frac{\mathbf{p}}{k}, \quad a = \frac{n_p}{n}, \quad b = \frac{n_q}{n}, \tag{D.1}$$

(3.28) gives

$$\frac{a}{\left(\hat{p}_1^2 + \hat{p}_2^2\right)^{1/2}} + \frac{b}{\left((\hat{p}_1 + 1)^2 + \hat{p}_2^2\right)^{1/2}} + 1 = 0. \tag{D.2}$$

The requirement $n_p < 0$ or $n_q < 0$, necessary for the existence of the resonance curve, is equivalent to $a < 0$ or $b < 0$ since $n > 0$. If $a > 0$, b must be negative and we rewrite (D.2) as

$$\frac{b}{\left(\hat{q}_1^2 + \hat{q}_2^2\right)^{1/2}} + \frac{a}{\left((\hat{q}_1 + 1)^2 + \hat{q}_2^2\right)^{1/2}} + 1 = 0, \tag{D.3}$$

where $\hat{q}_1 = -\hat{p}_1 - 1$ and $\hat{q}_2 = -\hat{p}_2$. Swapping a with b and $\hat{\boldsymbol{q}}$ with $\hat{\boldsymbol{p}}$ we obtain equation (D.2) with $a < 0$. Thus, we restrict attention to $a < 0$.

The condition (3.26) implies

$$b = s_1 a + s_2, \tag{D.4}$$

where s_1 and s_2 take one of the values ± 1. According to their original definitions, a and b are nonzero, rational numbers. The range of a and b is subsequently extended to all real values, constrained by (D.4), $a < 0$ and $b \neq 0$. In so doing, it should be borne in mind that, when $s_1 = s_2$, the limit $a \to -1$ implies $b \to 0$ and (D.2) yields the limiting resonance curve

$$\hat{p} = 1. \tag{D.5}$$

Although the singularity at $\hat{\boldsymbol{p}} = (-1, 0)$ is absent when $b = 0$, it approaches the resonance curve as $b \to 0$. This makes $s_1 = s_2$, $a \to -1$ a singular limit.

As $a \to 0$, there are two cases: $s_2 = 1$ and $s_2 = -1$. In the case $s_2 = 1$ it follows from (D.4) that $b \to 1$. Hence, the only negative term in (D.2) is the first one, which must not tend to zero, otherwise (D.2) cannot be satisfied. This requires that $\hat{p} \to 0$. Thus, the sum of other two terms tends to 2 and (D.2) gives

$$\hat{p} = -\frac{1}{2}a, \tag{D.6}$$

a small circle centered on $\hat{\boldsymbol{p}} = 0$.

On the other hand, if $s_2 = -1$, $b \to -1$ and (D.2) approaches

$$\left((\hat{p}_1 + 1)^2 + \hat{p}_2^2\right)^{1/2} = 1, \tag{D.7}$$

a circle centred on $\hat{\boldsymbol{p}} = (-1, 0)$.

In either of the above cases, the curve arising from (D.2) has a single loop as $a \to 0$.

Let us examine the possibility that the number of loops changes as a varies in $a < 0$. Leaving aside the singular case $s_1 = s_2$, $a = -1$, for this to happen, both the left-hand side of (D.2) and its derivatives with respect to $\hat{p}_1$ and $\hat{p}_2$ must be simultaneously zero, i.e. (D.2),

$$\frac{a\hat{p}_1}{\left(\hat{p}_1^2 + \hat{p}_2^2\right)^{3/2}} + \frac{b(\hat{p}_1 + 1)}{\left((\hat{p}_1 + 1)^2 + \hat{p}_2^2\right)^{3/2}} = 0, \tag{D.8}$$

and

$$\hat{p}_2\left(\frac{a}{\left(\hat{p}_1^2 + \hat{p}_2^2\right)^{3/2}} + \frac{b}{\left((\hat{p}_1 + 1)^2 + \hat{p}_2^2\right)^{3/2}}\right) = 0 \tag{D.9}$$

all hold. (D.9) implies either $\hat{p}_2 = 0$ or

$$\frac{a}{\left(\hat{p}_1^2 + \hat{p}_2^2\right)^{3/2}} + \frac{b}{\left((\hat{p}_1 + 1)^2 + \hat{p}_2^2\right)^{3/2}} = 0. \tag{D.10}$$

If (D.10) is satisfied, (D.8) gives

$$\frac{b}{\left((\hat{p}_1 + 1)^2 + \hat{p}_2^2\right)^{3/2}} = 0, \tag{D.11}$$

hence

$$\frac{a}{\left(\hat{p}_1^2 + \hat{p}_2^2\right)^{3/2}} = 0 \tag{D.12}$$

according to (D.10). (D.11) and (D.12) imply $a = b = 0$, but this is inconsistent with (D.4). We conclude that $\hat{p}_2 = 0$ and so (D.2) and (D.8) become

$$\frac{a}{\left|\hat{p}_1\right|} + \frac{b}{\left|\hat{p}_1 + 1\right|} + 1 = 0, \tag{D.13}$$

$$\frac{a\hat{p}_1}{\left|\hat{p}_1\right|^3} + \frac{b(\hat{p}_1 + 1)}{\left|\hat{p}_1 + 1\right|^3} = 0. \tag{D.14}$$

The solution of (D.14) is

$$\hat{p}_1 = \frac{1}{\operatorname{sgn}(b)|b/a|^{1/2} - 1}, \tag{D.15}$$

which is used in (D.13) to obtain

$$\left(\mathrm{sgn}(b)|b|^{1/2} - |a|^{1/2}\right)\left|\mathrm{sgn}(b)|b|^{1/2} - |a|^{1/2}\right| + 1 = 0. \tag{D.16}$$

b can be determined using (D.4), hence the left-hand side of (D.16) is a function of $a < 0$ which

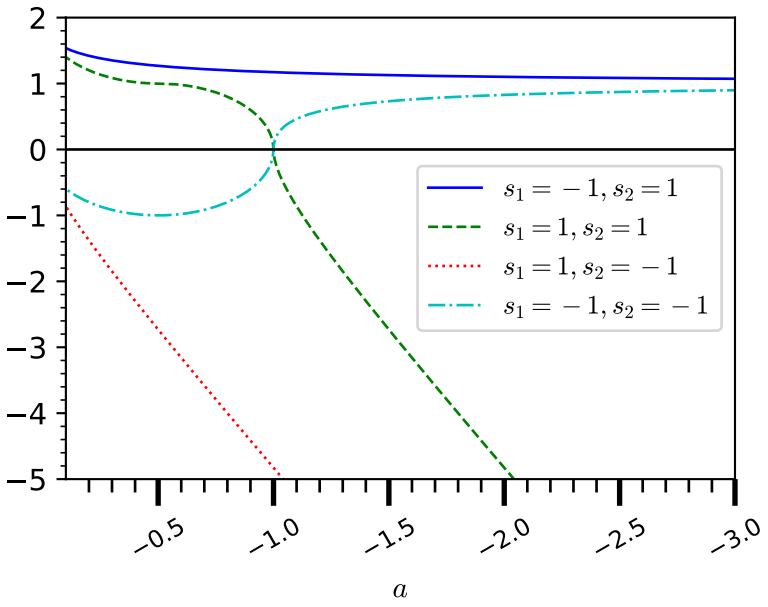

Figure D.1.: Plots of the left-hand side of (D.16) for all combinations of s_1 and s_2.

must be zero for a change in the number of loops. Figure D.1 shows plots of this function for the four possible values of s_1, s_2. When $s_1 \neq s_2$, there are no zeroes and hence no change in the number of loops. There being a single loop in the limit $a \to 0$, this remains the case for all $a < 0$. If $s_1 = s_2$, there is a zero at $a = -1$, the singular case excluded earlier. Recalling the previous result, (D.5), the limiting curve consists of a single loop when $a \to -1$. On each side of $a = -1$, the left-hand side of (D.16) has no zeroes and the number of loops remains 1. We conclude that, in the limit $k \to \infty$, the resonance curve exists and consists of a single loop (provided, of course, that $n_p < 0$ or $n_q < 0$).

E. Critical-point determination

Since $\mathbf{k} = (k, 0) \neq 0$, (3.30) implies $p_2 = 0$ and

$$\frac{n_p \pi p_1}{\left(p_1^2 + n_p^2 \pi^2\right)^{3/2}} + \frac{n_q \pi (k + p_1)}{\left((k + p_1)^2 + n_q^2 \pi^2\right)^{3/2}} = 0, \tag{E.1}$$

while (3.29) gives

$$\frac{n\pi}{\left(k^2 + n^2 \pi^2\right)^{1/2}} + \frac{n_p \pi}{\left(p_1^2 + n_p^2 \pi^2\right)^{1/2}} + \frac{n_q \pi}{\left((k + p_1)^2 + n_q^2 \pi^2\right)^{1/2}} = 0. \tag{E.2}$$

We look for solutions of (E.1) and (E.2) in what follows. Given symmetry under the transformation $n_p \leftrightarrow n_q$, $\mathbf{p} \leftrightarrow -\mathbf{k} - \mathbf{p}$, we restrict attention to $|n_p| \geq |n_q|$.

Writing

$$X = \frac{(k + p_1)^2}{n_q^2 \pi^2} + 1, \tag{E.3}$$

(E.1) implies

$$4\alpha X^3 - 27X + 27 = 0, \tag{E.4}$$

where

$$\alpha = \frac{27\pi^4 n_p^2 n_q^2 \xi^2}{4\left(\xi^2 + n_p^2 \pi^2\right)^3} \tag{E.5}$$

and $\xi = |p_1|$. As a function of ξ, α has a maximum of n_q^2/n_p^2 at $\xi = |n_p|\pi/\sqrt{2}$, hence $\alpha \leq 1$ since $|n_p| \geq |n_q|$. Because $k > 0$, (E.1) implies $p_1 \neq 0$, hence $\xi > 0$. Thus, we can restrict attention to $\xi > 0$, in which case $0 < \alpha \leq 1$. (E.4) has two roots, $X_- < X_+$, in $X > 1$ for $0 < \alpha < 1$, which merge as the double root $X_- = X_+ = 3/2$ when $\alpha = 1$. As $\alpha \to 0$, $X_- \to 1$ and $X_+ \to +\infty$. To avoid problems near $\alpha = 0$, it is better to work with

$$27Y^3 - 27Y^2 + 4\alpha = 0, \tag{E.6}$$

where $Y = X^{-1}$. The two roots in $Y > 0$ are

$$Y_- = 1 - \frac{4}{3}\sin^2\frac{1}{3}\phi, \tag{E.7}$$

$$Y_+ = \frac{2}{3}\sin\frac{1}{3}\phi\left(\sin\frac{1}{3}\phi + \sqrt{3}\cos\frac{1}{3}\phi\right), \tag{E.8}$$

where $0 < \phi \leq \pi/2$ is the solution of

$$\sin\phi = \alpha^{1/2}. \tag{E.9}$$

Satisfaction of (E.1) implies one of the two values

$$k = g_\pm(\xi)\,\mathrm{sgn}(p_1), \tag{E.10}$$

where

$$g_\pm(\xi) = -\xi - n_q\pi\,\mathrm{sgn}\big(n_p\big)(X_\pm - 1)^{1/2}. \tag{E.11}$$

$k > 0$ requires $g_\pm(\xi) \neq 0$ and that the sign of p_1 be chosen to be the same as $g_\pm(\xi)$. (E.2) and (E.10) give

$$h_\pm(\xi) \stackrel{\text{def}}{=} \frac{n\pi}{\left(g_\pm(\xi)^2 + n^2\pi^2\right)^{1/2}} + \frac{n_p\pi}{\left(\xi^2 + n_p^2\pi^2\right)^{1/2}} + \frac{n_q\pi}{\left(\left(g_\pm(\xi)+\xi\right)^2 + n_q^2\pi^2\right)^{1/2}} = 0. \tag{E.12}$$

Note that if $g_\pm(\xi) = 0$, (E.12) becomes

$$\frac{n_p\pi}{\left(\xi^2 + n_p^2\pi^2\right)^{1/2}} + \frac{n_q\pi}{\left(\xi^2 + n_q^2\pi^2\right)^{1/2}} + 1 = 0. \tag{E.13}$$

This is the same as (3.27) and, as show, earlier, requires that $n_p, n_q < 0$. (E.11) then implies the contradiction $g_\pm(\xi) < 0$. Thus, (E.12) is incompatible with $g_\pm(\xi) = 0$ and any solutions of (E.12) lead to critical points with

$$k = \left|g_\pm(\xi)\right|, \quad p_1 = \xi\,\mathrm{sgn}(g_\pm(\xi)). \tag{E.14}$$

Note that, as $\xi \to 0$, $h_+(\xi) \to \mathrm{sgn}(n_p)$ and $h_-(\xi) \to 1 + \mathrm{sgn}(n_p) + \mathrm{sgn}(n_q)$. These limiting values can be used to extend the range of $h_\pm(\xi)$ down to $\xi = 0$.

To find critical points, the two functions $h_\pm(\xi)$ are numerically evaluated at closely and equally spaced points covering the range $0 \leq \xi \leq \xi_{max}$. A change in sign indicates a critical point, which is then refined by interval halving. This procedure is carried out for all $0 < n \leq n_{max}$ and $n_p, n_q \neq 0$ such that $\left|n_q\right| \leq \left|n_p\right| \leq n_{max}$ and one of the four conditions $n \pm n_p \pm n_q = 0$ is satisfied. The case $\left|n_p\right| \leq \left|n_q\right| \leq n_{max}$ can be treated using the symmetry $n_p \leftrightarrow n_q$, $\mathbf{p} \leftrightarrow -\mathbf{k} - \mathbf{p}$.

The above procedure was carried out with $n_{max} = 20$, $\xi_{max} = 200$ and 10000 points covering the range $0 \leq \xi \leq \xi_{max}$. It was found that a single critical point existed provided n_p and n_q are of opposite signs. Although we are unable to provide a proof that this is true, we assume it to hold.

F. Jump of the spectrum at a critical point

Considering a critical point $\mathbf{k}_c = (k_c, 0)$, $\mathbf{p}_c = (p_{c1}, 0)$ we examine the limit of the integral on the right-hand side of the (3.20) as $k \searrow k_c$. The coefficients $\eta_{nn_pn_q}(\mathbf{k}, \mathbf{p})$ and $\lambda_{nn_pn_q}(\mathbf{k}, \mathbf{p})$ are smooth functions of $\mathbf{k}$ and $\mathbf{p}$ and can thus be approximated by their values at $\mathbf{k}_c$, $\mathbf{p}_c$. It seems unlikely that jumps in $A_{n_pn_p}(p)$ and $A_{n_qn_q}(|\mathbf{k} + \mathbf{p}|)$ are situated precisely at p_c and $\left|\mathbf{k}_c + \mathbf{p}_c\right|$, so these quantities are also approximated by their values at $\mathbf{k}_c$, $\mathbf{p}_c$. Thus, using (3.39) the integral has the limiting form

$$\pi I A_{n_pn_p}(p_c)\Big(\eta_{nn_pn_q}(\mathbf{k}_c, \mathbf{p}_c)A_{nn}(k) + \lambda_{nn_pn_q}(\mathbf{k}_c, \mathbf{p}_c)A_{n_qn_q}\Big(\left|\mathbf{k}_c + \mathbf{p}_c\right|\Big)\Big), \tag{F.1}$$

where

$$I = \oint_C \frac{|\,\mathrm{d}\mathbf{p}|}{\left(\mu_1^2(p_1 - p_{c1})^2 + \mu_2^2 p_2^2\right)^{1/2}}, \tag{F.2}$$

where C is the ellipse defined by (3.38). The position on the ellipse can be written as

$$p_1 - p_{c1} = \left(\frac{-2\kappa(k - k_c)}{\mu_1}\right)^{1/2} \cos\theta, \tag{F.3}$$

$$p_2 = \left(\frac{-2\kappa(k - k_c)}{\mu_2}\right)^{1/2} \sin\theta, \tag{F.4}$$

from which,

$$|\,\mathrm{d}\mathbf{p}| = \left(\mathrm{d}p_1^2 + \mathrm{d}p_2^2\right)^{1/2} = (-2\kappa(k - k_c))^{1/2}\left(\frac{\sin^2\theta}{\mu_1} + \frac{\cos^2\theta}{\mu_2}\right)^{1/2} \mathrm{d}\theta \tag{F.5}$$

and

$$\begin{aligned}\left(\mu_1^2(p_1 - p_{c1})^2 + \mu_2^2 p_2^2\right)^{1/2} &= (-2\kappa(k - k_c))^{1/2}\left(\mu_1\cos^2\theta + \mu_2\sin^2\theta\right)^{1/2} \\ &= (-2\kappa(k - k_c))^{1/2}(\mu_1\mu_2)^{1/2}\left(\frac{\cos^2\theta}{\mu_2} + \frac{\sin^2\theta}{\mu_1}\right)^{1/2}.\end{aligned} \tag{F.6}$$

Applying (F.5) and (F.6) to (F.2) gives

$$I = \int_0^{2\pi} (\mu_1\mu_2)^{-1/2} \, \mathrm{d}\theta = 2\pi(\mu_1\mu_2)^{-1/2}, \tag{F.7}$$

which leads to (3.40).

G. Determination of $\lambda^{(p)}(k)$ and $X_n^{(p)}(k)$ for $k \neq 0$

The eigenvalue problem is

$$\sum_{m=-N}^{N} A_{nm}\, X_m = \lambda X_n. \tag{G.1}$$

Writing $A_{nm} = A^r_{nm} + \mathrm{i}A^i_{nm}$, $X_n = X^r_n + \mathrm{i}X^i_n$, (G.1) is equivalent to

$$\sum_{m=-N}^{N} A^r_{nm}\, X^r_m - \sum_{m=-N}^{N} A^i_{nm}\, X^i_m = \lambda X^r_n, \tag{G.2}$$

$$\sum_{m=-N}^{N} A^i_{nm}\, X^r_m + \sum_{m=-N}^{N} A^r_{nm}\, X^i_m = \lambda X^i_n, \tag{G.3}$$

where we have used the fact that λ is real since A_{nm} is Hermitian. Furthermore, the property $A_{-n,-m} = A^*_{nm}$ implies

$$A^r_{-n,-m} = A^r_{nm}, \qquad A^i_{-n,-m} = -A^i_{nm}. \tag{G.4}$$

Looking for solutions of (G.2) and (G.3) such that $X^r_{-n} = X_n$ and $X^i_{-n} = -X^i_n$, the left-hand sides of these equations become

$$\sum_{m=-N}^{N} A^r_{nm}\, X^r_m - \sum_{m=-N}^{N} A^i_{nm}\, X^i_m$$

$$= \frac{1}{2}\left(A^r_{n,0} + A^r_{-n,0}\right)X^r_0 + \sum_{m=1}^{N}\left(A^r_{n,m} + A^r_{-n,m}\right)X^r_m - \sum_{m=1}^{N}\left(A^i_{n,m} + A^i_{-n,m}\right)X^i_m, \tag{G.5}$$

$$\sum_{m=-N}^{N} A^i_{nm}\, X^r_m + \sum_{m=-N}^{N} A^r_{nm}\, X^i_m$$

$$= \frac{1}{2}\left(A^i_{n,0} - A^i_{-n,0}\right)X^r_0 + \sum_{m=1}^{N}\left(A^i_{n,m} - A^i_{-n,m}\right)X^r_m - \sum_{m=1}^{N}\left(A^r_{n,m} - A^r_{-n,m}\right)X^i_m, \tag{G.6}$$

where we have used (G.4) and $X_0^i = 0$ (which follows from $X_{-n}^i = -X_n^i$). Like X_n^r and X_n^i, the right-hand sides of (G.5) and (G.6) are respectively symmetric and antisymmetric under the transformation $n \mapsto -n$. Thus (G.2) and (G.3) are satisfied if

$$\frac{1}{2}\left(A_{n,0}^r + A_{-n,0}^r\right)X_0^r + \sum_{m=1}^{N}\left(A_{n,m}^r + A_{-n,m}^r\right)X_m^r - \sum_{m=1}^{N}\left(A_{n,m}^i + A_{-n,m}^i\right)X_m^i = \lambda X_n^r \qquad 0 \le n \le N, \tag{G.7}$$

$$\frac{1}{2}\left(A_{n,0}^i - A_{-n,0}^i\right)X_0^r + \sum_{m=1}^{N}\left(A_{n,m}^i - A_{-n,m}^i\right)X_m^r - \sum_{m=1}^{N}\left(A_{n,m}^r - A_{-n,m}^r\right)X_m^i = \lambda X_n^i \qquad 1 \le n \le N. \tag{G.8}$$

Employing (G.4), $A_{mn}^r = A_{nm}^r$ and $A_{mn}^i = -A_{nm}^i$, (G.7) and (G.8) give

$$A_{00}\,X_0^r + 2\sum_{m=1}^{N} A_{0,m}^r X_m^r - 2\sum_{m=1}^{N} A_{0,m}^i r X_m^i = \lambda X_0^r, \tag{G.9}$$

$$A_{0,n}^r\,X_0^r + \sum_{m=1}^{N}\left(A_{n,m}^r + A_{-n,m}^r\right)X_m^r - \sum_{m=1}^{N}\left(A_{n,m}^i + A_{-n,m}^i\right)X_m^i = \lambda X_n^r \qquad 1 \le n \le N, \tag{G.10}$$

$$-A_{0,n}^i\,X_0^r - \sum_{m=1}^{N}\left(A_{m,n}^i + A_{-m,n}^i\right)X_m^r + \sum_{m=1}^{N}\left(A_{n,m}^r - A_{-n,m}^r\right)X_m^i = \lambda X_n^i \qquad 1 \le n \le N. \tag{G.11}$$

Equation (G.9), (G.10), (G.11) can be rewritten in the matrix form

$$\begin{bmatrix} A_{00} & \chi_r^T & \chi_i^T \\ \chi_r & C & D \\ \chi_i & D^T & E \end{bmatrix} Y = \lambda Y, \tag{G.12}$$

where

$$Y = \begin{bmatrix} 2^{-1/2}\,X_0^r \\ X_1^r \\ \vdots \\ X_N^r \\ X_1^i \\ \vdots \\ X_N^i \end{bmatrix}, \qquad \chi_r = \begin{bmatrix} \chi_1^r \\ \vdots \\ \chi_N^r \end{bmatrix}, \qquad \chi_i = \begin{bmatrix} \chi_1^i \\ \vdots \\ \chi_N^i \end{bmatrix}, \tag{G.13}$$

$$\chi_n^r = 2^{1/2}\,A_{0,n}^r, \qquad \chi_n^i = -2^{1/2}\,A_{0,n}^i, \tag{G.14}$$

$$C_{nm} = A^r_{n,m} + A^r_{-n,m}, \qquad D_{nm} = -A^i_{n,m} - A^i_{-n,m}, \qquad E_{nm} = A^r_{n,m} - A^r_{-n,m} \tag{G.15}$$

and the indices n and m run over the values $1 \leq n, m \leq N$. Using symmetry of A^r_{nm} and the first of equations (G.4)

$$A^r_{-n,m} = A^r_{m,-n} = A^r_{-m,n} \tag{G.16}$$

implies symmetry of C_{nm} and E_{nm}. It follows that the matrix in (G.13) is symmetric. There are thus a complete set of real eigenvectors, $Y^{(p)}$, having real eigenvalues, $\lambda^{(p)}$, and which are orthonormal in the sense that

$$\sum_n Y_n^{(p)} Y_n^{(q)} = \frac{1}{2}\,\delta_{pq}. \tag{G.17}$$

Each such eigenvector yields X^r_n for $n \geq 0$ and X^i_n for $n \geq 1$. Completing the X^r_n and X^i_n using $X^i_0 = 0$ and $X^r_{-n} = X^r_n$, $X^i_{-n} = -X^i_n$ for $n \geq 1$, $X_n = X^r_n + \mathrm{i}X^i_n (-N \leq n \leq N)$ provides a solution of the original complex eigenvalue problem, (G.1). The complex scalar product between any two of these solutions is

$$\sum_{n=-N}^{N} X_n^{(p)*}(k) X_n^{(q)}(k) = \sum_{n=-N}^{N} \left(X_n^{r(p)} X_n^{r(q)} + X_n^{i(p)} X_n^{i(q)} \right) + \mathrm{i} \sum_{n=-N}^{N} \left(X_n^{r(p)} X_n^{i(q)} - X_n^{i(p)} X_n^{r(q)} \right). \tag{G.18}$$

The second sum on the right-hand side is zero by symmetry of X^r_n and antisymmetry of X^i_n with respect to $n \mapsto -n$. The first sum can be written

$$\begin{aligned} \sum_{n=-N}^{N} \left(X_n^{r(p)} X_n^{r(q)} + X_n^{i(p)} X_n^{i(q)} \right) &= X_0^{r(p)} X_0^{r(q)} + 2 \sum_{n=1}^{N} \left(X_n^{r(p)} X_n^{r(q)} + X_n^{i(p)} X_n^{i(q)} \right) \\ &= 2 \sum_n Y_n^{(p)} Y_n^{(q)} \\ &= \delta_{pq}, \end{aligned} \tag{G.19}$$

where we have employed (G.17), symmetry of X^r_n and antisymmetry of X^i_n. Thus, the complex eigenvectors satisfy the orthonormality condition (G.13). The dimension of the problem (G.12) being $2N + 1$, there are the same number of complex eigenvectors, which are linearly independent by orthonormality. Thus, the above procedure generates a complete set. The complex eigenvectors satisfy $X^{(p)}_{-n}(k) = X^{(p)*}_n(k)$ by construction.

Finally, we derive (6.14). Using (6.13) and (G.1),

$$\sum_{m=-N}^{N} \left(A_{nm} - \sum_p \lambda^{(p)}\, X_n^{(p)}\, X_m^{(p)*} \right) X_m^{(q)} = \lambda^{(q)}\, X_n^{(q)} - \sum_p \lambda^{(p)}\, X_n^{(p)}\, \delta_{pq} = 0 \tag{G.20}$$

for any eigenvector $X^{(q)}_m$. Since the eigenvectors form a complete set, the matrix in brackets on the left of (G.20) must be zero, hence (6.14).

H. Details of calculations for the initialization

Using equation (6.6)

$$\overline{W_i^{(n)*}(x_3;0)W_j^{(m)}(x_3';0)} = \frac{1}{4M}\sum_{r,r'=0}^{4M-1} V_i^{(n)*}(x_3;\phi_r)V_j^{(m)}(x_3';\phi_{r'})\overline{\exp\{\mathrm{i}(\theta_r-\theta_{r'})\}}. \tag{H.1}$$

Given the definition of the θ_r, the average on the right-hand side is zero unless $r' = r$, thus

$$\overline{W_i^{(n)*}(x_3;0)W_j^{(m)}(x_3';0)} = \frac{1}{4M}\sum_{r=0}^{4M-1} V_i^{(n)*}(x_3;\phi_r)V_j^{(m)}(x_3';\phi_r). \tag{H.2}$$

Using (6.3)-(6.5), the right-hand side of (H.2) can be written in terms of arithmetic averages over $0 \le r \le 4M-1$ of $\sin^2\phi_r$, $\cos^2\phi_r$ and $\sin\phi_r\cos\phi_r$. Given $\phi_r = \pi r/2M$, these averages are respectively $1/2$, $1/2$ and 0, hence

$$\overline{W_i^{(n)*}(x_3;0)W_j^{(m)}(x_3';0)} = \frac{1}{2}\begin{bmatrix} 1+s_ns_m & -\mathrm{i}(s_n+s_m) & 0 \\ \mathrm{i}(s_n+s_m) & 1+s_ns_m & 0 \\ 0 & 0 & 0 \end{bmatrix}\cos n\pi x_3 \cos m\pi x_3'. \tag{H.3}$$

Equation (6.9) implies $\aleph_{nm}(0) = \overline{\alpha_n^*(0)\alpha_m(0)}$, from which we deduce, using $\alpha_n^*(0) = \alpha_{-n}(0)$, that $\aleph_{-n,-m}(0) = \aleph_{nm}^*(0)$. Writing $\aleph_{nm}(0) = \aleph_{nm}^r(0) + i\aleph_{nm}^i(0)$, this gives $\aleph_{-n,-m}^r(0) = \aleph_{nm}^r(0)$ and $\aleph_{-n,-m}^i(0) = -\aleph_{nm}^i(0)$. Given the definition of s_n, the right-hand side of (H.3) is zero if n and m are nonzero and of opposite signs. Using these results, the definition of s_n and (H.3), the first

sum in (6.10) gives

$$\sum_{n,m=-N}^{N} \aleph_{nm}(0)\overline{W_i^{(n)*}(x_3;0)W_j^{(m)}(x_3';0)} = \frac{1}{2}\begin{bmatrix} \aleph_{00}^r(0) & 0 & 0 \\ 0 & \aleph_{00}^r(0) & 0 \\ 0 & 0 & 0 \end{bmatrix}$$

$$+\sum_{n=1}^{N}\begin{bmatrix} \aleph_{n0}^r(0) & \aleph_{n0}^i(0) & 0 \\ -\aleph_{n0}^i(0) & \aleph_{n0}^r(0) & 0 \\ 0 & 0 & 0 \end{bmatrix}\cos n\pi x_3 + \sum_{m=1}^{N}\begin{bmatrix} \aleph_{0m}^r(0) & \aleph_{0m}^i(0) & 0 \\ -\aleph_{0m}^i(0) & \aleph_{0m}^r(0) & 0 \\ 0 & 0 & 0 \end{bmatrix}\cos m\pi x_3'$$

$$+2\sum_{n,m=1}^{N}\begin{bmatrix} \aleph_{nm}^r(0) & \aleph_{nm}^i(0) & 0 \\ -\aleph_{nm}^i(0) & \aleph_{nm}^r(0) & 0 \\ 0 & 0 & 0 \end{bmatrix}\cos n\pi x_3 \cos m\pi x_3'. \tag{H.4}$$

(H.4) should give the contribution to (3.4) of [27] from the small square centred on $\mathbf{k} = 0$. We approximate $A_{nm}(k)\exp\{\mathrm{i}k_1r_1 + \mathrm{i}k_2r_2\}$ of [27] by its value at $\mathbf{k} = 0$, namely $A_{nm}(0)$. Using (6.2)-(6.5) to approximate $W_i^{(n)*}(x_3;\mathbf{k})W_j^{(m)}(x_3';\mathbf{k})$ for small $\mathbf{k}$, its average over the square is given by the right-hand side of (H.4). Thus, we obtain

$$\int_{-\pi/L}^{\pi/L}\int_{-\pi/L}^{\pi/L} A_{nm}(k)W_i^{(n)*}(x_3;\mathbf{k})W_j^{(m)}(x_3';\mathbf{k})\exp\{\mathrm{i}k_1r_1 + \mathrm{i}k_2r_2\}\,\mathrm{d}k_1\,\mathrm{d}k_2$$

$$\sim \frac{2\pi^2}{L^2}A_{nm}(0)\begin{bmatrix} 1+s_ns_m & -\mathrm{i}(s_n+s_m) & 0 \\ \mathrm{i}(s_n+s_m) & 1+s_ns_m & 0 \\ 0 & 0 & 0 \end{bmatrix}\cos n\pi x_3 \cos m\pi x_3'. \tag{H.5}$$

Summing over $-N \le n, m \le N$ and using $A_{-n,-m}(0) = A_{nm}^*(0)$ gives the right-hand side of (H.4), but with $4\pi^2A_{nm}(0)/L^2$ in place of $\aleph_{nm}(0)$.

Finally, the requirement that the result should agree with (H.4) yields (6.12). It was noted following (6.12) that, whereas (6.11) constrains $\aleph_{nm}(\mathbf{k})$ for all n, m when $\mathbf{k}$ is nonzero, $\aleph_{nm}(0)$ is unconstrained if n and m are nonzero and of opposite signs. This is essentially because the right-hand side of (H.3) is zero for such n, m. Thus, they contribute neither to the integral in (3.4) of [27], nor to the first sum in (6.10).

I. Comparison of DNS cases

This appendix compares the results of DNS for the three different cases summarised in Table 6.1.

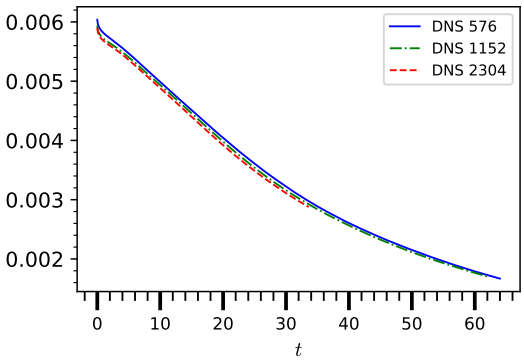

Figure I.1.: The total energy, E, as a function of time, t.

Figure I.1 shows the total (including $n = 0$, but not $k = 0$) energy as a function of time. The results are almost identical for the three cases. Figure I.2 plots D_v as a function of time. Here, the case $N_i = 576$ is rather different from the other two, which are reasonably close. Based on these results, it would appear that $N_i = 1152$ gives acceptable results, though $N_i = 2304$ is of course better. Figure I.3 shows energy spectra at different instants of time. Once again, $N_i = 576$ is somewhat different, while the other two cases seem to have reasonable convergence.

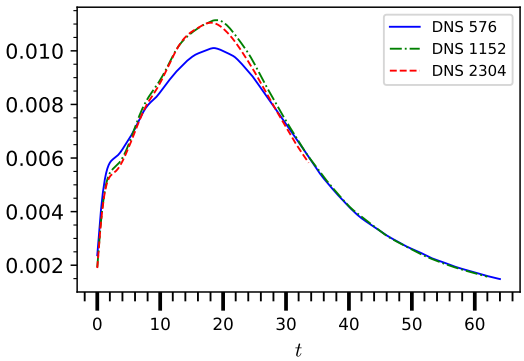

Figure I.2.: Evolution of D_v with time, t.

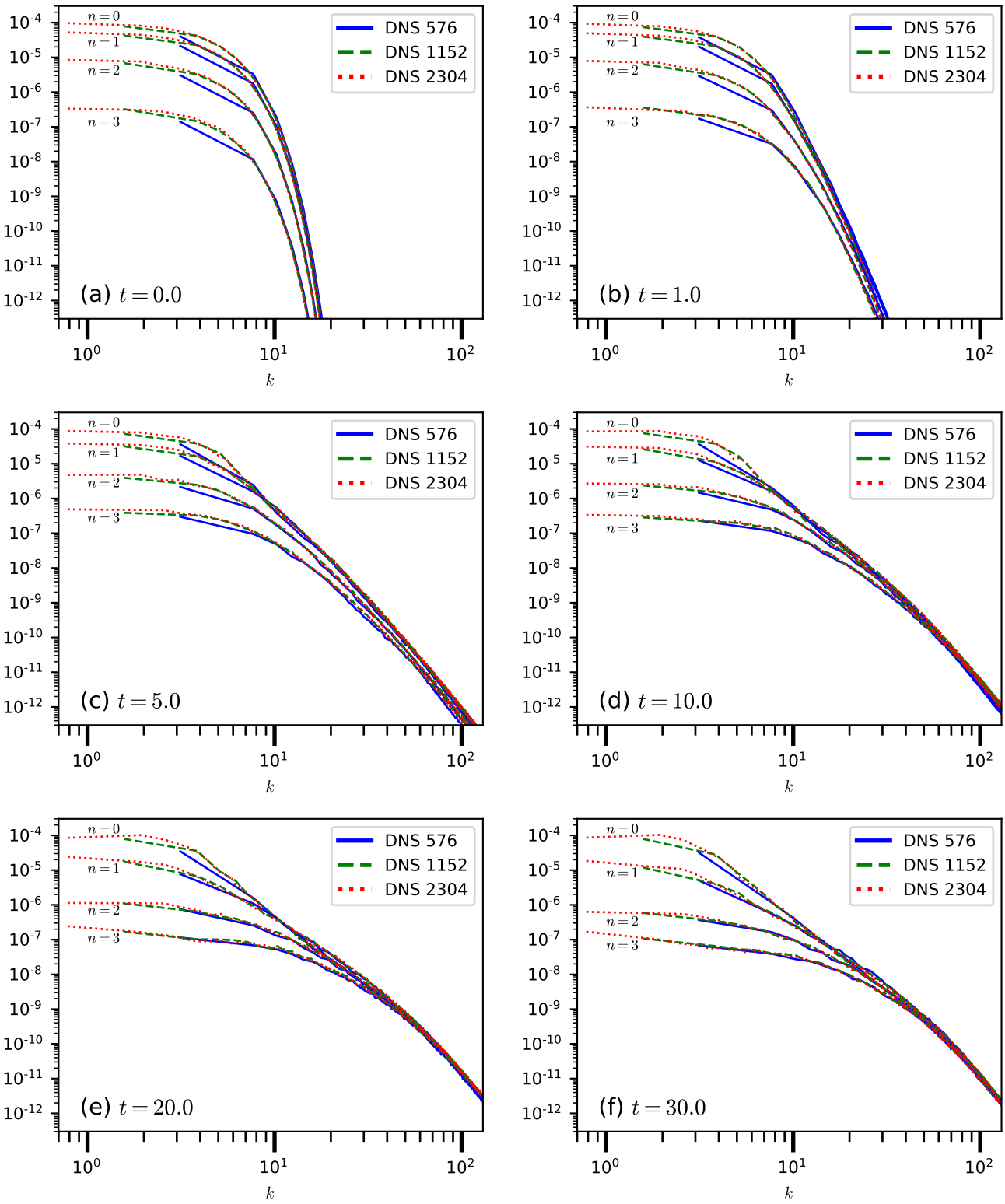

Figure I.3.: $A_{nn}(k)$.

J. 2D DNS

This appendix gives results obtained using 2D DNS for $\Xi = 4$, $\varepsilon = 5.73 \cdot 10^{-2}$ and two values of Ekman number, namely $E = 3.12 \cdot 10^{-5}$ and $E = 0$ (referred to as the inviscid case).

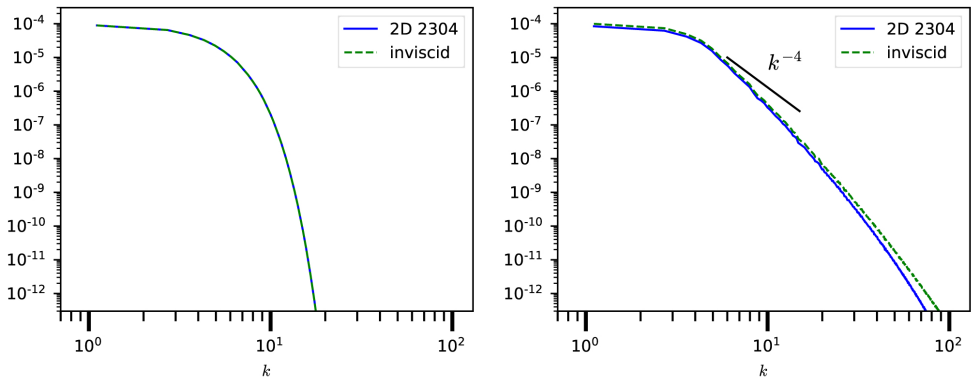

(a) $t = 0$ (b) $t = 10$

(c) $t = 20$ (d) $t = 30$

Figure J.1.: $A_{00}(k)$.

Figures (J.1)-(J.2) show $A_{00}(k)$ at different times. It will be seen that the inviscid and viscous cases are quite similar, at low wavenumbers, though viscous dissipation lowers the spectral level at larger times. This is mainly due to wall damping. It will also be seen that the inviscid spectral slope in the inertial range approaches a value close to -4 at larger times. Because

$A_{00}(k)$ needs to be multiplied by $2\pi k$ to obtain the usual definition of the energy spectrum, this corresponds to the expected k^{-3} behavior.

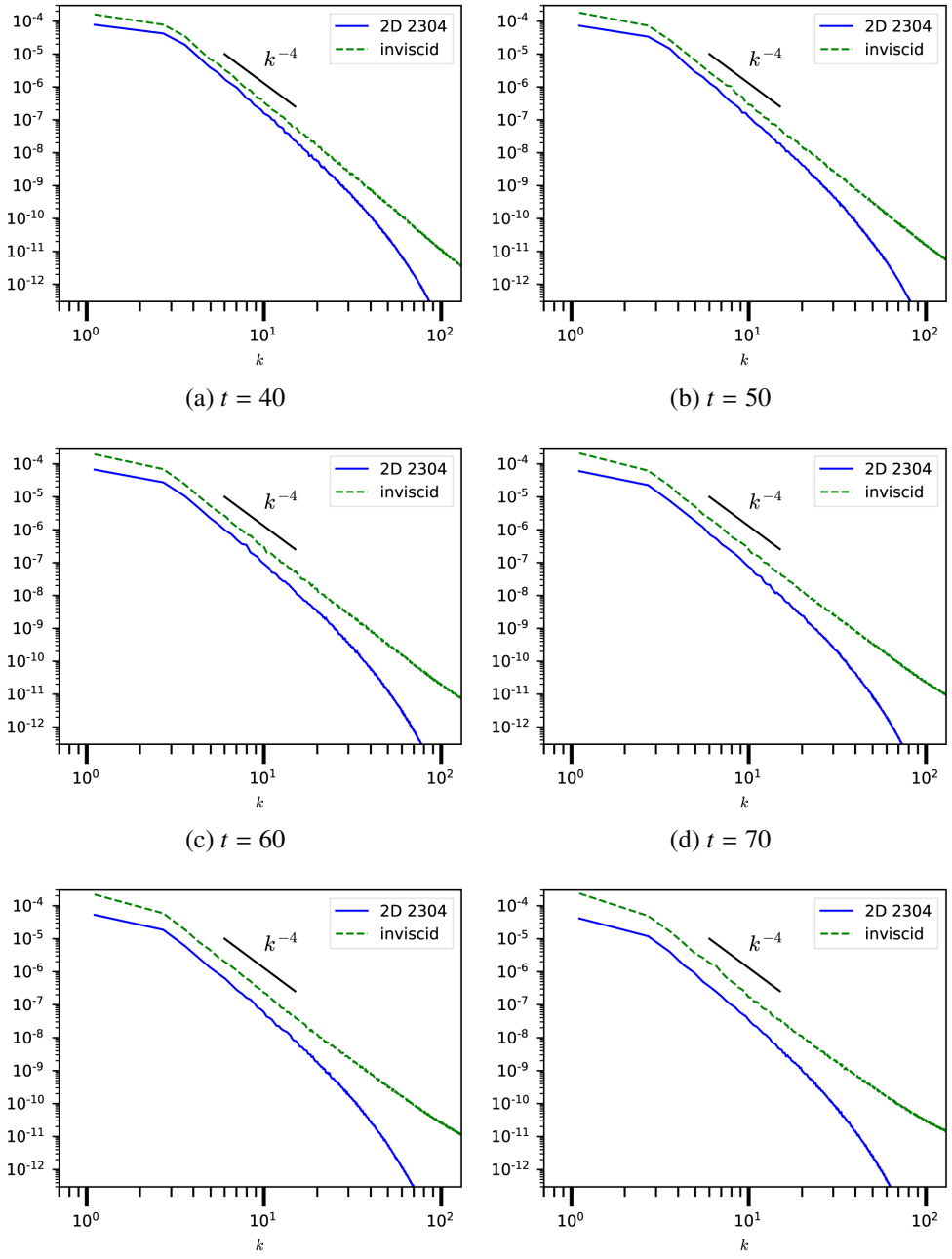

(a) $t = 40$ (b) $t = 50$

(c) $t = 60$ (d) $t = 70$

(e) $t = 80$ (f) $t = 100$

Figure J.2.: $A_{00}(k)$.

Bibliography

[1] G. K. Batchelor. *The Theory of Homogeneous Turbulence*. Cambridge University Press, 1953.

[2] G. K. Batchelor. *An Introduction to Fluid Dynamics*. Cambridge University Press, 1979.

[3] F. Bellet, F. S. Godeferd, J. F. Scott, and C. Cambon. Wave turbulence in rapidly rotating flows. *Journal of Fluid Mechanics*, 562:83, 2006.

[4] D. J. Benney, P. G. Saffman, and G. K. Batchelor. Nonlinear interactions of random waves in a dispersive medium. *Proceedings of the Royal Society of London. Series A. Mathematical and Physical Sciences*, 289(1418):301–320, 1966.

[5] L. Biferale, S. Musacchio, and F. Toschi. Split energy–helicity cascades in three-dimensional homogeneous and isotropic turbulence. *Journal of Fluid Mechanics*, 730: 309–327, 2013.

[6] M. Buffat, L. Le Penven, and A. Cadiou. An efficient spectral method based on an orthogonal decomposition of the velocity for transition analysis in wall bounded flow. *Computers & Fluids*, 42(1):62–72, 2011.

[7] M. Buffat, A. Cadiou, L. Le Penven, and C. Pera. In situ analysis and visualization of massively parallel computations. *The International Journal of High Performance Computing Applications*, 31(1):83–90, 2015.

[8] C. Cambon, N. N. Mansour, and F. S. Godeferd. Energy transfer in rotating turbulence. *Journal of Fluid Mechanics*, 337:303–332, 1997.

[9] S. Galtier. Weak inertial-wave turbulence theory. *Physical Review E*, 68(1):015301, 2003.

[10] C. H. Gibson. Fossil turbulence revisited. *Journal of Marine Systems*, 21(1-4):147–167, 1999.

[11] F. S. Godeferd and F. Moisy. Structure and Dynamics of Rotating Turbulence: A Review of Recent Experimental and Numerical Results. *Applied Mechanics Reviews*, 67(3): 030802, 2015.

[12] J. R. Herring, S. A. Orszag, R. H. Kraichnan, and D. G. Fox. Decay of two-dimensional homogeneous turbulence. *Journal of Fluid Mechanics*, 66(3):417–444, 1974.

[13] G. Holloway and M. C. Hendershott. Stochastic closure for nonlinear Rossby waves. *Journal of Fluid Mechanics*, 82(4):747–765, 1977.

[14] S. S. Hough and G. H. Darwin. IX. On the application of harmonic analysis to the dynamical theory of the tides. — Part I. On laplace's "oscillations of the first species" and the dynamics of ocean currents. *Philosophical Transactions of the Royal Society of London. Series A, Containing Papers of a Mathematical or Physical Character*, 189:201–257, 1897.

[15] L. Jacquin, O. Leuchter, C. Cambon, and J. Mathieu. Homogeneous turbulence in the presence of rotation. *Journal of Fluid Mechanics*, 220:1–52, 1990.

[16] R. H. Kraichnan. Decay of Isotropic Turbulence in the Direct-Interaction Approximation. *The Physics of Fluids*, 7(7):1030–1048, 1964.

[17] R. Kristoffersen and H. I. Andersson. Direct simulations of low-Reynolds-number turbulent flow in a rotating channel. *Journal of Fluid Mechanics*, 256:163–197, 1993.

[18] C. Lamriben, P.-P. Cortet, F. Moisy, and L. R. M. Maas. Excitation of inertial modes in a closed grid turbulence experiment under rotation. *Physics of Fluids*, 23(1):015102, 2011.

[19] J. Lighthill. *Waves in Fluids*. Cambridge University Press, 2001.

[20] A. Mahalov, B. Nicolaenko, and Y. Zhou. Energy Spectra of Strongly Stratified and Rotating Turbulence. *Physical review. E, Statistical physics, plasmas, fluids, and related interdisciplinary topics*, 57, 1998.

[21] J. Montagnier, A. Cadiou, M. Buffat, and L. Le Penven. Towards petascale spectral simulations for transition analysis in wall bounded flow. *International Journal for Numerical Methods in Fluids*, 72:709–723, 2013.

[22] D. W. Moore, P. G. Saffman, and K. Stewartson. The structure of free vertical shear layers in a rotating fluid and the motion produced by a slowly rising body. *Philosophical Transactions of the Royal Society of London. Series A, Mathematical and Physical Sciences*, 264(1156):597–634, 1969.

[23] R. D. Moser, P. Moin, and A. Leonard. A spectral numerical method for the Navier-Stokes equations with applications to Taylor-Couette flow. *Journal of Computational Physics*, 52 (3):524–544, 1983.

[24] A. C. Newell and B. Rumpf. Wave Turbulence. *Annual Review of Fluid Mechanics*, 43 (1):59–78, 2011.

[25] S. A. Orszag. Analytical theories of turbulence. *Journal of Fluid Mechanics*, 41(2): 363–386, 1970.

[26] P. Sagaut and C. Cambon. *Homogeneous Turbulence Dynamics*. Springer International Publishing, 2018.

[27] J. F. Scott. Wave turbulence in a rotating channel. *Journal of Fluid Mechanics*, 741: 316–349, 2014.

[28] P. R. Spalart, R. D. Moser, and M. M. Rogers. Spectral methods for the Navier-Stokes equations with one infinite and two periodic directions. *Journal of Computational Physics*, 96(2):297–324, 1991.

[29] M. Ulitsky, T. Clark, and L. Turner. Testing a random phase approximation for bounded turbulent flow. *Physical Review. E, Statistical Physics, Plasmas, Fluids, and Related Interdisciplinary Topics*, 59(5 Pt B):5511–5522, 1999.

[30] F. Waleffe. The nature of triad interactions in homogeneous turbulence. *Physics of Fluids A: Fluid Dynamics*, 4(2):350–363, 1992.

[31] Y.-T. Yang, W.-D. Su, and J.-Z. Wu. Helical-wave decomposition and applications to channel turbulence with streamwise rotation. *Journal of Fluid Mechanics*, 662:91–122, 2010.

[32] E. Yarom and E. Sharon. Experimental observation of steady inertial wave turbulence in deep rotating flows. *Nature Physics*, 10(7):510–514, 2014.

[33] V. E. Zakharov, V. S. L'vov, and G. Falkovich. *Kolmogorov Spectra of Turbulence I: Wave Turbulence*. Springer Series in Nonlinear Dynamics. Springer-Verlag, 1992.